VILNIUS UNIVERSITY
CENTER FOR PHYSICAL SCIENCES AND TECHNOLOGY

Ilona
ZAMARAITĖ

Ferroelectricity, dielectric and low-frequency noise spectroscopic studies of phosphorus chalcogenide crystals

DOCTORAL DISSERTATION

Technological Sciences,
Material Engineering (T 008)

VILNIUS 2019

This dissertation was written between 2015 and 2019 in Vilnius University.

Academic supervisor:
Dr. Andrius Džiaugys (Vilnius University, Technological Sciences, Material Engineering T 008)

This doctoral dissertation will be defended in a public meeting of the Dissertation Defence Panel:
Chairman – Prof. Habil. Dr. Vytautas Balevičius (Vilnius University, Natural Sciences, Physics N 002).
Members:
Prof. Dr. Valdas Šablinskas (Vilnius University, Technological Sciences, Material Engineering T 008).
Assoc. Prof. Dr. Tomas Šalkus (Vilnius University, Technological Sciences, Material Engineering T 008).
Prof. Habil. Dr. Gintaras Valušis (Center for Physical Sciences and Technologies, Natural Sciences, Physics N 002).
Assoc. Prof. Dr. Bonifacas Vengalis (Center for Physical Sciences and Technologies, Technological Sciences, Material Engineering T 008).

The dissertation shall be defended at a public meeting of the Dissertation Defence Panel on 30th of September, 2019 at 15:00 o`clock in A101 auditorium of National Center for Physical Sciences and Technologies.
Address: Saulėtekio av. 3, LT-10257, Vilnius, Lithuania.

The text of this dissertation can be accessed at the libraries of Vilnius University, Center for Physical Sciences and Technology, as well as on the website of Vilnius University:
www.vu.lt/lt/naujienos/ivykiu-kalendorius

VILNIAUS UNIVERSITETAS
FIZINIŲ MOKSLŲ IR TECHNOLOGIJOS CENTRAS

Ilona
ZAMARAITĖ

Fosforo chalkogenidų kristalų feroelektros, dielektriniai ir žemadažnio triukšmo spektroskopiniai tyrimai

DAKTARO DISERTACIJA

Technologijos mokslai,
Medžiagų inžinerija (T 008)

VILNIUS 2019

Disertacija rengta 2015– 2019 metais Vilniaus universitete.

Mokslinis vadovas – dr. Andrius Džiaugys (Vilniaus universitetas, technologijos mokslai, medžiagų inžinerija – T 008).

Gynimo taryba:
Pirmininkas – **prof. habil. dr. Vytautas Balevičius** (Vilniaus universitetas, gamtos mokslai, fizika – N 002).
Nariai:
prof. dr. Valdas Šablinskas (Vilniaus universitetas, technologijos mokslai, medžiagų inžinerija – T 008);
doc. dr. Tomas Šalkus (Vilniaus universitetas, technologijos mokslai, medžiagų inžinerija – T 008);
prof. habil. dr. Gintaras Valušis (Fizinių ir technologijos mokslų centras, gantos mokslai, fizika – N 002).
doc. dr. Bonifacas Vengalis (Fizinių ir technologijos mokslų centras, technologijos mokslai, medžiagų inžinerija – T 008).

Disertacija ginama viešame Gynimo tarybos posėdyje 2019 m. rugsėjo mėn. 30 d. 15:00 Nacionaliniame fizinių ir technologijos mokslų centre A101 auditorijoje.
Adresas: Saulėtekio al. 3, LT-10257, Vilnius, Lietuva.

Disertaciją galima peržiūrėti Vilniaus universiteto ir Fizinių ir technologijos mokslų centro bibliotekose ir VU interneto svetainėje adresu: https://www.vu.lt/naujienos/ivykiu-kalendorius

Acknowledgements

This thesis would never have been possible without the assistance and support of numerous people:

Most of all I would like to thank dr. Andrius Džiaugys for his guidance during my PhD studies, the fruitful discussions, kind advices and his great support in scientific work.

Sincere gratitude to prof. dr. Jūras Banys for giving me the opportunity to conduct my research in the Laboratory of Microwave Spectroscopy.

It was a great pleasure to collaborate with prof. dr. Yulian Vysochanskii and his co-workers from Uzhgorod University.

Additionally, I would like to thank to prof. dr. Jonas Matukas and assoc. prof. dr. Sandra Pralgauskaitė who introduced me into very interesting field of noise measurements in ferroelectrics.

I would like to thank all former and current members of Laboratory of Microwave Spectroscopy for interesting discussions, collaboratorion and friendly atmosphere. I also wish to express my sincere thanks to all colleagues from Institute of Applied Electrodynamis and Telecommunications for their help and support.

Finally, this dissertation would not have been possible without the support of my family, Alina, Vladas, Lukas and my fiancé Justinas during my whole studies and the following PhD period.

List of Abbrevations

2D – two-dimensional
AFE –antiferroelectric
BEG – Blume-Emery-Griffiths
Br – Bridgman
CP – critical point
CW – Curie-Weiss
FE – ferroelectric
GR – generation-recombination
IC – incommensurate phase
LP –Lifshitz point
OP – order parameter
PE - paraelectric
PT – phase transition
QAO – quantum anharmonic oscillator
QCP – quantum critical point
RTS – random telegraph signal
SPS – $Sn_2P_2S_6$
SPSe – $Sn_2P_2Se_6$
TCP – tricritical point
VT – vapor transport

TABLE OF CONTENTS

1. INTRODUCTION

Ferroelectrics and related materials, such as ferroelectric relaxors, are widely investigated class of materials due to both scientific and engineering point of view. In practical point of view, ferroelectric materials show a number of desirable properties such as a high piezoelectric and pyroelectric responses, polarization switching which can potentially be used for information storage and high dielectric constants. For this reason, they are widely used in devices such as memory elements, ultrasound generators, transducers, capacitors and many others.

The most prominent ferroelectric materials include barium titanate ($BaTiO_3$), lead titanate ($PbTiO_3$) and lead zirconate titanate (PZT), which have been studied extensively over the past decade as the most promising ferroelectric materials. For the past few decades these ferroelectric materials have dominated commercially. In comparison to them ferroelectric phosphorous chalcogenide crystals look rather exotic. Ferroelectric phosphorous chalcogenide family investigated in this doctoral dissertation can be subdivided into two compounds groups. The first is represented by the general formula $M_2P_2X_6$ (where M - transition metal, X – chalcogenides) . Needless to say, these compounds are to be classified as chalcogenohypodiphosphates. The following thiophosphates have so far been synthesized and structurally characterized: $Sn_2P_2S(Se)_6$, $Pb_2P_2S(Se)_6$ [1]. The crystals from $Sn(Pb)_2P_2S(Se)_6$ system have a complicated three-dimensional lattice with no close packing of the chalcogenide atoms [2]. The second crystal group is described by Van der Waals layered structure with the common chemical formula $M^{I}M^{III}P_2X_6$ (where M^{I}, M^{III} – transition metals, X – chalcogenides). Most of these compounds are characterized by compact arrangement of chalcogen atoms, in which two atom layers of phosphorus and a layer of metal atoms placed between them construct the two-dimensional fragments in form of a sandwich [2]. Inside of such layer structure strong ion-covalent bonds are formed, and Van der Waals gaps exist between the layers [3]–[5]. Indeed, layered materials in which M^{I} = Cu or Ag, M^{III}= In, Bi, Sc or Cr have been prepared and characterized [4]–[6][7]. A common peculiarity for both structures exists - the presence of $(P_2X_6)^{4-}$ anions [2].

The interest in ferroelectric phosphorus chalcogenides is not only motivated by the large variety of crystal structures but also by the variety of their physical properties. $Sn_2P_2S_6$ crystals are the most prominent example of ferroelectric ternary phosphorus chalcogenide. Moreover, optical

measurements have proven $Sn_2P_2S_6$ as a semiconductor with relatively narrow bandgap and promising photorefractive, photovoltaic, electrooptic and piezoelectric features [8], [9]. Another feature, which makes them attractive for researches, is an isovalent anion substitution into the crystal lattice producing series of $(Pb_ySn_{1-y})_2P_2(Se_xS_{1-x})_6$ crystal. The impact of dopants on the ferroelectricity of the crystals has a special attention as an effective engineering approach that introduces changes in the position or character of phase transition and physical properties. Prior work on $Sn_2P_2S_6$ has focused mainly on the explanation of ferroectricity nature, photorefraction properties and characterization of the absorption edges in relation to ferroelectricity. The motivation of this study is defined by the interest of ferroelectric properties and possible memory applications of $Sn_2P_2S_6$ crystals. The influence of the crystal lattice defects that appear upon the partial substitution of dopants is also investigated.

Since the isolation of single graphene layers, graphene-analogous two-dimensional (2D) materials have gained broad attention due to their unique physical phenomena that could have potential applications in novel electronic devices [10]. Recently, some of the most emphasized layered materials are hexagonal boron nitride [11] and transition metal dichalcogenides with the well-studied MoS_2 [12]. The quaternary phosphorous chalcogenide crystals are mainly characterized by lamellar structure and ionic bonding within each layer. Given that these are Van der Waals crystals, they can be exfoliated to nanoscale 2D flake [13]. Such a two-dimensional lamellar material with strong in-plane chemical bonds and weak coupling between the layers appears as the most suitable candidate to create a new generation of integrated electronic devices because layered structures provide an opportunity to be easily cleaved into individual atomic-thick layers. Copper indium thiophosphate ($CuInP_2S_6$) is the best known representative of these layered compounds. Up till now, the structural and physical properties of $CuInP_2S_6$ bulk and nanoscale crystals have been extensively studied and reviewed [3], [14], [15]. In this dissertation the low-frequency noise characteristics of the well-studied lamellar ferrielectric-semiconductor $CuInP_2S_6$ crystal were explored. The investigations of noise behavior of $CuInP_2S_6$ are motivated by the interest in some additional information on dynamics of physical processes that take place near the phase transition.

1.1.Aim and main tasks of the work

The **main aim** of this doctoral dissertation is to investigate the dielectric, ferroelectric, pyroelectric and noise properties related to the phase transitions of ternary and quaternary phosphorus chalcogenide crystals.

The following **tasks** were formulated in order to achieve the aim of the work:

1. To investigate the ferroelectric and antiferroelectric instabilities observed in $Sn_2P_2S_6$ crystals and to compare dielectric and ferroelectrics measurements results of the same crystals;
2. To investigate dielectric, ferroelectric and pyroelectric anomalies of $(Pb_ySn_{1-y})_2P_2S_6$ solid solutions, studying the influence of Pb atoms on the phase diagram;
3. To investigate the influence of small amounts of Ge dopants on the dielectric properties of the $(Pb_ySn_{1-y})_2P_2S_6$ crystals.
4. To establish the relation between the macroscopic and fluctuation aspects of ferrielectric $CuInP_2S_6$ crystal and to present noise spectroscopy as a powerfull tool to characterize processess occuring in the vicinity of polar phase transition.

1.2.Scientific novelty

1. Double antiferroelectric-like hysteresis loops are observed for the first time in a bulk proper uniaxial $Sn_2P_2S_6$ ferroelectric crystal grown by Bridgman-method. Double polarization hysteresis loops are an exceptional phenomenon in ferroelectrics. It was clearly explained the realization of “ordinary” and “double” hysteresis loops in $Sn_2P_2S_6$ ferroelectrics.
2. The complete analysis of the dielectric permittivity, pyroelectric coefficient and polarization dependencies in a wide temperature range has been undertaken for $(Pb_ySn_{1-y})_2P_2S_6$ mixed crystals and related with the features occurring on their phase diagram.
3. Dielectric permitivitty has been measured for the first time for $Pb_2P_2S_6$, $(Pb_{0.98}Ge_{0.02})_2P_2S_6$, $(Pb_{0.7}Sn_{0.3})_2P_2S_6$+5%Ge and $(Pb_{0.7}Sn_{0.3})_2P_2Se_6$+5%Ge compounds in the wide temperature range (20-300K).
4. Detailed modeling of the noise characteristics of the ferrielectric crystal near the phase transition was performed for the first time. The obtained results indicate noise spectroscopy as being a reliable, sensitive, and

non-destructive tool complementary to the other measurement techniques for the characterization of ferroelectric materials.

1.3. Statements presented for defence

1. Peculiar polarization switching in bulk proper ferroelectric $Sn_2P_2S_6$ is determined by the local three-well potential for spontaneous polarization fluctuations.
2. Dielectric, pyroelectric and ferroelectric characterization of $(Pb_ySn_{1-y})_2P_2S_6$ mixed crystals give evidences of coexistence of phases in the *T-y* phase diagram at $y>0.2$.
3. Ge-doping have a relevant consequences on quantum paraelectric behavior of $Pb_2P_2S_6$.
4. A sharp changes of low-frequency noise characteristics indicating structural phase transition is observed in ferriellectric crystal.

1.4. Author`s contribution

The author of this doctoral dissertation carried out all the experiments of dielectric, ferroelectric, pyroelectric and low-frequency noise characteriation, analyzed the results, prepared manuscripts of articles included into the thesis. The presentations that was presented by the author of the dissertation are underlined. However, a part of this research was done in colaborations with the partners and the scientific supervisor: the chemical synthesis of the investigated phosphorus chalcogenide single crystals and some theoretical modelling of hysteresis loops were performed at Uzhgorod University, Ukraine.

1.5. Approbation of the research results

This section presents the lists of papers and presentations related to the dissertation.

List of publications included into the thesis:

1. Zamaraite, I; Svirskas, S; Vysochanskii, Yu; Glemza, K; Banys, J; Dziaugys, A. Dielectric, pyroelectric and ferroelectric properties of lead-doped $Sn_2P_2S_6$ crystals, *Phase Transitions* 92 (5): 500-507 (2018).
2. Zamaraite, I; Yevych, R; Dziaugys, A; Molnar, A; Banys, J; Svirskas, S; Vysochanskii, Y. Double Hysteresis Loops in Proper Uniaxial Ferroelectrics. *Physical Review Applied* 10 (3): 034017 (2018).

3. Zamaraite, I; Matukas, J; Pralgauskaite, S; Vysochanskii, Y ; Banys, J; Dziaugys, A. Low-frequency noise characteristics of lamellar ferrielectric crystal $CuInP_2S_6$ at the phase transition, *Journal of Applied Physics* 112: 024101-1 (2017).
4. Zamaraite, I; Dziaugys, A; Banys, J; Vysochanskii, Y. Dielectric and electrical properties of $AgCrP_2S_6$ and $Cu_{0.2}Ag_{0.8}CrP_2S_6$ layered crystals. *Ferroelectrics* 515: 13-17 (2017).

Other publications:

5. Salak AN, Khalyavin DD, Zamaraite I, Stanulis A, Kareiva A, Shilin AD, Rubanik VV, Radyush YuV, Pushkarev AV, Olekhnovich NM, Starykevich M, Grigalaitis R, Ivanov M, Banys J. Metastable perovskite $Bi_{1-x}La_xFe_{0.5}Sc_{0.5}O_3$ phases in the range of the compositional crossover, *Phase Transitions* 90 (9): 831-839 (2017).
6. Pralgauskaite, S.; Matukas, J.; Grigalaitis, R.; Banys, J.; Zamaraite, I.; Vitajovic Petrovic, M.M.; Bobic, J.D.; Stojanovic, B.D., "Low frequency noise characteristics of $BaTiO_3$-$NiFe_2O_4$ composites at phase transition," in Noise and Fluctuations (ICNF), 2015 International Conference on , vol., no., pp.1-4.

1.6.List of presentations

Oral presentations:

1. I. Zamaraite, A. Dziaugys, R. Yevych, J. Banys, Yu. Vysochanskii „Nonlinear dynamics of phosphorous chalcogenide ferroelectrics with many-well local potentials“ – RCBJSF2018 Rusia, Saint Petersburg May 14-18, 2018
2. I. Zamaraite, A. Dziaugys, J. Banys, Yu. Vysochanskii „Investigation of Physical Properties of Phosphorous Chalcogenide Crystals“ – „New multiferroics and superionic conductors for acustoelectronics and solid state ionics“ Lithuania, Vilnius October 10, 2017.
3. I. Zamaraite, J. Matukas, S. Pralgauskaite, A. Dziaugys, Yu. Vysochanskii, J. Banys „Fluctuations properties near the ferroelectrci phase transition“ - "Modern Multifunctional Materials and Ceramics", Lithuania, Vilnius April 19-20, 2017.
4. I. Zamaraite, J. Matukas, S. Pralgauskaite, A. Dziaugys, Yu. Vysochanskii, J. Banys „ Low frequency noise characteristics of

ferroelektric materials“ – „Properties of ferroelectric and superionic systems“, Ukraine, Uzhgorod November 17-18, 2016.

Poster presentations:

1. I. Zamaraite, A. Dziaugys, J. Banys, Yu. Vysochanskii „Quantum Paraelectric State in $(Pb_ySn_{1-y})_2P_2S_6$“ – FMNT2018 Latvia, Ryga October 2-5, 2018
2. I. Zamaraite, A.V. Pushkarev, Yu.V. Radyush, N.M. Olekhnovich, A.D. Shilin, V.V. Rubanik, A. Stanulis, A. Kareiva, M. Ivanov, R. Grigalaitis, J. Banys, D.D. Khalyavin, A.N. Salak „Processing and Dielectric Properties of the $Bi_{1-x}La_xFe_{0.5}Sc_{0.5}O_3$ Metastable Perovskite Ceramics“ – CIEC16 Italy, Turin September 9-11, 2018.
3. I. Zamaraite, A. Dziaugys, J. Banys, Yu. Vysochanskii „Low Frequency Noise Characteristics of Phosphorus Chalcogenide Crystals“ – ECAPD2018 Rusia, Moscow July 25-28, 2018.
4. I. Zamaraite, A. Dziaugys, J. Banys, Yu. Vysochanskii "Influence of Se and Pb on dielectric and ferroelectric properties of $Sn_2P_2S_6$ crystals" - RCBJSF2016 Japan, Hiroshima May 27 – June 1, 2018.
5. I. Zamaraite, A. Džiaugys, J. Banys, D. G. Mandrus „Electrical conductivity investigations of lamellar crystals“ – FMNT2017, Estonia, Tartu April 24-27, 2017.
6. I. Zamaraite, J. Matukas, S. Pralgauskaite, A. Dziaugys, Yu. Vysochanskii, J. Banys „Low frequency noise characteristics of $CuInP_2S_6$ lamellar crystal“ – IMF-2017, USA, San Antonio September 4-8, 2017
7. I. Zamaraite, A. Konovalova, O. Ignatenko, A. Pushkarev, Yu. Radyush, N. Olekhnovich, A. Shilin, V. Rubanik, A. Stanulis, M. Ivanov, R. Grigalaitis, J. Banys, D. Khalyavin, A. Salak „Multiferroic ceramics of the $Bi_{1-x}La_xFe_{0.5}Sc_{0.5}O_3$ Metastable Solid Solutions System Prepared Using High Power Activation“ – Materiais 2017, Aveiro, Portugal April 9-12, 2017.
8. I. Zamaraite, A. Salak, J.Banys "Effects of La doping on dielectric and electrical properties of $Bi_{1-x}La_xFe_{0.5}Sc_{0.5}O_3$ ceramics,, - ISAF/ECAPD/PFM Conference, Darmstadt, Germany August 21-25, 2016.
9. I. Zamaraite, A. Salak, J.Banys, M. Ivanov "Dielectric spectroscopy characterization of $Bi_{1-x}La_xFe_{0.5}Sc_{0.5}O_3$ ceramics,, – Electroceramics XV, Limoges, France June 27-29, 2016.

10. I. Zamaraite, A. Dziaugys, J. Banys, Y. Vysochanskii "Influence of Se and Pb on dielectric and ferroelectric properties of $Sn_2P_2S_6$ crystals" - RCBJSF-IWRF Japan, Shimane June 19-23, 2016.

1.7.Layout of the dissertation

This doctoral dissertation is divided into five chapters:

INTRODUCTION

This chapter briefs about the background and motivation of the research work presented in the thesis along with the aim and objective.

OVERVIEW

This chapter contains a brief review of literature in the subject area under study. This review presents a detailed survey of previous published works on crystal structure, electrical properties, ferroelectric properties and optical properties of the phosphorous chalcogenide crystals family focusing on $M_2P_2X_6$-type crystals.

EXPERIMENTAL

The detailed preparation of investigated crystals growed by vapour transport and Bridgman methods has been described. Also, the various characterization methods and the parameters used to investigate the properties of the samples have been described and illustrated.

RESULTS AND DISCUSSION

In this chapter, the dielectric, ferroelectric and pyroelectric studies carried out for $M_2P_2X_6$-type crystals have been presented. In addition, the noise spectroscopy of lamellar phosphorous chalcogenide $CuInP_2S_6$ have been presented.

CONCLUSIONS

Here the results of the present doctoral dissertation are summarized with concluding remarks.

2. OVERVIEW

This chapter provides some general knowledge of structural phase transitions and ferroelectric materials. The remaining section of this literature overview focuses on phosphorus chalcogenide crystals family and reviews the literature over the period 1970-2018. This literature overview is not claimed to be comprehensive, it is structured chronically, and only specific topics are described in more details. The noise spectroscopy is also reviewed, and this topic is subdivided into two sections: general knowledge about noise spectroscopy and its applications in materials sciences.

2.1.General Knowledge of Ferroelectrics and Phase Transitions

2.1.1.General Properties of Ferroelectrics

Ferroic materials are characterized by a spontaneous order parameter that can be reversibly switched between two or more different orientation states via an applied external field. Another important feature of ferroic materials is the existence of the spontaneous order parameter in the absence of any external field. There are many common features among ferroic materials, such as the existence of domains [16] [17], which can be switched with respect to external fields; the appearance of hysteresis loops [18] [19] [20] [21]; etc.

A large class of ferroic materials is ferroelectrics, which are insulators possessing a spontaneous electric polarization switchable by an electric field. Ferroelectric phenomenon was first noticed in Rochelle salt and reported by Czech scientist Valasek in 1921 [22]. Actually, Rochelle salt was the only known material with ferroelectric characteristics for a long time. Thus, the ferroelectricity was considered a unique peculiarity and it did not draw much scientific attention. However a significant change has appeared after the discovery of ferroelectricity in $BaTiO_3$ ceramics in 1945 [23]. It was demonstrated for the first time that ferroelectricity could exist in oxide materials whose simple crystal structure stimulated theoretical work and practical applications. Since then ferroelectrics have been extensively studied and are nowadays realized in a wide range of applications [24].

Moreover, all ferroelectric materials exhibit not only ferroelectric phenomena, but also piezoelectric and pyroelectric effects, which can be used for many applications. The piezoelectricity, the generation of an electrical charge as a result of applied mechanical stress, occurs in all

noncentrosymmetric crystals. Pyroelectricity, the generation of an electrical potential due to the temperature change of the material, occurs in all crystals that belong to a polar symmetry class. Thus, ferroelectrics are a subgroup of pyroelectric materials which in turn is a subgroup of the piezoelectric materials. It has led to the vast application ranging from the micromechanical devices (ultrasonic sensors, actuators) based on the piezoelectric effect to infrared sensors based on the pyroelectric effect [25]. Besides piezoelectric and pyroelectric applications, optical, thermal and electrical properties of ferroelectrics are exploited in a number of devices, including nonvolatile high-density memories (FeRAM or FRAM) [18] [26]. Since FeRAM has excellent electric properties, such as a high speed read/write, high switching endurance and low power consumption in comparison with conventional FLASH memory, it has been applied to radio frequency identification (RFID) tags, advanced smartcards and authentication devices [27]. Memory applications of ferroelectrics are based on polarization switching and hysteretic *P-E* behavior.

2.1.2.Polarization Switching and Hysteresis Loops

Ferroelectric materials are characterized by a finite electric polarization in absence of an external electric field. Furthermore, this polarization must possess at least two stable states, and must have the ability to be reversibly switched from one state to another by applying an electric field. Thus, these regions with uniformly oriented spontaneous polarization vector may coexist within a ferroelectric sample, and are called *ferroelectric domains* [16]. The atomically sharp topological defects that separate the regions of uniform polarization (two domains) is called the *domain wall* [16]. The walls that separate domains with oppositely orientated polarization are called 180° walls and those which separate regions with mutually perpendicular polarization are called 90° walls [21]. The types of domain walls depend on the symmetry of both paraelectric and ferroelectric phases of the ferroelectric crystal [18]. Size of domains varies in wide limits, from tens of nanometers to millimeters; however, if a narrower region should be quoted as typical, linear dimension between 1 and 100 mm would seem a reasonable hint for the crystals, however, much smaller values are typical for thin films [17]. The presence of domains in a ferroelectric sample was demonstrated to affect macroscopic properties such as the dielectric susceptibility and piezoelectric response [16].

The domains in ferroelectric materials may be naturally present for energetic reasons. In this case the sample is usually called *polydomain*. In

contrast, samples presenting a uniform state of the order parameter are said to be *monodomain* [16]. An application of strong field could lead to the reversal of the polarization in the domain, known as *domain switching* or *polarization reversal*. A consequence of the switching in ferroelectric materials is the occurrence of the ferroelectric (*P-E*) hysteresis loop as shown in Fig. 1. The value of polarization at zero field (point D) is called the *remnant polarization*, P_r. The field necessary to bring the polarization to zero is called the *coercive field*, E_C. The *spontaneous polarization* P_S is usually taken as the intercept of the polarization axis with the extrapolated linear segment CD (Fig. 1). Since ferroelectrics usually possess ferroelastic domains (with the exception of $LiNbO_3$, which only has 180° ferroelectric domains), spontaneous strain is also induced with the external electric field simultaneously [19]. Therefore, if the strain is monitored as well as the polarization, a strain–electric field curve (butterfly-like) can be observed (Fig. 1).

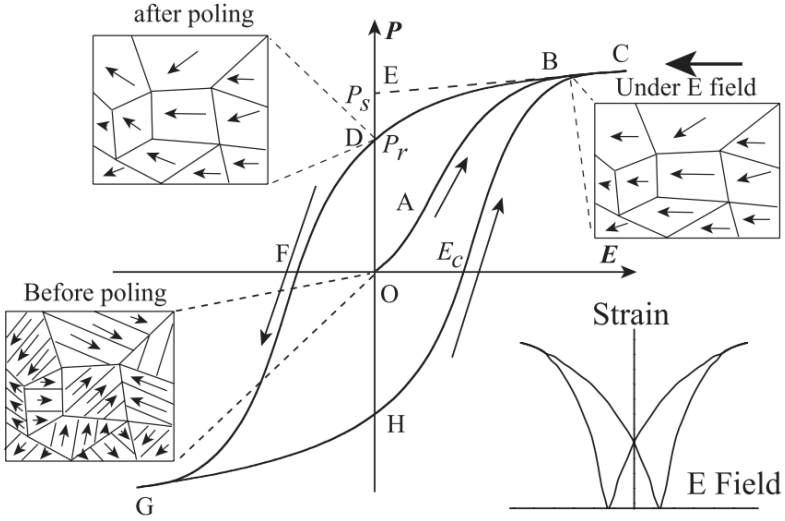

Fig. 1. A typical hysteresis loop in ferroelectrics and corresponding domain reversal (polarization switching) and strain–electric field curve [19].

The first electronic circuit to measure the ferroelectric hysteresis loop in Rochele salt was created by C. B. Sawyer and C. H. Tower. It has been in use for more than sixty years. Nowadays, *P-E* hysteresis loops can be easily carried out by commercial apparatus available mainly from two companies, AixACCT TF Analyzer and Radiant Precision Pro. In these equipements the current is measured, and after integration with compensation by variable

resistor, the polarization hysteresis loops can be obtained. Although the experimental equipement is not the obstacle to study the *P-E* relationship in ferroelectrics, interpreting the loops is much more chalenging [19]. In principle, every ferroic material possesses a unique hysteresis loop, related to its properties and structures [19]. For ferroelectrics, many characteristic parameters, such as coercive field, spontaneous, and remnant polarizations can be directly extracted from the hysteresis loops. Furthermore, many impact factors, including the effect of materials (grain size and grain boundary, phase and phase boundary, doping, anisotropy, thickness), aging (with or without poling), and measurement conditions (applied field amplitude, fatigue, frequency, temperature, stress), can affect the hysteretic behaviors of the ferroelectrics [19]. The study of the hysteresis loops, is one of the most important tools to investigate the behavior and to assess the properties of ferroelectric materials. Therefore, only appropriate hysteresis analysis allows to separate the various contributions and extract reliable values of the quantities of interest [20]. As reported in the famous article „Ferroelectrics go bananas“, leaky dielectrics or even ordinary bananas exhibit misleading „hysteresis“ loops which have very little in common with ferroelectricity [28]. Cautions were made to avoid some misinterpretation, normaly due to the coexistence of conductivity and polarization in the same material [29]. For a normal ferroelectric hysteresis loop, it should be saturated and has a region in *Q-V* loop that is concave [28]. Only an appropriate procedure of analysis and well-designed measurements test allow reliably extract the contribution of the measured hysteresis loop associated to different ferroelectric phases in a material and avoid misinterpretation of data [19] [20] [29] [30].

Recently the ferroelectric loops were categorized into four groups based on the morphologic features: classic hysteresis loops, double hysteresis loops, asymmetric hysteresis loops and slim hysteresis loops [19].

Classic hysteresis loop is the most popular ferroelectric loop possessing main features that is presented in Fig. 2(a). An ideal hysteresis loop is symmetrical so that $+E_C = -E_C$ and $+P_r = -P_r$ [21]. It is worth to mention that there are important differences in the hysteresis loops measured on polycrystalline or single crystal ferroelectric materials of similar composition [18] [19] [21]. This phenomena is mainly attributed to the clamping effect of domains with respect to grain boundaries [19]. The most striking difference appears by applying the same electric field on the polycrystalline and single crystal materials of the same composition: the

polarization switching is much easier in crystals than in ceramics, owing to the absebce of grain boundaries [19].

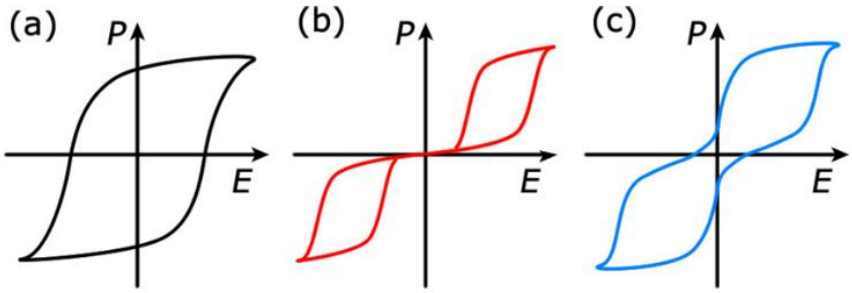

Fig. 2. Schematic representation of three types of *P-E* loops. (a) Single loop typically found in ferroelectrics, (b) double hysteresis loop with zero remnant polarization, as characteristic of antiferroelectric compounds, and (c) pinched hysteresis loop with finite but small remnant polarization [31].

Antiferroelectrics (AFE) can be characterized by an antipolar crystal structure with two nearby crystalline sublattice with the oppositely directed dipoles [32] [33] [31] [34]. This crystalline arrangement results in the *double hysteresis loops* of antiferroelectrics as depicted in Fig. 2(b) [19] [34]. Needless to say, more precise definition of antiferroelectrics has been managed to extended [32]. According to the textbook by Lines and Glass [24], an antiferroelectric „exhibits large dielectric anomalies near the phase transition temperature and which can be transformed to an induced ferroelectric phase by an application of an electric field“. In the earliest studies of ferroelectricity, it was generally accepted that the double hysteresis loop is an intrinsic mark of antiferroelectricity [32]. Surprisingly, double *P-E* curves have been found not only in antiferroelectric materials, e.g., $Pb(Zr,Ti)O_3$ (PZT) [35], $BaTiO_3$ ceramics [36] and other $BaTiO_3$-based ceramics [37]. Such a kind of curve is illustrated in Fig. 1(c), and is typically identified as a “pinched” hysteresis loop, which is similar to the double loop as observed in AFE [31]. Sometimes, observed pinched loops are misinterpreted to be double (antiferroelectric) hysteresis loops [31]. However, the pinched hysteresis loops and double hysteresis loops have different physical origins. Double hysteresis loop stems from two phases of antiferroelectrics, including stable antiferroelectric phase and field-induced metastable ferroelectric phase [19]. Whereas it is commonly believed that the existence of the pinched loops requires some types of inhomogeneity and structural defects in the material [35], such as domain walls being strongly

pinned by defects [31]. Other factors leading to a pinched hysteresis loop include aging (degradation with time in the absence of an external electrical loading) of ferroelectric sample and fatigue (degradation during electrical loading) [19] [38]. The underlying mechanisms of aging and fatigue processes are similar and mainly related to the presence of mobile charge species, such as defects or defect dipoles, which usually stabilize the domain pattern and decrease the domain wall contribution to the polarization response [38]. The microscopic mechanisms causing aging and fatigue of ferroelectrics are still under discussion. Carl and Härdtl [39] suggested three mechanisms: volume effect, domain effect and grain boundary effect (Fig. 3). It is worth noting that classic ferroelectric hysteresis loop also can be observed in samples with pinning centers, if the aging state is disturbed, e. g., when the sample is quenched from high-temperature paraelectric state [19].

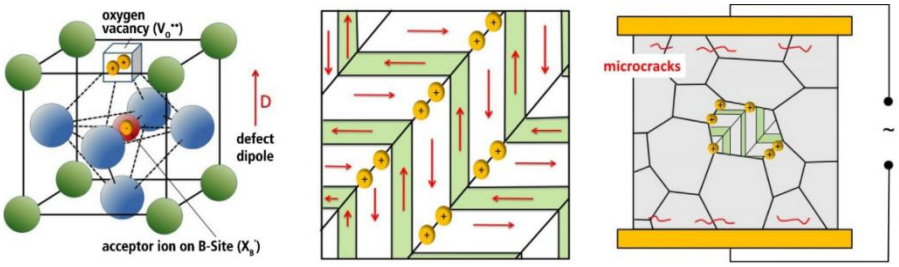

Fig. 3. Classification of the different domain stabilization mechanisms according to their length scales [38].

Hysteresis loops of the poled hard ferroelectrics exhibit an asymmetric shape [19] [38]. Such an asymmetric shape is related to the existence of an internal bias field [24]. Therefore, ferroelectric materials with higher internal bias are desirable for high power electromechanical applications [19] [24].

It is commonly acknowleged that the hysteresis phenomena is caused by the domain wall motion [21] [24]. Relaxor ferroelectrics posses only microdomains or polar nanoregions (PNRs) instead of the macroscopic domains [40]. Due to their much smaller characteristic size, microdomains response to the external field much faster than macroscopic domains and frequently result in a *slim hysteresis loop*, which is not so obvious [19].

2.1.3.Structural Phase Transitions and Critical Phenomena in Crystals

L. D. Landau constructed a general theory of secon-order phase transition, in which he introduced the concept of spontaneous broken symmetry [41]. Landau was the first to propose a phenomenological expression for the free energy as a Taylor expansion series in the vicinity of the critical temperature T_C, i.e. Curie temperature [42].

Continuous (also known as *second-order*) phase transitions occur when a new state of reduced symmetry develops continuously from the disordered (high-temperature) or symmetric phase as the temperature is reduced [43]. A phase transition is associated with a change of certain symmetry. The ordered phase typically has a lower symmetry than the disordered phase [44]. Landau introduced a phenomenological *order parameter* η that characterizes the degree of ordering when a phase transformation takes place on lowering, e.g., the temperature [45]. The variation of order parameter of second-order phase transition with temperature is depicted in Fig. 4. The order parameter lies within the range of values 0 and 1 (see figure) corresponding respectively to total disorder at high temperature and complete ordering at low temperature. The transition from η = 1 to 0 is continous, but involves a singularity as $T \rightarrow T_C$ [46]. At *first-order phase transitions*, the order parameter jumps discontinously at the transition temperature, typically T_C, from 0 to a finite value.

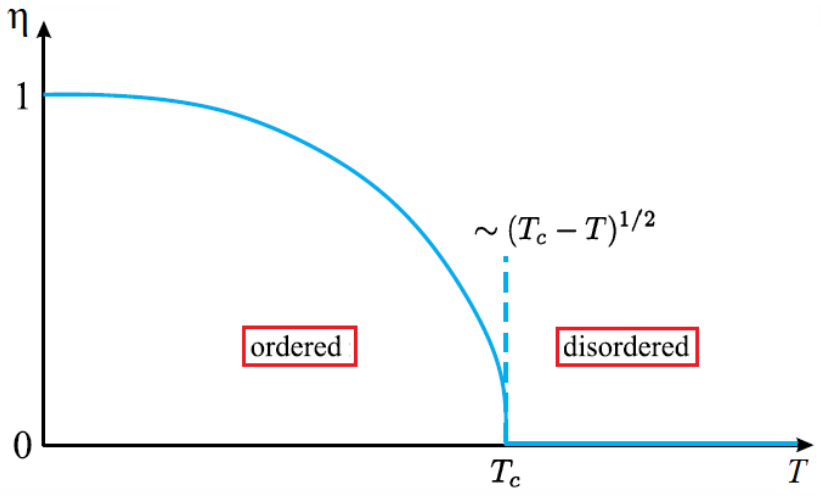

Fig. 4. Schematic representation of the temperature dependence of the order parameter η.

The important three classes of primary ferroics are ferroelectrics, ferromagnets and ferroelastics. In these ferroics the order parameter is some physical quantity providing thermodynamic information about the properties of material [44]. The spontaneous electric polarization P_S, already mentioned earlier, is considered to be an order parameter in ferroelectrics. In analogy with ferroelectrics, the spontaneous magnetization M_S can be defined as the order parameter of ferromagnetic materials. The spontaneous strain behaves as the order parameter of ferroelastics. Multiferroics refer to a big class of materials which exhibit simultaneously more than one ferroic order parameter in a single phase [47].

V. L. Ginzburg developed the first phenomenological theory of ferroelectricity based on the Landau theory of second-order phase transitions and a similar treatment was developed by Devonshire shortly thereafter [48]. Second-order phase transition can be described in the framework of Landau theory by writing a Gibbs thermodynamic potential as a polynomial expansion in the relevant order parameter η:

$$\Phi = \Phi_0 + \frac{\alpha}{2}(T - T_C)\eta^2 + \frac{\beta}{4}\eta^4 + \frac{\gamma}{6}\eta^6 + \cdots - E\eta, \qquad (1)$$

where Φ_0 is the equilibrium value at T_C, η is the order parameter and the expansion coefficients α, β and γ are in general temperature and pressure dependent. In the Landau theory of second-order phase transition, the expansion coefficients α and β should be limited to positive values, and γ=0.

The equilibrium condition is given by minimization of the Gibbs thermodynamis potential Φ with respect to η:

$$\frac{\partial \Phi}{\partial \eta} = 0, \qquad \frac{\partial^2 \Phi}{\partial \eta^2} > 0. \qquad (2)$$

Applying the equilibrium conditions to the polynomial expansion in the absence of external field (E = 0), we obtain the equilibrium value of the order parameter $\eta_0 = 0$ for $T > T_C$ and

$$\eta_0 = \pm\left(\frac{\alpha(T_C - T)}{\beta}\right)^{1/2} \quad \text{for } T < T_C \qquad (3)$$

Derivatives of the Landau free energy with respect to temperature, pressure, electric field, and other thermodynamic variables provide information about the heat capacity, heat, entropy, susceptibility, etc.

The equilibrium value of the order parameter shows the typical result that at the second order phase transition there is no jump in the order parameter and no latent heat of transition. The first-order phase transition is accompanied by a small but finite jump of the order parameter η and a transition enthalpy. Another typical feature of the first-order phase transition is the temperature hysteresis and the cioexistence of metastable phase in the vicinity of the transition temperature T_C. Many ferroelectrics exhibit a special kind of first-order phase transition with a change of symmetry from group to a subgroup, which is close to the situation in the second-order, and can be sufficiently bescribed by Landau theory. In this case, the terms up to the sixth order must be taken into account in the expansion of free energy.

Landau theory has been succesfully adapted to a numerous examples of phase transitions. On the other hand, the Landau theory of phase transitions is not applicable at the phase transition (critical) temperature. The major criticism of the Landau theory can be summarized as follows: thermal fluctuations are neglected in the Landau theory; however, near the critical temperature, thermal fluctuations become important and render the Landau theory inaccurate [26].

Continuous phase transitions are often synonymous with *critical phenomena*, i.e. anomalous phenomena that appears at the critical point. Critical phenomena include scaling relations among different quantities, power-law divergences of some quantities described by critical exponents, universality classes [49]. Reduced temperature $t = (T\text{-}T_C)/T_C$ are introduced in the theory of critical behavior to critical exponents, which describe the behavior of physical quantities in terms of power law near continuous phase transitions. The smaller the reduced temperature *t*, the better is the description of the critical behavior. The critical behavior has been studied comparing the critical parameters found with the Landau mean-field theory or with different universality classes predicted by renormalization group analysis. Each universality classs corresponds to a particular hamiltonian in which different physical mechanisms are taken into account and to a different set of the critical parameters α (associated to specific heat), β (associated to spontaneous polarization) and γ (associated to the inverse of dielectric susceptibility) through the equations:

$$c_p(T) \sim A^{\pm}|t|^{-\alpha} \quad (A^- \; for \; T < T_C, A^+ \; for \; T > T_C) \tag{4}$$

$$P_S(T) \sim |t|^{-\beta} \quad (T < T_C) \tag{5}$$

$$\chi^{-1}(T) \sim |t|^{\gamma} \quad (T > T_C) \tag{6}$$

which are fulfilled in the critical region, where fluctuations of the order parameter are relevant. A summary of all universality classes corresponding to the different set of the crical parameters can be found in Ref. [50]

Scaling analysis theory assesses that all those critical exponents are interrelated $\alpha + 2\beta + \gamma = 2$; $\delta = 1 + \gamma/\beta$.

2.2.Structure and Phase Diagram of Phosphorus Chalcogenide Family

2.2.1.Crystalline Structure and Phase Transitions of $Sn(Pb)_2P_2S(Se)_6$

Single crystals of thio-phosphates and thio-hypodiphosphates succesfully were grown by vapor transport with iodine in 1970 [51]. One of these compounds was $Sn_2P_2S_6$, which was presented for the first time. The crystal structure of $Sn_2P_2S_6$ was refined in a sequence of measurements [1] [52] [53]. Nitsche and Wild conducted $Sn_2P_2S_6$ single crystal structure determination and reported the monoclinic latttice with constants: a=6.43 Å; b=7.47 Å; c=11.03 Å; β=122.2° [51]. Later in 1974, Carpentier and Nitsche carried out an experiment to a greater extent on $Sn_2P_2S_6$ single crystal [1]. It was found that at room temperature, $Sn_2P_2S_6$ has a non-centrosymmetric monoclinic structure corresponding to space group P*c*. The elementary cell is made up of two formula units (Z=2) with the lattice parameters as follows: a=9.378 Å; b=7.488 Å; c=6.513 Å; β=91.15° [52].

Structure analysis of $Sn_2P_2S_6$ at ambient temperature (Fig. 5) determined typical $(P_2S_6)^{4-}$ anion clusters that are connected to a three-dimensional network by Sn^{2+} cations [52]. The $(P_2S_6)^{4-}$ anion clusters consist of PS_3-PS_3 deformed trigonal prisms interlinked together by covalent bonds P-P and P-S (at room temperature distances of bonds are 2.211(9) Å and 2.0 Å, respectively [53]). The $(P_2S_6)^{4-}$ anions are tied together via S-Sn ionic bonds (length of bonds is equal to 8.690 Å [53]). These bonds result in an eightfold coordination sphere of sulfur atoms about each Sn atom, which may be roughly described as a bicapped trigonal prism. There are two inequivalent Sn sites in the room temperature structure; one is seven coordinate, while the other is eight coordinate [53].

It was demonstrated dy differential thermal analysis (DTA) that above approximately 333 K the crystal undergoes a transition into monoclinic phase described by a space group $P2_1/c$ [1]. The phase transition was suggested to be of the second order [53]. The changes in $Sn_2P_2S_6$ structure

between the paraelectric (at 110°C) and ferroelectric (at room temperature) phases have been well studied by Scott and co-workers [53]. In the 110°C structure (paraelectric phase) the length of P-P and P-S bonds are rougly the same with the S and P atoms occupying essentially the same positions in both phases. The most striking differences between paraelectric phase and ferroelectric phase were found mainly in the tin positions. At elevated temperature, all the Sn atoms occupy crystallographically equivalent eightfold coordination sites [53]. At elevated temperatures, the Sn-S distances vary between 2.91 Å and 3.23 Å, maintaining the inversion symmetry around a midpoint between two Sn atoms [53] [54]. Upon transition to the ferroelectric phase, pairwise displacements of the tin atoms along the *a*-axis relative to the rigid $(P_2S_6)^{4-}$ group result in a lost of the inversion symmetry and twofold axis [53] [54] [55]. X-ray structural studies indicated that the phase transition is mainly displacive type with tin displacements serving as the order parameter [53]. The unit cell of the $Sn_2P_2S_6$ crystal contains two formula units (Z=2) in both phases [56].

The changes in the crystal structure between ferroelectric and paraelectric phases are quite small. Structural changes occuring by isovalent substituting sulfur by selenium or tin by lead are more considerable. The crystal structures of $Sn_2P_2Se_6$, $Pb_2P_2S_6$, $Pb_2P_2Se_6$ and their solid solutins $(Pb_ySn_{1-y})_2P_2(Se_xS_{1-x})_6$ are isomorphous with the high-temperature paraelectric phase of the previously reported $Sn_2P_2S_6$ single crystals. The crystallographic data of these compounds was studied, analyzed and summarized in [1]. X-ray studies showed that all these isostructural compounds crystallize in the monoclinic system.

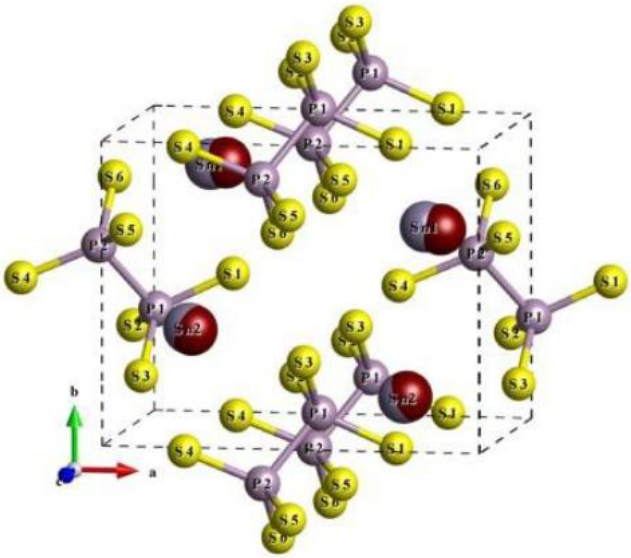

Fig. 5. The crystal structure of $Sn_2P_2S_6$ ferroelectric phase [57]. The tin atoms positions in the paraelectric phase are shown by red spheres

The substitution of sulfur by selenium in the anion sublattice in $Sn_2P_2(S_{1-x}Se_x)_6$ solid solutions results in a decrease in the phase transition temperature and and the appearance of an intermediate incommensurate (IC) phase. $Sn_2P_2(S_{1-x}Se_x)_6$ family of phosphorous chalcogenide ferroelectrics is an excellent system for studying the appearance of an intermediate incommensurate phase, since mixed crystals can be grown for all values of x ($0<x<1$). $Sn_2P_2Se_6$ exhibits three phases and shows an intermediate IC at ambient pressure, in contrast to $Sn_2P_2S_6$. Selenide compound has been less studied that the sulfide, but again the appearance of an incommensurate phase in $Sn_2P_2Se_6$ makes it of fundamental interest. Only a few structural studies have been performed on $Sn_2P_2Se_6$ [58] [59] [60]. In the selenide compound the structural arrangement in the incommensurate phase has been analyzed qualitatively [61]. The structure of paraelectric phase has been previously detemined by Voroshilov *et al.* [58]. The differences of structure between paraelectric and ferroelectric phases of $Sn_2P_2Se_6$ were reported in the literature [59][60]. The crystallographic data of $Sn_2P_2Se_6$ presented in thsese papers are in good agreement. The room temperature phase of $Sn_2P_2Se_6$ belongs to $P2_1/c$ with two formulas per unit cell (Z=2) [58] [59] [56]. It is isomorphous with the high-temperature paraelectric phase of $Sn_2P_2S_6$. However, the phase transition to an intermediate incommensurate

phase [61] occurs at 220 K and then to a commensurate ferroelectric phase of the space group P*c* with Z=2 at 196 K [56]. The low-temperature phase is isomorphous with the room temperature ferroelectric phase of $Sn_2P_2S_6$.

The values of the unit cell parameters of $Sn_2P_2Se_6$ are as follows: a=6.805(1) Å, b=7.708(2) Å, c=9.616(5) Å, β=91.03(5)°, V=504.4(3) $Å^3$ at 150 K (ferroelectric phase labelled as FE-$Sn_2P_2Se_6$); a=6.815(1) Å, b=7.671(3) Å, c=9.626(4) Å, β=91.01(4)°, V=503.2 $Å^3$ at 293 K (paraelectric phase labelled as PE-$Sn_2P_2Se_6$) [60]. Three-dimensional represntations of $Sn_2P_2Se_6$ structures in the ferroelectric and paraelectric phase are shown in Figs. 6 and 7, respectively. The PE-$Sn_2P_2Se_6$ network is built up by $[P_2Se_6]$ anionic groups linked by Sn^{2+} cations. Within the $[P_2Se_6]$ group each P atom is fourfold coordinated, forming PSe_3 units associated in pairs via a P-P coordination bond. The selenium atoms form an octahedron, the two PSe_3 units being exactly in a staggered position (center of symmetry on the P-P bond). The $[P_2Se_6]$ groups are disposed in coordination octahedra and the Sn^{2+} atoms are surrounded by eight Se atoms forming a bicapped trigonal prism (BTP). The tin atoms shows an eightfold coordination, the selenium atoms being at the corners of a bicapped trigonal prism BTP [60]. The FE-$Sn_2P_2Se_6$ structure shows a similar general network architecture but upon the ferroelectric phase transition $[P_2Se_6]$ group loses its crystallographic center: in the FE phase P atoms are no more related by inversion [60].

The P-P bond lengths in the ferroelectric and paraelectric phases are nearly the same. The P-Se bond lengths also differ only slightly for the ferrroelectric and paraelectric phase [59]. The interatomic distances and angles in both phases are accuratelly determined in [59] and [60]. The most striking difference occurs at the level of the Sn coordination: displacement of the Sn atoms produce a macroscopic polarization in the ferroelectric phase [60]. Nevertheless, since the structural studies showed the ferroelectricity in this material are mainly connected with atomic displacements, a slight order-disorder character in the close neighbourhood of the transition point cannot be completely excluded from the structure data [60]. A first-principles study of the ferroelectric phase of $Sn_2P_2Se_6$ approved the existence of isolated Sn^{2+} cations ionically bonded with the $[P_2Se_6]$ group as the main characteristic of $Sn_2P_2Se_6$ structure [62]. The spontaneous polarization has been estimated on the order of ~15 μC cm^{-2} [62]. The obtained structures of $Sn_2P_2Se_6$ and structural changes related to the phase transitions have much in common with those observed for the crystal structure of $Sn_2P_2S_6$.

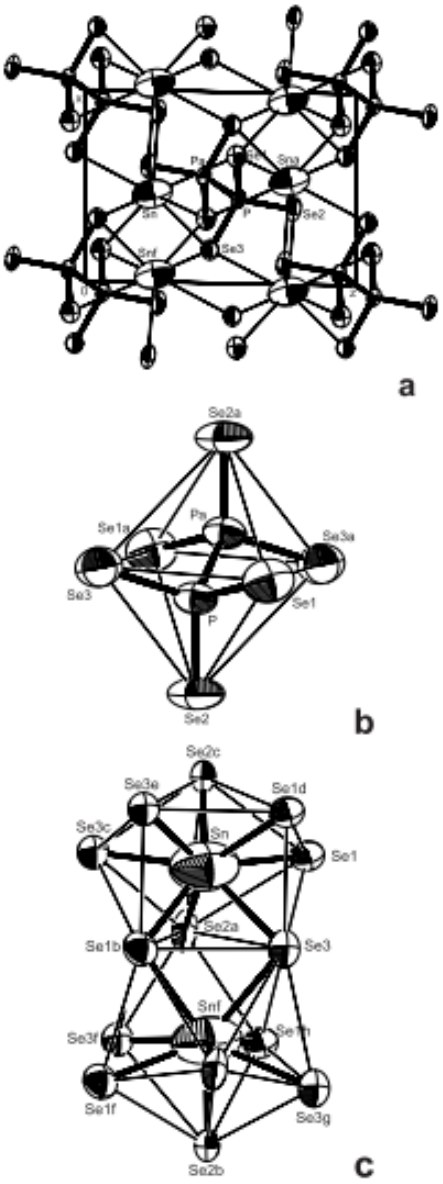

Fig. 6. PE-$Sn_2P_2Se_6$ structure [60]

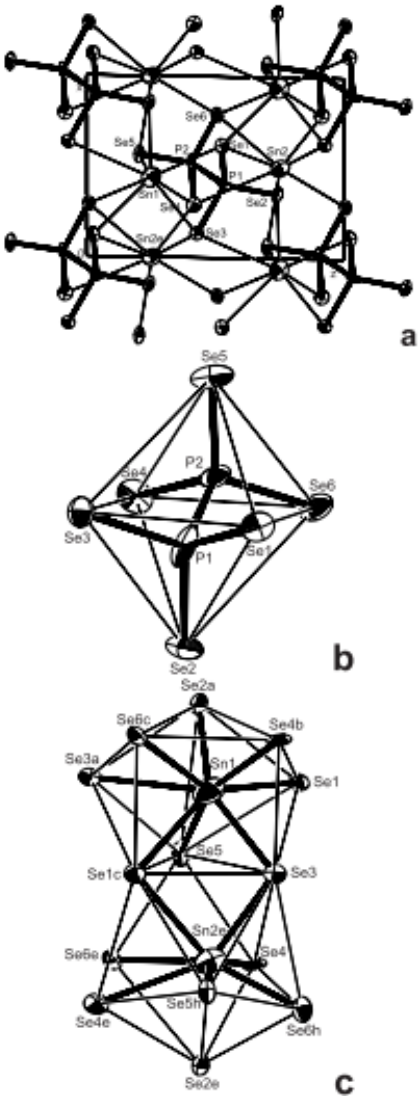

Fig. 7. FE-$Sn_2P_2Se_6$ structure [60]

At the room temperature $Pb_2P_2S_6$ and $Pb_2P_2Se_6$ are isotypic to the monoclinic modification II of $Sn_2P_2S_6$ [63]. In the first structural study [1], the $P2_1/c$ space group was reported for $Pb_2P_2S_6$ crystals, but later an acentric P*c* structure at room temperature was proposed [63]. Experimental pyroelectric and piezoelectric studies support the former conclusion about the centrosymmetric structure of $Pb_2P_2S_6$ crystal at room temperature [64]. $Pb_2P_2S_6$ and $Pb_2P_2Se_6$ are thio(seleno)phosphates compounds with Pb^{2+} cations bonded to ethane-like $[P_2S(Se)_6]^{4-}$ anions [2].

Their crystalline structures are similar to the presented above for $Sn_2P_2S_6$ in the paraelectric phase (Fig. 5). They differ only in the volume of the unit cell, due to the difference in the sizes of the ions which provoke a change in the crystal lattice parameters [64] [65]. The replacement of tin by lead leads to an increase in the unit cell volume from from 462 $Å^3$ to 513 $Å^3$ for $Pb_2P_2S_6$ and $Pb_2P_2Se_6$, respectively. $Pb_2P_2S_6$ crystallizes in the monoclinic system with the lattice constants a=6.612 Å, b=7.466 Å, c=11.349 Å, β=124.09° [66]. The lattice parameters of $Pb_2P_2Se_6$ at the room temperature and the atmospheric pressure are as follows: a=6.606 Å, b=7.464 Å, c=11.3346 Å and β=91.33° [1]. $Pb_2P_2S_6$ and $Pb_2P_2Se_6$ crystals remain in the centrosymmetric phase ($P2_1/c$) till 0 K [64].

2.2.2.The General Shape of the Phase Diagram of $Sn(Pb)_2P_2S(Se)_6$

From the first synthesis and structural study of $Sn(Pb)_2P_2S(Se)_6$ crystals by Nitsche and Wild [51], till present days, much attention has been devoted to investigations of the phase diagram of theses solid solutions. The phase diagram of $Sn(Pb)_2P_2S(Se)_6$ is considerably interesting due to the presence of an intriguing phenomena – the Lifshitz point (LP) [67]–[69]. Only a few materials with Lifshitz points on the phase diagram have been found: several studies have suggested LP on the temperature-magnetic field (*T-H*) diagram of MnP [70] and on the temperature-composition (*T-x*) diagram of $Sn_2P_2(Se_xS_{1-x})_6$ ferroelectrics [71].

$Sn_2P_2S_6$ crystal is a uniaxial proper ferroelectric with a three-well local potential for order parameter fluctuations [72].

The ferroelectric phase transition of $Sn_2P_2S_6$ crystal is induced by the stereoactivity of the Sn^{2+} cation $5s^2$ electron lone pair: the antibonding mixing of tin and sulfur orbitals (5*s* and 3*p*, respectively) interacts with the tin 5p orbitals, generating lower energy filled states Sn 5*p* (Sn 5*s* + S 3*p*). This formation of the Sn^{2+} lone pair electron cloud, together with the deformation of the nearest polyhedron formed by the sulfur atoms, determines the origin of the spontaneous polarization [57], [72], [73]. Microscopic origin of ferroelectric lattice instability in $Sn_2P_2S_6$ was described as second-order Jahn-Teller effect and their thermodynamics was considered in a frame of Blume-Emery-Grffiths (BEG) model with two order parameters (dipolar and quadrupolar) and three possible values of pseudospin: -1, 0, +1 [74] [75]. This model predicts the possibility of a tricritical points (TCP) in phase diagram. The existence of tricritical point (TCP) in the $Sn_2P_2S_6$ phase diagram under hydrostatic pressure was expected

earlier. The analysis of ultrasound anomalies showed an evidence of tricritical behavior of the $Sn_2P_2S_6$ crystal at p=0.4 GPa and T=250K [76]. At this point $Sn_2P_2S_6$ changes its character to the first order. Experimental measurements indicate that $Sn_2P_2S_6$ undergoes a second-order phase transition at $T_C \approx 337$ K. Substituting sulfur by selenium leads to a smooth splitting of the phase transition into a first order (solid line on Fig. 8) and second order (dashed line) phase transition lines. The Lifshitz point (LP) at which the paraelectric, ferroelectric and incommensurate (IC) phases coexist is reached at x_{LP}=0.28. As the result, $Sn_2P_2Se_6$ crystal exhibits a sequence of phase transitions: at $T_i \approx 220$ K, from the paraelectric to the IC phase, and at $T_C \approx 192$ K, from the IC phase to the ferroelectric phase [77]. In $Sn_2P_2(Se_xS_{1-x})_6$ mixed crystals TCP exists at x=0.6 which is virtual, which is not materialized because at $x = 0.27$ a Lifshitz point appears.

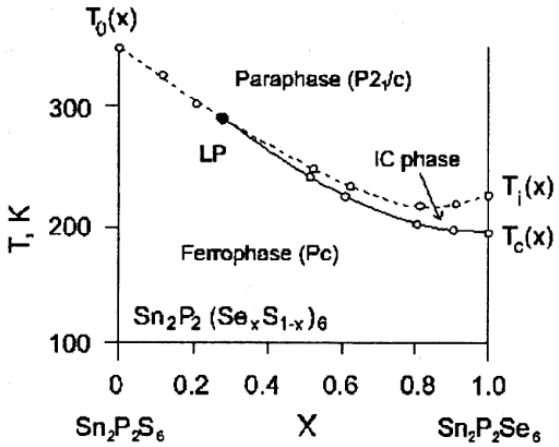

Fig. 8. Phase diagram of $Sn_2P_2(Se_xS_{1-x})_6$ mixed crystals. LP – Lifshitz point; dashed line – second order phase transitions; solid line – first order phase transitions [78].

The nonequilibrium properties of proper uniaxial $Sn_2P_2(Se_xS_{1-x})_6$ ferroelectrics with the type II incommensurate phase above Lifshitz point $x_{LP} \approx 0.28$ has been studied by dielectric investigation [79] which have been performed in cooling and heating regimes with the different rates 0.002–0.1 K/min, as well as high-resolution ultrasound investigation and hypersound Brillouin scattering experiments. From the temperature anomalies of reciprocal dielectric susceptibility, the transitions at $T_i(x)$ and $T_C(x)$ have been observed for compositions x=0.28, 0.40 and 1.0 indicating the presence of a true IC phase (Fig. 9).

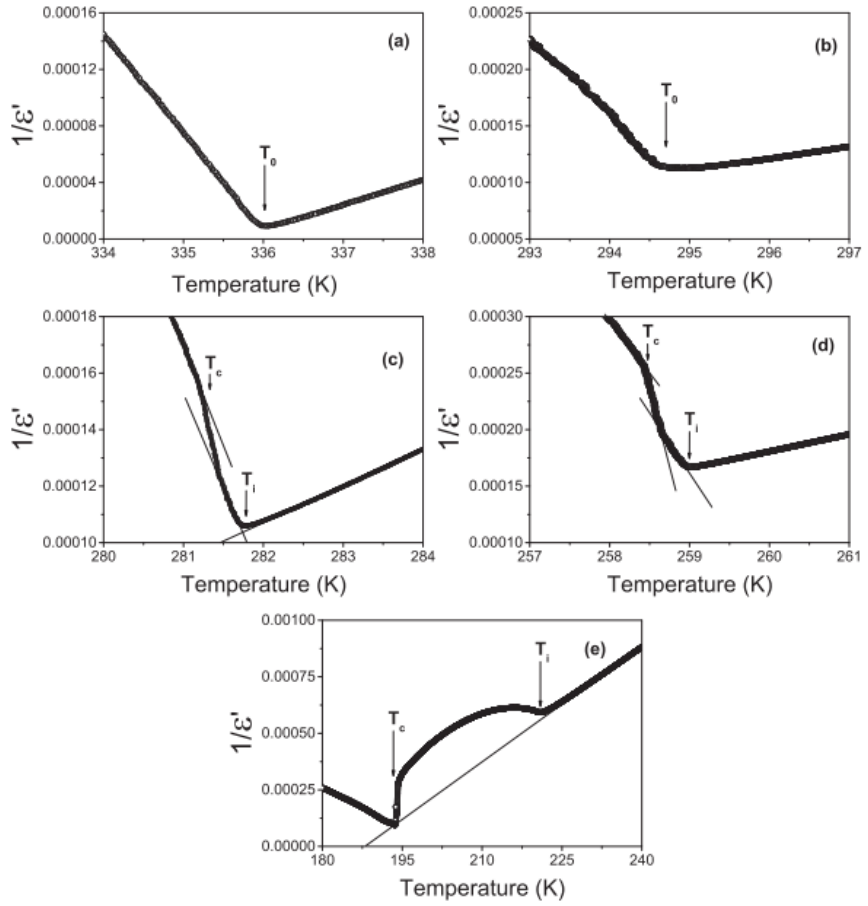

Fig. 9. Temperature dependence of reciprocal dielectric susceptibility of $Sn_2P_2(Se_xS_{1-x})_6$ mixed crystals: (a) x=0, (b) x=0.22, (c) x=0.28, (d) x=0.4, (e) x=1 [79].

According to the high-resolution ultrasound velocity and hypersound Brillouin scattering data, in a crystal with x=0.28 the intermediate state is still observed between the paraelectric and the ferroelectric phases. It gives an evidence that the position of LP in $Sn_2P_2(Se_xS_{1-x})_6$ mixed crystals should be localized somewhere in the range $0.22<x<0.28$. According to a high-resolution dielectric data, the IC state is observed in an interval of about 0.2 K at a cooling speed of 5 mK/min, while at a higher rate 100 mK/min the kink in the dielectric susceptibility at T_C is completely smeared and the curve is being similar to the one at Se concentration of x=0.22. Such a smearing is related to some space interference of the long-period modulation wave with

regular domain structure with very high concentration of domain walls concentration in the ferroelectric state whose size increases at higher cooling rates. This effect can be explained within the theory of Kibble-Zurek model, where in the case of the uniaxial ferroelectrics the domain walls in a sample could be considered as scalar topological defects [80], [81]. As was estimated in ref. [79], at a cooling rate of 0.1 K/min, the biggest value of domain size is about 50 nm, which is comparable to the modulation wavelength in the vicinity of LP.

The phase transition temperatures of $(Pb_ySn_{1-y})_2P_2S_6$ has been first investigated by dielectric measurements [82], [83]. $Pb_2P_2S_6$ has been found to form a solid solution with $Sn_2P_2S_6$ over the entire concentration range, resulting in the production of $(Pb_ySn_{1-y})_2P_2S_6$ mixed crystals [49]. It is interesting to understand the evolution of the ferroelectric phase transition with substitution of tin by lead in $(Pb_ySn_{1-y})_2P_2S_6$ solid solutions as lead ocupies the place of tin which is responsible for ferroelectric phase transition. The high resolution ac photopyroelectric calorimetry, dielectric and ultrasonic spectroscopy was applied to determine the compositional dependence of the ferroelectric phase transition temperature in $(Pb_ySn_{1-y})_2P_2S_6$ mixed crystals [50][63]–[66] [67] [68]. As a general trend, it was observed that the ferroelectric-paraelectric phase transition temperature decreases as the lead concentration in the $(Pb_ySn_{1-y})_2P_2S_6$ system is increased. The reason for this behavior is a weaker hybridization due to a bigger difference between Pb 6*s* and S *p* states By increasing lead content, the phase transition temperature goes down to 4.2 K in $(Pb_{0.61}Sn_{0.39})_2P_2S_6$ [75]. This was interpreted as follows: in the $(Pb_ySn_{1-y})_2P_2S_6$ system the smaller ionic radius tin ions is mixed by the larger ionic radius lead ions, and so this addition of lead increases the space for tin ions in the mixed single crystals. In this case it should be noted that in the $Sn_2P_2S_6$ crystals the motion of the tin ions is the leading force of the displacive type phase transition [83]. Therefore, the phase transition in the $(Pb_ySn_{1-y})_2P_2S_6$ solid solutions were suggested to be of a second order type up to $y\approx0.66$. It was constructed rather simple well-known phase diagram of $(Pb_ySn_{1-y})_2P_2S_6$ with neither a LP, nor an IC phase in contrast to the phase diagram of $Sn_2P_2(S_{1-x}Se_x)_6$ mixed crystals (Fig. 10).

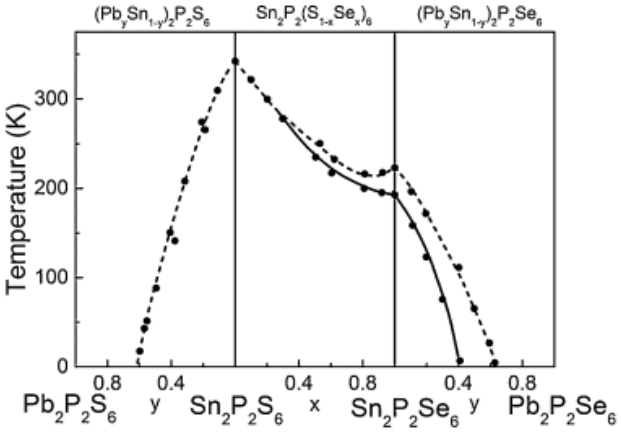

Fig. 10. Phase diagram of the $(Pb_ySn_{1-y})_2P_2(S_{1-x}Se_x)_6$ system. The dashed lines indicate the second order PT, the solid lines - the first order PT [84].

In Refs. [65], [85] it was presented dielectric and ultrasound studies performed of $(Pb_ySn_{1-y})_2P_2S_6$ ferroelectric family assessing that the phase diagram of these compounds is more complicated comparing to the presented above. A crossover has been observed in $(Pb_xSn_{1-x})_2P_2S_6$ from a non-mean field model at x=0.1 to a mean-field behavior at x=0.3 [84]. Besides, an anharmonic quantum oscillator (AQO) model has been proposed for a *T-p* diagram of $Sn_2P_2S_6$ single crystal and a *T-y* diagram of $(Pb_ySn_{1-y})_2P_2S_6$ mixed crystals (Fig. 11) [86]. The tricritical points (TCP) were located near 220K for pressure p≈0.6 GPa [87] or for concentration y≈0.3 [65].

According to the dielectric data, in $(Pb_{0.2}Sn_{0.8})_2P_2S_6$ the second-order ferroelectric phase transition occurs at 248K [65]. At higher lead concentration, phase transition changes its character to the first-order. It was shown for the lead concentration y=0.3, the real and imaginary parts of dielectric susceptibility become broader and have a clear temperature hysteresis. This broadening in detail was explained considering different stereoactivity of tin and lead cations and involving of diluted BEG model: the sublattice of strongly stereoactive Sn^{2+} cations is diluted by weakly stereoactive Pb^{2+} cations. The resulting decrease of the stereoactivity of the two cation sublattices determines the decrease of the second order ferroelectric phase transition temperature down to the TCP [65].

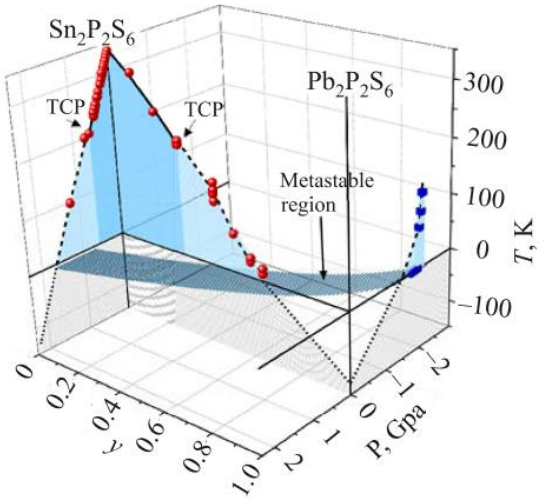

Fig. 11. Temperature-pressure (*T-p*) phase diagram of $Sn_2P_2S_6$ crystal and temperature-composition (*T-x*) phase diagram of $(Pb_ySn_{1-y})_2P_2S_6$ mixed crystals [86].

Besides, it was suggested the possibility of a ferroelectric phase transition at very low temperature in $Pb_2P_2S_6$ [64]. It was reported that the $Pb_2P_2S_6$ compound at normal pressure has quantum paraelectric ground state [86].

2.3.Low-frequency Noise and its Application in Materials Science

2.3.1.Intrinsic Noise Types and Fundamentals of 1/*f* Noise

Various manifestations of electronic noise are commonly classified into four intrinsic types: *thermal* or *Johnson noise*, *shot noise*, *generation–recombination (GR) noise* and *flicker* or 1/*f noise* [88] [89] [90].

The electrical noise has some mathematical characteristics that can provide insight about the magnitude and nature of the corresponding noise. Noise spectral density *S*(*f*) (also known as power spectral density) is the main characteristic of the electrical noise signal. In statistical signal processing, the power spectral density *S*(*f*) is defined as the Fourier transform of the Autocorrelation function. It is determined as the noise power per unit of bandwidth. It has dimension of power over frequency. For the sake of simplicity, the power spectral density is called spectral power.

For an ohmic sample the power spectral densities *S* are related to the fluctuating amplitudes about the mean value of the voltage, resistance,

current, conductance, carrier number etc. by the relations $S_R/R^2 = S_I/I^2 = S_V/V^2$. Similar expressions are found in nonohmic systems [88].

Nyquist noise (often known as *Johnson noise* or *thermal noise*) arises from the Nyquist theorem and in a resistor R at a temperature T, it shows up as white noise (which means that spectral power of noise is independent of f) of current spectral power S_I:

$$S_I(f) = 4k_B T/R \qquad (7)$$

where k_B is the Boltzmann's constant and T is temperature. In this case, the spectral power $S_I(f)$ is independent of the current through the resistor and is not dependent on the materials property of the resistor [91]. Thermal noise does not help to distinguish one material from another but it exists in almost all kinds of electronic systems. Consequently, it is not a useful tool, except in a few cases where this type of noise is used to measure the effective electron temperature or to calibrate a noise measuring setup [89].

The *shot noise*, which arises from discrete carrier motion in devices, is also white in nature. Not until the World War I did engineers begin to realize that the essential deterioration of vacuum-tube amplifier was not due to the thermal noise but the shot noise [92]. According to Schottky's theorem, the spectral power of shot noise is given by

$$S_I(f) = 2q\langle I\rangle \qquad (8)$$

where $\langle I\rangle$ is the average value of the electrical current, q – the elementary charge.

Shot noise is a good indicator of the magnitude of the charge carrier. In general, the shot noise is visible at low temperatures when the thermal noise is low enough. It is again a fundamental noise, namely it arise from the fundamental physical process and cannot be eliminated [92].

Generation-recombination (G-R) noise is a fluctuation in the conduction, and is observed at low frequencies [89]. Spectral density of generation-recombination noise is described by the Lorentzian power spectra of a single fluctuator (Fig. 11a):

$$S_I(f) = \frac{S_0}{1 + (2\pi f\tau)^2} \qquad (9)$$

where S_0 is the frequency independent portion of $S_I(f)$ observed at $f < (2\pi\tau)^{-1}$ and τ is the time constant associated with a specific trapping state. The name GR noise is often used for any noise with a Lorentzian spectrum [88].

Generation-recombination noise can be overwhelmed by another type of conductance fluctuation – *low-frequency* l/*f* (also called *flicker* or *pink*) *noise* [89]. 1/*f* noise was defined in terms of the noise power spectrum because it is inversely proportional to frequency at low frequencies [89]. For higher frequencies, the 1/*f* spectrum reaches the white noise floor. Depending on a particular device or temperature, the white noise level is defined by either thermal or shot noise. A change from a 1/*f* spectrum into an f^{-2} spectrum was also observed in some samples [92]. The specific physical mechanism for the l/*f* noise is not generally accepted. In many systems there is good evidence that it is related to defects or some trapping states and could be due to a superposition of many *G-R* spectra with different characteristic times [88]. Even though several mechanisms of 1/*f* noise has been proposed, no conclusive theory appears. It is possible that there is no common mechanism fro this type of noise but different mechanisms occur in different systems.

The most common description of 1/*f* noise, dominated by fluctuations in the number of free charge carriers *N*, stems from the observation that a superposition of individual GR noise sources with the lifetime distributed on a logarithmically wide timescale, within the τ_1 and τ_2 limits, gives the 1/*f* spectrum in the intermediate range of frequencies $1/\tau_2 < \omega < 1/\tau_1$ ($\omega = 2\pi f$ is an angular frequency) [93]. Introducing a density distribution of lifetimes, $g(\tau_N)$, one can write the spectral density of the number fluctuations, S_N, in the form

$$S_N(\omega) = \overline{4\delta N^2} \int_{\tau_1}^{\tau_2} g(\tau_N) \frac{\tau_N}{1 + (\omega\tau_N)^2} d\tau_N \qquad (10)$$

Integration of equation (10) for $g(\tau_N) = [\tau_N \ln(\tau_2/\tau_1)]^{-1}$ gives the 1/*f* spectrum inside the region determined by the limiting values of τ_N. Further development of this idea in the context of semiconductors led to a *McWhorter's number fluctuations model* [94] that is used to describe 1/*f* noise in MOSFET. In his model, McWhorter considered the carriers number fluctuation due to trapping of charge carriers in traps located at a semiconductor surface as the noise source. The 1/*f* spectrum comes from the superimposing noise spectra of $\tau/[1 + (\omega\tau)^2]$ over a wide range of τ whose distribution function is proportional to $1/\tau$ [94]. The contribution of traps with different τ results in a set of GR bulges represented by Lorentzian functions. The envelope of the closely positioned Lorentzians has the 1/*f*-type dependence over the relevant frequency range (Fig. 11b). If one type of traps dominates the fluctuation processes, for example, traps at the interface

with the same time constant, the GR bulge associated with this trapping state can appear superimposed on the 1/*f* spectrum [93].

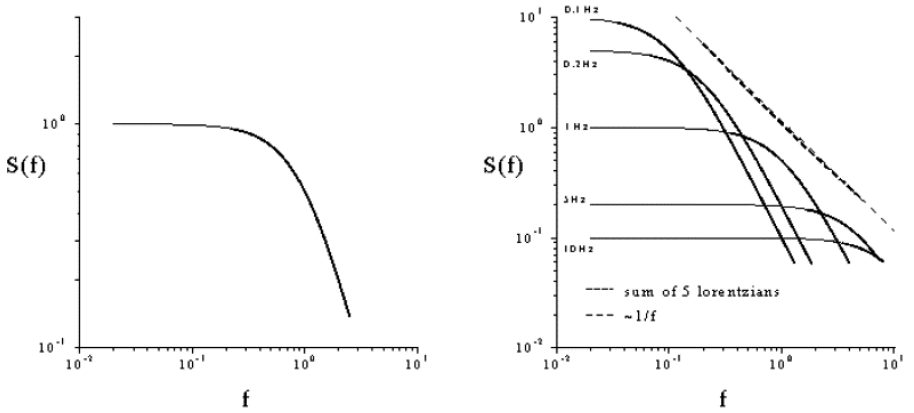

Fig. 11. (a) The Lorentzian power spectra of a single fluctuator (τ^{-1} = 1 Hz). (b) Generation of a power law *S* (*f*) from superposition of Lorentzians. In this case five Lorentzians have been used. τ^{-1} is marked in the graph [91].

In general, low-frequency 1/*f* noise can have another origin – the mobility fluctuations. It is not known which of the two models is correct for the l/*f* noise [88]. The low-frequency 1/*f* noise caused by mobility fluctuations can appear as a result of the superposition of elementary events in which the scattering cross-section, σ, of the scattering centres fluctuates from σ_1 to σ_2. The cross-section can change owing to capture or release of the charge carriers [93]. In this case, the noise spectral density of the elemental mobility-fluctuation events is given by

$$\frac{S_I}{I^2} \propto \frac{N_t^{\mu}}{V} \frac{\tau\varsigma(1-\varsigma)}{1+(\omega\tau)^2} \Lambda^2(\sigma_2-\sigma_1)^2 \qquad (11)$$

where N_t^{μ} is the concentration of the scattering centres of a given type that contribute to the noise, Λ is the mean free path of the charge carriers, ζ is the probability for a scattering centre to be in the state with σ_1. Integration of equation (11) results in the 1/*f* spectrum caused by the mobility fluctuations.

F. N. Hooge systematized the 1/*f* noise measurement results in metal films and developed phenomenologifcal theory of 1/*f* noise that is based on his empirical formula

$$\frac{S_R}{R^2} = \alpha_H / Nf \quad (12)$$

where S_R is the power spectral density of the resistance fluctuations, R is the resitance of the sample N is the total number of free carriers in the sample and α_H=2 10^{-3} is a dimensionless constant called Hooge's parameter. Later it has been found that α_H is not a constant, but that α_H depends on the prevailing type of scattering of the electrons and the perfection of the crystal lattice [89]. In high-quality material α_H can be more than 3 times lower than the originally proposed value.

2.3.2.Noise Spectroscopy in Materials Science

Noise spectroscopy in the field of materials science adds a new dimension to the experiment. Recently, noise spectroscopy has been coupled to other measurement techniques. Noise has long been used to investigate metal films, semiconductors, oxides, and composites [91] [88]. It is a unique and sensitive tool that can give information about statistics of defects and the relaxation phenomena that give rise to the noise [88], [89], [91]. The noise measurement in materials science is important not only from the scientific point of view but also there are many practical reasons why the characteristics of low-frequency noise are important: the sensitivity of electronic devices is highly defined by the low-frequency noise level [92].

Noise in semiconductors as well as in semiconductor devices have been investigated extensively. These investigations have been motivated from the viewpoint of understanding the noise in semiconductor devices so that they can be controlled. From the multitude of studies done on semiconductors some general statements has been made [91].

Systems with two dispersed phases (composites) are important materials because they offer the capability to engineer properties. Noise spectroscopy has long been used to study these materials. In these materials the volume fraction of one of the phases is varied relative to the other in order to change properties. Due to the inhomogeneous nature of the solids, the current paths in these materials are not uniform. This makes the conduction susceptible to fluctuation leading to noise. These aspects of composites have been studied intensively for a decade and a half [95].

The first report of $1/f$ noise in graphene appeared in 2008 [96]. Since that report, studies of the noise in graphene devices have been systematically performed [97]. It was suggested that the observed noise in graphene correlates better with charge scattering primarily due to the long-range

Coulomb scattering from charged impurities rather than short-range scattering from lattice defects [93]. The research of low-frequency noise in 2D transition-metal dichalcogenides is conducted as well [98]. Nevertheless, a considerably small number of papers have been dedicated to the investigation of noise in ferroelectrics [99][100][101][102] [103] [104].

This brief overview of noise spectroscopy in semiconductors, inhomogeneous systems, feroic and 2D materials is definitely not exhaustive analysis. A new positive trend to make noise measurements more useful and more informative is emerging due to the potential applications like reliability study and failure prediction.

3. EXPERIMENTAL

In this chapter the single crystal growth technique and experimental methods are presented.

3.1.Single crystal growth

All the studied phosphorous chalcogenide single crystals mainly were obtained by vapour transport (VT) or Bridgman (Br) techniques.

The following single crystals systems were prepared:

- $Sn_2P_2S_6$ VT and $Sn_2P_2S_6$ Br;
- $Pb_2P_2S_6$ VT;
- $(Pb_ySn_{1-y})_2P_2S_6$ (y=0.1, 0.2 an 0.3) VT;
- $(Pb_{0.98}Ge_{0.02})_2P_2S_6$ VT;
- $(Pb_{0.7}Sn_{0.3})_2P_2S(Se)_6$ VT;
- $CuInP_2S_6$ VT;
- $AgCrP_2S_6$ and $Cu_{0.2}Ag_{0.8}P_2S_6$ VT.

The studied single crystals were prepared in collaboration with scientists from the Institute of Solid State Physics and Chemistry, Uzhgorod University, Ukraine.

3.1.1.Vapour transport method

The single crystals of $(Pb_ySn_{1-y})_2P_2S_6$ (y = 0.1, 0.2 and 0.3) were grown by the vapour transport technique in an evacuated quartz tube using I_2 as a transport agent. The synthesis of the starting material in the polycrystalline form was carried out using high-purity elements Sn (99.99%), P (99.999%), S (99.99%), Pb (99.99%), in atomic percentage. Required amount of tin, phosphorous, sulphur and lead was placed into quartz tube for further homogenization at 650°C during one week. After, the recrystallization by vapor transport between hot zone at 650°C and cool zone at 630°C has taken three days. At the next stage, the cool zone was cleaned by heating and further this zone has been cooled to 615°C and kept at this temperature until the appearance of visually observed crystal nucleus. From this moment the monocrystal growth was started with duration of near one month. At the finish of the growth process, the hot zone of a quartz tube was absolutely

clean, which gave evidence that a full mass transport and a growth of a monocrystal with needed stoichiometry was achieved.

3.2.Experimental methods

Dielectric measurements. In the wide temperature and low frequency (from 20 Hz to 1 MHz) range, capacitance and loss tangent of the sample was measured with Hewlett Packard 4284 precision LCR meter. For all measurements the silver paste electrodes were painted on the largest (001) face to ensure electrical contact. This surface is nearly a normal to the spontaneous polarization. Complex dielectric permittivity was calculated from the plane capacitor formulas:

$$\varepsilon' = \frac{(C_S - C_0)h}{\varepsilon_0 A} + 1, \qquad (13)$$

$$\varepsilon'' = \varepsilon' tg\delta = \frac{C_S tg\delta_S - C_0 tg\delta_0}{C_S - C_0} \qquad (14)$$

where C_S and $tg\delta_S$ are capacitance and loss tangent of the system with the sample, C_0 and $tg\delta_0$ are capacitance and loss tangent of the system without the sample, h is height of the sample, A is the area of the sample, ε_0 is the dielectric permittivity of vacuum.

The area of the sample was much larger as quadrate of height h^2 so that the fringing field effects were insignificant in all performed experiments. Measurements were performed during continuous temperature variation on a cooling cycle with cooling rate 0.05 K/min near a phase transition temperature and 0.5 K/min far from a phase transition temperature. All measurements were performed on cooling and heating but most of presented results are on cooling. The samples were cooled using the liquid nitrogen.

Ferroelectric and pyroelectric measurements. Ferroelectric and pyroelectric properties were measured by a commercial ferroelectric test system (TF Analyzer 2000E with FE-Module, AixACCT, Germany) with TREK 609E high voltage set-up. The external high voltage amplifier allows voltage pulses ranging from 200 V to 4 kV to be applied to the sample via the probes. Measurements were performed in the temperature range from 180 to 350 K. The TF-Analyzer 2000 system is actually modular; attaching an FE-module will allow hysteresis loops to be measured. The FE-module can be replaced by three other modules to investigate different ferroelectrics behaviors.

Polarization hysteresis, which allows a fast characterization of the ferroelectric samples, was considered a standard technique. Ferroelectric hysteresis loops have been obtained using the Dynamic Hysteresis Mode (DHM). In the DHM method, four bipolar triangular excitation signals of frequency v_0 are applied with a delay time τ between them as shown in Fig. 12. The first (third) bipolar voltage (V) pulse prepolarizes the sample in the negative (positive) state. The frequency of the triangular signal was varied in the range of 3-30 Hz in accordance to the sample parameters. The $I_{DHM}(V)$ loop is obtained from the addition of the currents measured while applying the negative V during the second pulse and the positive V during the fourth pulse as indicated in Fig. 12 (shaded areas). The final hysteresis is then calculated from the measured current response $I_{DHM}(V)$

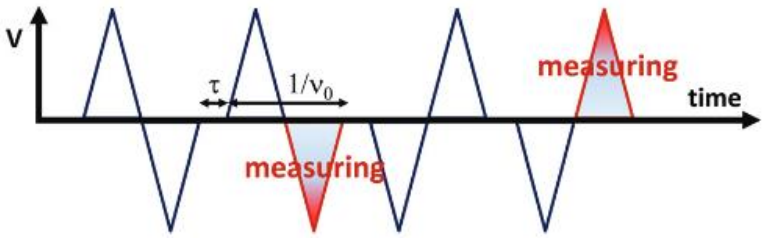

Fig. 12. Voltage sweeps for FE characterization.

The polarization was calculated from the pyrocurrent response on the heating cycle after the sample was poled. It was recorded the current flow through the sample when the temperature is changed at 5 K/min rate. The pyroelectric coefficient γ was calculated according to the following formula:

$$\gamma = \frac{I}{A}\frac{1}{\mathrm{d}T/\mathrm{d}t} \qquad (15)$$

where I is the pyroelectric current, A is the electrode surface area, dT/dt is the rate of temperature change.

Noise measurements. For the noise measurements plate-like $CuInP_2S6$ crystals grown by vapour transport technique were used. The measurements were performed in direction perpendicular to the layers. In order to obtain a good electrical contact silver paste was painted on the top and bottom surfaces of the crystals.

Low-frequency (from 10 Hz to 20 kHz) noise characteristics (voltage fluctuation spectral density) were measured under continuous wave

operation in the temperature range from 290K to 350 K. The voltage noise measurements were performed at a constant voltage of 5V. The noise measurement circuit comprises of a low-noise amplifier, a filter system, and an analog-digital converter (National Instrument TM PCI 6115 board; Fig. 13). As the resistance of $CuInP_2S_6$ is relatively high, the noise measurements were performed at constant voltage using a load resistance about 20-40 times smaller than that of the sample. Typically, the load resistance is selected to be 30-50 times higher than the resistance of the sample in order to operate in a constant current mode.

Noise measurements were performed in a specially copper and iron shielded room (Faraday cage) in order to avoid interfering effects from the electrical network and communication systems.

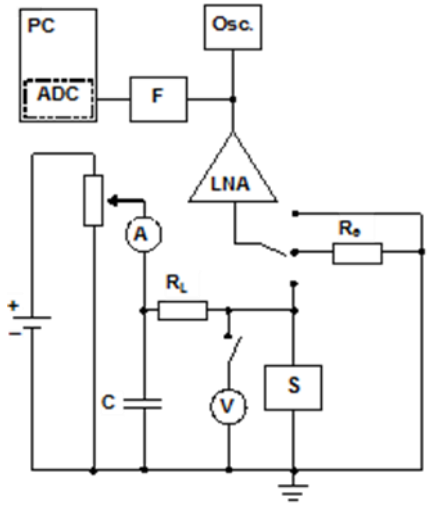

Fig. 13. Experimental circuit of low-frequency noise measurements: S – investigated sample, RL - load resistor, R_e – standard resistor, LNA – low-noise amplifier, F – filter system, ADC – analogue-to-digital converter, PC – personal computer, Osc. – oscilloscope.

The noise signal was processed with a computer-based fast Fourier transform signal analyzer. The data series of 4096 points were sampled at 44.1 kHz. For better measurement accuracy, 200 time series were averaged, which corresponds to 18.6 s series.

The voltage spectrum density, S_V, was calculated using the Cooley–Tukey fast Fourier transform algorithm and evaluated by comparing with the thermal noise of a standard resistor:

$$S_V = \frac{\overline{V^2} - \overline{V_{syst}^2}}{\overline{V_{et}^2} - \overline{V_{syst}^2}} \cdot 4kT_0R_{et} \qquad (16)$$

where $\overline{V^2}$, $\overline{V_{\text{syst}}^2}$, $\overline{V_{\text{et}}^2}$ are the sample, the measuring system, and the standard resistor thermal noise variances in the narrow frequency band Δf; T_0 is the absolute temperature of the standard resistor.

4. RESULTS AND DISCUSSION

4.1.Dielectric and ferroelectric properties of $Sn_2P_2S_6$ single crystals

This section presents the results of the double polarization hysteresis loops in the tin thio-hypodiphosphate $Sn_2P_2S_6$ ferroelectric crystal (SPS). The $Sn_2P_2S_6$ crystals are obtained by two methods: the vapor-transport ($Sn_2P_2S_6$ VT) and Bridgman ($Sn_2P_2S_6$ Br) techniques. Crystals grown by both methods were used in this study to ensure the reliability and the repeatability of the results.

The temperature dependences of the real and imaginary parts of the dielectric permittivity of $Sn_2P_2S_6$ Br sample are presented in Fig. 14. As can be seen in Fig. 14, the second-order phase transition is manifested by a sharp peak in the temperature dependencies of the dielectric permittivity near T_0 (for both the real and the imaginary parts). The dielectric losses in the polar phase have a sufficiently high value but they decrease rapidly below 260 K.

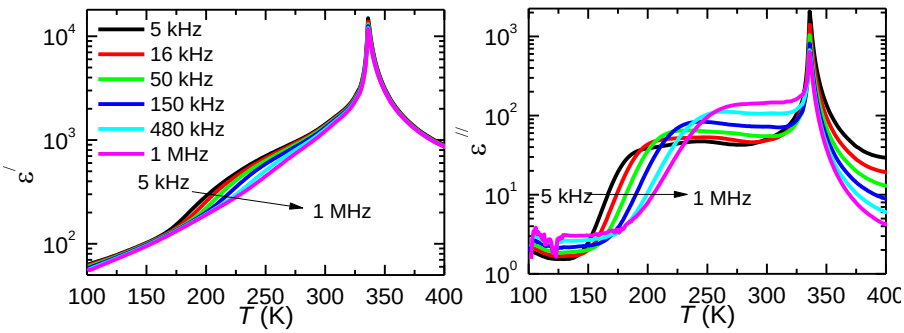

Fig. 14. Temperature dependences of the real and imaginary parts of the dielectric permittivity of the Bridgman-grown $Sn_2P_2S_6$ crystal at different frequencies.

Dielectric spectrosopy also was performed for the vapor transport-grown $Sn_2P_2S_6$ samples. However, dielectric losses of SPS VT was smaller in comparison to $Sn_2P_2S_6$ Br samples. Figs. 15-16 represent temperature evolution of polarization hysteresis loops of $Sn_2P_2S_6$ Br and $Sn_2P_2S_6$ VT single crystals, respectively.

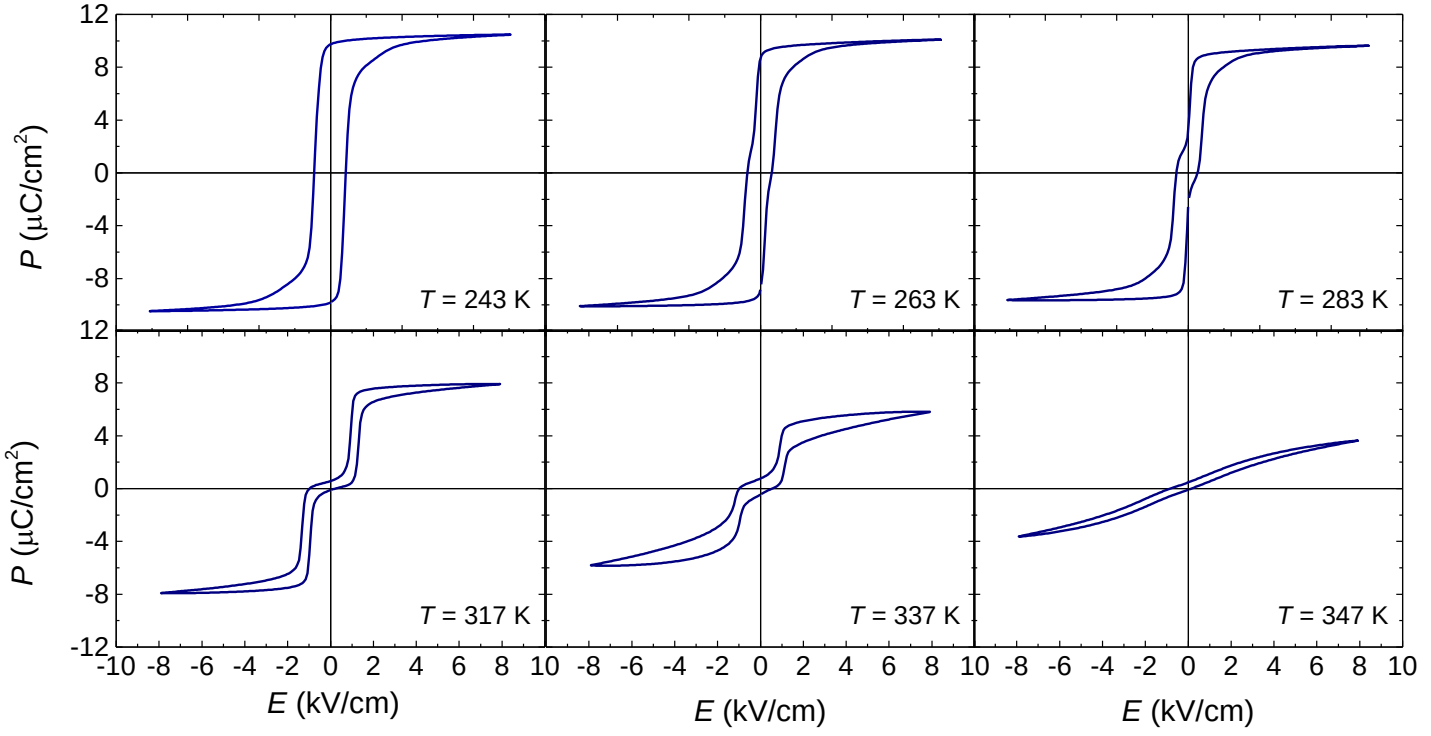

Fig. 15. Temperature evolution of polarization hysteresis loops in the Bridgman-grown $Sn_2P_2S_6$ crystal.

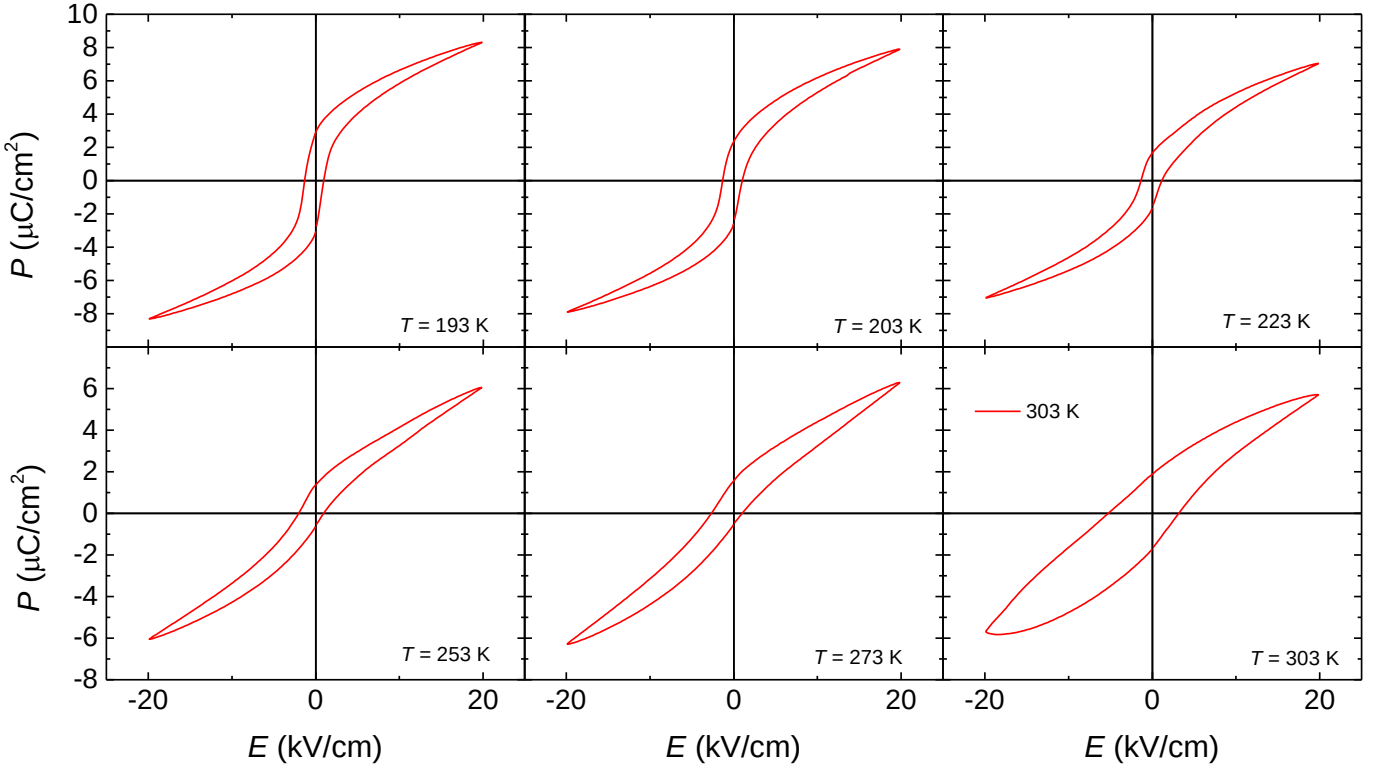

Fig. 16. Temperature evolution of polarization hysteresis loops in the vapor transport-grown $Sn_2P_2S_6$ crystal.

For the Bridgman-grown $Sn_2P_2S_6$ sample below T_0, the hysteresis loops have a double kind of shape (Fig.15). At zero field, the spontaneous polarization is very small (< 1 μC cm^{-2}) but it reaches 8 μC cm^{-2} upon an increase of the electric-field amplitude to 6 kV/cm for T= 318 K. As it is evident, the double hysteresis loops are connected by two lines crossing the origin point for the *P-E* graph. Such a peculiarity is related to the electrical conductivity of the investigated samples. For the same reason, the shape of the loops in the paraelectric phase, above 338 K, is found to be deformed ellipse-like (Fig.15). Upon cooling below 283 K, the hysteresis loops take up the usual ferroelectric shape with a spontaneous-polarization value near 10 μC cm^{-2} and a coercive field of about 1 kV/cm.

In previous studies [105], SPS crystals were characterized by an ordinary ferroelectric hysteresis loop, with a spontaneous polarization value of 14 μC cm^{-2} and a coercive field of 0.75 kV cm^{-1}. SPS crystal posseses the polarization in the (010) plane deviating at (14 ± 2)º from the *x* polar axis. It is worth to mention, that the aforementioned authors studied the SPS crystal grown by vapour transport technique. Meanwhile, in Fig. 15 is shown the hysteresis of the Bridgman-grown $Sn_2P_2S_6$ crystal. Therefore, the investigation of polarization hysteresis of $Sn_2P_2S_6$ VT crystal is necessary. $Sn_2P_2S_6$ VT samples exhibit ferroelectric loops (Fig. 16). The hysteresis loops shown in Fig. 16 are in good agrreement with those reported in [105]. The shape of the hysteresis shown in Fig. 16 indicates the enhanced conductivity in $Sn_2P_2S_6$ VT probably due to the increased concentration of defects.

After the $Sn_2P_2S_6$ sample has been kept in the paraelectric phase at a temperature of about 373 K for 2 h and with further cooling to 190 K, ordinary ferroelectric loops are observed (Fig. 17). At the same time, the spontaneous polarization and coercive field reach values of about 11 μC cm^{-2} and 2 kV/cm, respectively. However, after the sample has been kept at room temperature for a few weeks, antiferroelectric-like double loops are again observed. It should be noted that this phenomenon is repetitive for different samples. Obviously, the balance between the ferroelectric and antiferroelectric states is determined by the long-time relaxation processes in the electron subsystem of the $Sn_2P_2S_6$ ferroelectric semiconductor. These findings should be subjected to further investigation.

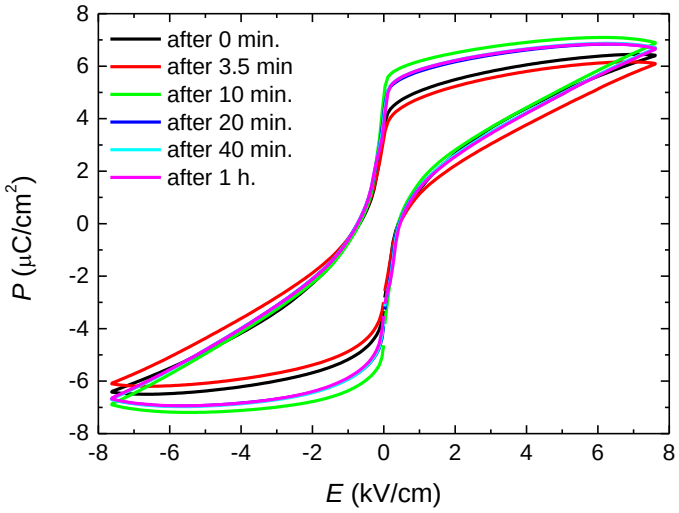

Fig. 17. *P-E* loops time dependence at fixed temperature just below phase transition (around 336,5 K) after annealing for 2 hours at 373K.

In $(Pb_ySn_{1-y})_2P_2S_6$ and $Sn_2P_2(Se_xS_{1-x})_6$ mixed crystals, the usual hysteresis loops also are observed. In the elementary cell of $Sn_2P_2S_6$ crystals, all atoms are placed in general positions with C_1 point-group symmetry [64]. It follows that the atomic substitution increases the crystal lattice defects and avoids the possibility of the observation of double loops.

The *P-E* hysteresis is investigated at different switching parameters (the frequency and amplitude of the electric field). In all measurements, the double hysteresis loops demonstrate their antiferroelectriclike shape over the whole range of variation of parameters (Figs. 18(a-b)). For example, the switching-current hysteresis is shown in Fig. 18(c) at different frequencies of the applied electric field. As expected, it has four peaks related to double hysteresis loops.

It was supposed that the observed peculiar switching in $Sn_2P_2S_6$ ferroelectrics is determined by the local three-well potential for the spontaneous polarization fluctuations at a specified negative ratio of intersite interactions in a given sublattice and between two sublattices of the $Sn_2P_2S_6$ crystal structure [64], [72], [75]. The QAO model presented below describes the possibility of the realization of double (antiferroelectric-like) hysteresis loops in such proper uniaxial ferroelectrics.

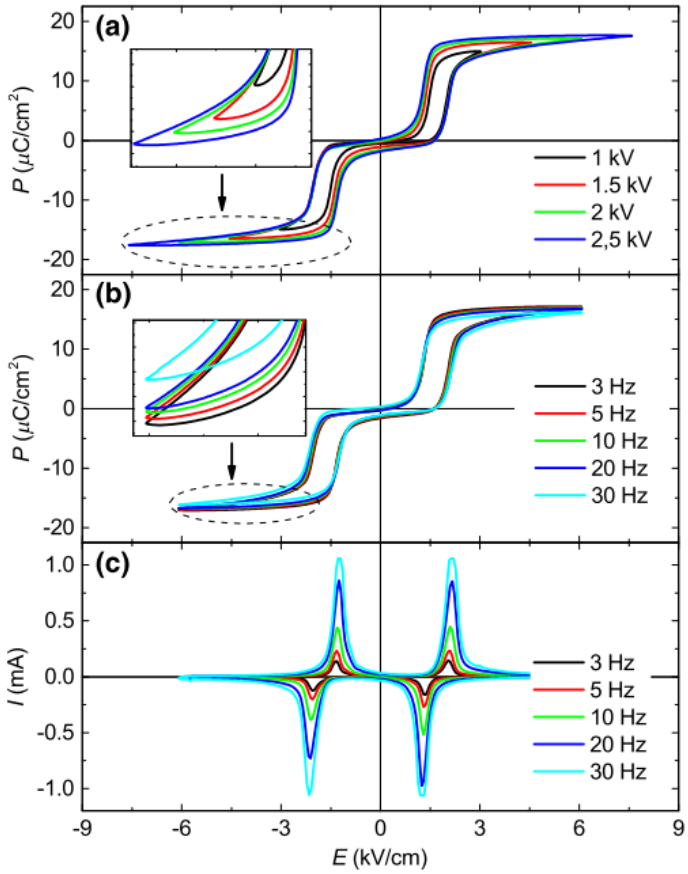

Fig. 18. *P-E* hysteresis loops measured in a $Sn_2P_2S_6$ Br sample at room temperature with various switching parameters: (a) different voltage amplitudes at a frequency of 3 Hz; (b) different frequencies with a voltage amplitude of 2 kV. (c) The switching current - field dependencies that are related to the hysteresis loops at a voltage amplitude of 2 kV at different frequencies.

In this work, it is developed an enhanced QAO model that has previously been described for the investigated crystal [86]. In the AQO model, crystal was represented as one dimensional system of anharmonic oscillators which interact via quadratic interaction term. Hamiltonian of such a system is

$$H = \sum_i \left(T(p_i) + V(x_i)\right) - \sum_{ij} J_{ij} x_i x_j \qquad (17)$$

where the $T(p_i)$ and $V(x_i)$ are the operators of the kinetic and potential energy and J is the coupling and potential energy. Here, the last term in the

Hamiltonian given in Eq. (17) reflects the mean-field approach by taking the relation $\sum_{ij} J_{ij} x_i x_j \to \sum_i J x_i \langle x \rangle$ into account. This proposal makes it possible to represent a model Hamiltonian as a sum of one-particle non-interacting Hamiltonians:

$$H = \sum_i H_i^{eff}, \quad H_i^{eff} = T(p_i) + V(x_i) - J x_i \langle x \rangle \qquad (18)$$

The main difference consists in the model representation of a crystal lattice. The real crystal lattice has been described earlier as a one-dimensional chain of equivalent quantum anharmonic oscillators. The interaction of the oscillators is described within the mean-field approach, which makes it possible to consider such a system as one comprised of noninteracting oscillators. Suppose, $Sn_2P_2S_6$ crystal lattice is described as two interacting subsystem of oscillators. The elementary cell of $Sn_2P_2S_6$ contains two formula units, which are related by the symmetry plane (see Fig. 5). Despite the three-dimensional structure of the $Sn_2P_2S_6$ crystal, its lattice can be presented as two chains of equivalent sites with a local three-well potential. The shape of the local three-well potential has been determined earlier by first-principles calculations [72]. This shape can be changed by pressure or with variation of the chemical composition in mixed crystals [86]. For simplicity, the chains are completely identical and are characterized by the same local potential V for each site and coupling constant J_1. However, the interaction between oscillators from different subsystems is characterized by another coupling constant, J_2. The mean-field approach is also applied. Therefore, the total Hamiltonian H_t for such a system can be written as a sum of two Hamiltonians H_1 and H_2 for each *x* and *y* subsystem:

$$H_t = H_1 + H_2 \qquad (19)$$

$$H_1 = \sum_i (T(x_i) + V(x_i) + (J_1 \langle x \rangle + J_2 \langle y \rangle) x_i \qquad (20)$$

$$H_2 = \sum_i (T(y_i) + V(y_i) + (J_2 \langle x \rangle + J_1 \langle y \rangle) y_i \qquad (21)$$

To investigate the influence of an external electric field *E* on the model system, the terms proportional to Ex_i and Ey_i should be added to Eqs. (20) and (21), respectively.

Self-consistently solving the system of Eqs. (20-21), it can be obtained the energy levels and corresponding wave functions of the system. Solution

of this Hamiltonian is a set of eigen energies $\{E_n\}$ of levels and its wave functions $\{\Psi_n(x)\}$ and $\{\Psi_n(y)\}$ which are used for self consistent calculation of average expectation values. It should be noted that temperature enters in effective Hamiltonian (19) indirectly through Boltzmann distribution for the occupation of the levels. The average displacements of the subsystems $\langle x\rangle = \sum_n p_n x_n$ and $\langle y\rangle = \sum_n p_n y_n$ are determined at each temperature, where $p_n \sim \exp(-\frac{E_n}{kT})$ is the probability to find the oscillator at the *n*th level with the energy E_n, x_n and y_n is the average displacements for the *n*th level. Then, the order parameter, which is proportional to the sum of the average displacements of the oscillators can be calculated for different temperatures.

It should be noted that the shape of the local three-well potential V is phenomenologically described by the non-linear interaction $A_g B^2_u$ of several low-energy optic modes of B_u symmetry with fully symmetrical A_g modes [72]. The shifts of the Sn^{2+} cations relative to the anions (Fig. 5) are accompanied by recharging and change in the covalency of the chemical bonds determining the origin of the local electric dipoles in every $Sn_2P_2S_6$ formula unit. At the given site, the fluctuations of the pseudospin in such a local three-well potential can be related to the Hubbard-Holshtein model for systems with electronic correlations involving phononic excitation [106]. Such a description can be projected on to the Blume-Emery-Griffiths (BEG) model with three values of pseudospins ("−1," "0," and "+1") and with two order parameters-dipolar with B_u symmetry and quadrupolar with A_g symmetry.

Upon evaluation of the QAO model parameters, the local three-well potential, which is determined by first-principles calculations [72], is taken into account. It is worth to mention that the parameters of the model were determined from independent measurements. The "inter-chain" coupling constant J_1 is chosen to fit the second-order phase transition temperature $T_0 \approx 337$ K at normal pressure. Also taken into account is the fact that for $Sn_2P_2S_6$ crystal, the ratio of interactions $J_2/J_1 \approx -0.23$ [64], which follows from analysis of the $T-x$ diagram of $Sn_2P_2(Se_xS_{1-x})_6$ mixed crystals in the axial next-nearest-neighbor Ising (ANNNI) model [107], explains the observed Lifshitz point at $x_{LP} \approx 0.28$ and continuous transitions from the paraelectric phase into the incommensurate phase at $x > x_{LP}$.

Let us introduce dimensionless parameters such as the reduced temperature ($\tau = T/T_0$ where T_0=337 K is the Curie temperature of $Sn_2P_2S_6$) and the ratio of the coupling constants $\lambda = J_2/J_1$ QAO model τ-λ phase diagram is shown in Fig. 19. It contains paraelectric (PE), ferroelectric (FE), and antiferroelectrcis (AFE) phases, and four regions I-IV with metastable

states. There are two points, λ = 1and λ =−1, phases, where no metastable regions occur, and pure FE and AFE phases, respectively, can be observed. Also, in the case of λ = 0 (no interaction between different chains), FE or AFE phases can be realized with equal probability.

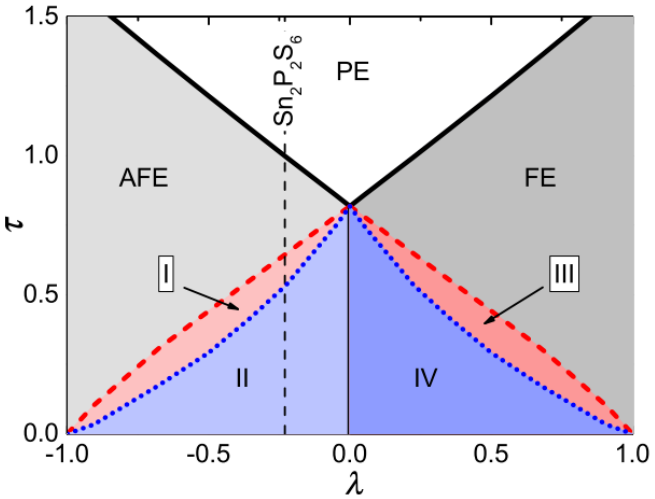

Fig. 19. The reduced temperature τ – coupling constant ratios λ phase diagram for the AQO model with stable paraelectric (PE), ferroelectric (FE), and antiferroelectric (AFE) phases. The coexistence of metastable AFE and FE states can be reached upon lowering of the temperature: region I contains, in addition to the stable AFE phase, one state with FE ordering, while region II contains two FE states; region III contains, in addition to the stable FE phase, one state with AFE ordering, while region IV contains two AFE states. The thermodynamic path for the $Sn_2P_2S_6$ crystal is highlighted by the vertical dashed line.

The λ= -0.23 point on the phase diagram can be associated with the model parameters for the $Sn_2P_2S_6$ crystal. For such parameters, the AFE phase appears at cooling below T_0. But inside the AFE phase, metastable FE states are also predicted (Fig. 19). For this case, the temperature dependencies of the total reduced polarization ρ (where $\rho = P/P_0$ and P_0 is a polarization in one subsystem at zero temperature for a stable solution) for all solutions are presented in Fig. 20. The contributions from different chains to the total polarization are shown in the insets. As is evident, the phase transition from the PE phase to the AFE phase at τ = 1 is a continuous transition, and additional metastable states with FE ordering of oscillator displacements appear continuously at $\tau = \tau_1$ and discontinuously at $\tau = \tau_2$.

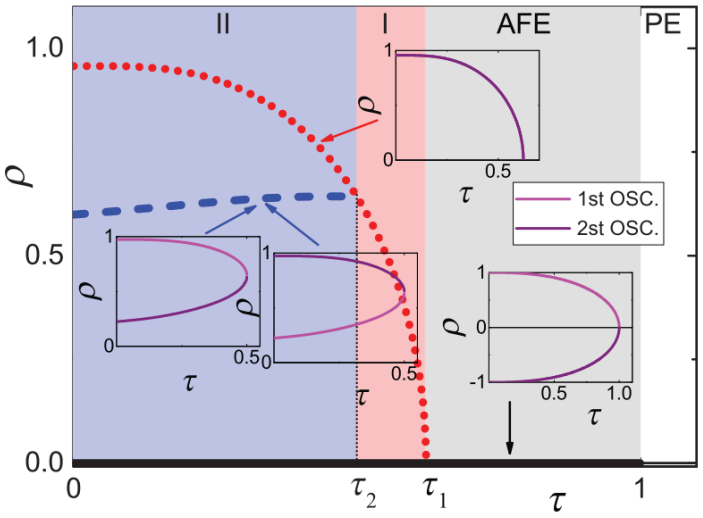

Fig. 20. The temperature dependence of the total reduced order parameters ρ for all solutions in the case of λ= -0.23. The thick black line corresponds to the order parameter of the AFE phase, which appears continuously at $\tau \leq 1$; the red dotted line corresponds to the continuous appearance of the FE phase at $\tau \leq \tau_1 \approx 0.62$; and the blue dashed line corresponds to the discontinuous appearance of the FE phase at $\tau \leq \tau_2 \approx 0.5$. The magenta and purple lines in the insets correspond to contributions to the total polarization from the first and the second subsystem, respectively.

The calculated dependence of the reduced polarization ρ versus the reduced electric field ξ dependence (where $\xi = E/E_0$ and E_0 is a coercive field at zero temperature) for different temperatures demonstrates several branches of stable and metastable solutions (Fig. 21). At zero temperature on a hysteresis loop, for example, there are three stable solutions, for which the polarization increases with an increase in the applied field, and three metastable solutions, for which the polarization decreases with an increase in the applied field. These solutions demonstrate the possibility of the observation of double hysteresis loops for proper uniaxial ferroelectrics $Sn_2P_2S_6$ with a three-well local potential for spontaneous polarization fluctuations and at a negative ratio of interactions inside and between the structure sublattices.

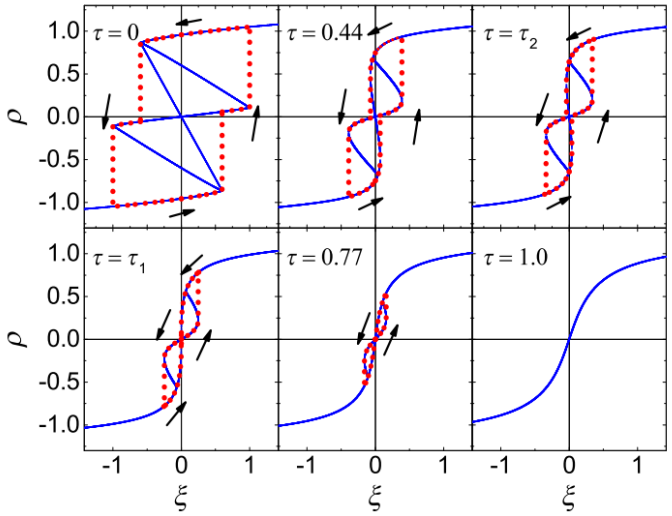

Fig. 21. The calculated dependencies of the polarization from the external electric field at different temperatures for the case temperature are shown by the red dotted lines. of $\lambda = -0.23$ (blue lines). Possible hysteresis loops for each temperature are shown by the red dotted lines.

Finally, we turn to the interesting question of why annealing in the paraelectric phase destroys the conditions for the observation of double loops upon cooling below T_0. As we mentioned earlier, for a $Sn_2P_2S_6$ ferroelectric semiconductor, spontaneous polarization is related to the stereoactivity of the tin cations and the valence fluctuations of the phosphorus cations. Recharging occurs and the changes in the covalence of the chemical bonds can be presented as small-hole polar formation in a given $SnPS_3$ structural group and the appearance of small electron polarons in the nearest $SnPS_3$ structural group [10]. The local dipole in the $Sn_2P_2S_6$ formula unit can be originated by a polaronic exciton, and the ferroelectric phase can be characterized as a coherent state of polaronic excitons. At heating above T_0, free carriers are thermally excited. They can be trapped at the lattice imperfections, producing dipole defects in the paraelectric phase and, obviously, these prevent the observation of double dielectric loops below T_0.

Summary. In bulk proper uniaxial ferroelectrics, double antiferroelectric-like hysteresis loops are observed in the case of $Sn_2P_2S_6$ crystal. The quantum anharmonic oscillator model is proposed for the description of such a polarization switching process. This phenomenon is related to the three-well local potential of the spontaneous polarization fluctuations at a distinctive negative ratio of coupling constants that correspond to intersite

interaction in the given sublattice and interaction between two sublattices of the modeled $Sn_2P_2S_6$ crystal structure.

4.2.Phase transitions in $(Pb_ySn_{1-y})_2P_2S_6$ solid solutions

Dielectric characterization. The dielectric permittivity data was used to determine the phase transition temperature variation with increasing lead content in $(Pb_ySn_{1-y})_2P_2S_6$ system. Fig. 22 shows the temperature dependences of real and imaginary parts of dielectric permittivity of $(Pb_ySn_{1-y})_2P_2S_6$ (y = 0.1, 0.2 and 0.3) single crystals.

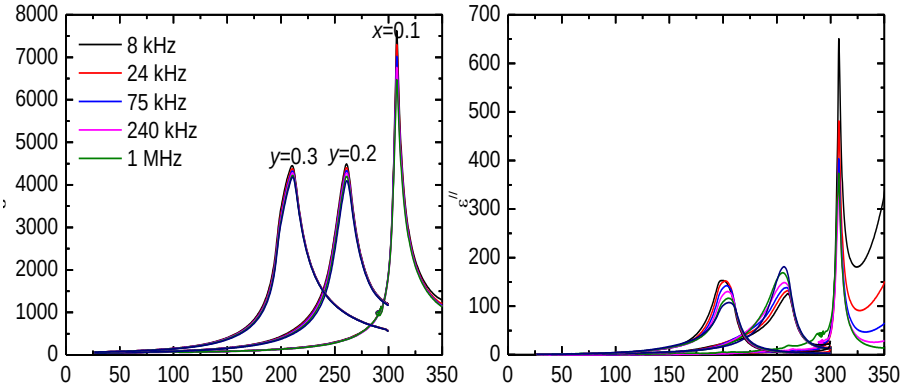

Fig. 22. Temperature dependence of dielectric permittivity of $(Pb_ySn_{1-y})_2P_2S_6$ single crystals (y=0.1, 0.2 and 0.3).

The structural phase transition was observed in all studied compositions. Phase transition temperatures obtained by dielectric spectroscopy together with phase transition temperatures previously obtained by dielectric and ultrasonic techniques are shown in Fig. 23. Ferroelectric phase transition in $Pb_{0.4}Sn_{1.6}P_2S_6$ and $Pb_{0.6}Sn_{1.4}P_2S_6$ single crystals changes its character: the anomalies of both the real and imaginary parts of dielectric permittivity become broad.

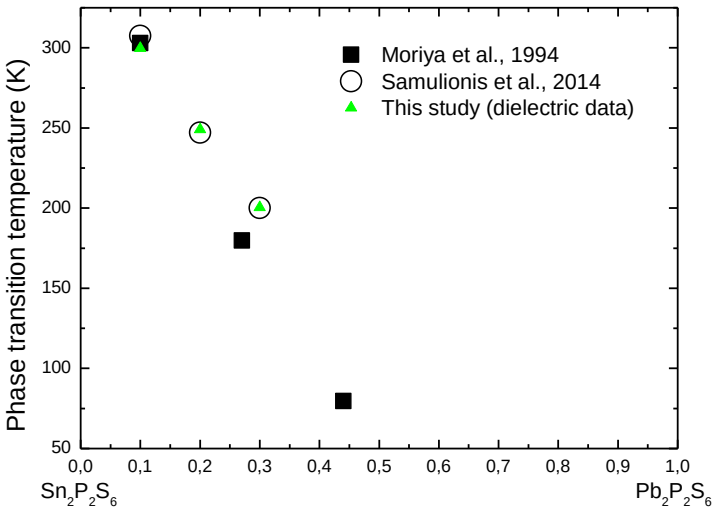

Fig. 23. The phase transition temperature dependence on the Pb^{2+} ion mole fraction in $(Pb_ySn_{1-y})_2P_2S_6$ single crystals. The positions of the dielectric and ultrasonic anomalies are shown according to the data of Refs. [83] and [108]. Solid symbols indicate the data obtained in this study.

To understand the nature of the phase transition, the reciprocal dielectric constant ($1/\varepsilon$‘) versus temperature for $(Pb_ySn_{1-y})_2P_2S_6$ single crystals (y = 0.1, 0.2 and 0.3) at 100 kHz is shown in Fig. 24. Data at this frequency corresponds to static permittivity, because no dispersion was observed. The reciprocal dielectric constant obeys Curie-Weiss law in $Pb_{0.2}Sn_{1.8}P_2S_6$ single crystals. The ratio of slopes in the ferroelectric and paraelectric phases is equal to 2.2 and Curie temperature is T_C=299.7 K. Such Curie-Weiss constant ratio suggests continous second-order ferroelectric-paraelectric phase transition which coincide well with the previous studies [83]. In Ref. [83] Curie-Weiss plot of the sample x=0.1 shows a straigth line, and no dielectric dispersion was observed around ferroelectric-paraelectric phase transition. The magnitude of the Curie constant in $(Pb_ySn_{1-y})_2P_2S_6$ single crystals (y=0.1) above phase transition is of the order of 10^5 which is more consistent with the displacive type ferroelectrics and is in good accordance with the value provided in Ref. [83].

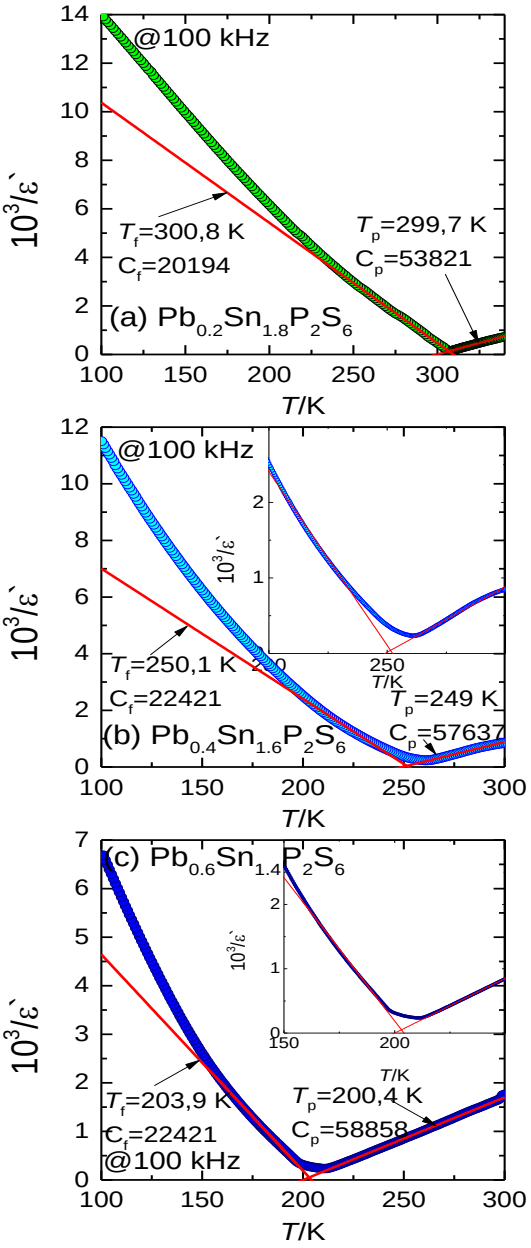

Fig. 24. Temperature dependences of the inverse dielectric permittivity. Red solid line represents the fit by the Curie-Weiss law, insets represent some intermediate phase. The experimental points are taken at 100 kHz frequency.

As it was mentioned before, at higher lead concentration the phase transition becomes broader. This is clearly seen in the insets of the temperature dependences of the inverse dielectric permittivity (Fig. 24 (b-c)). The Curie–Weiss fitting of the dielectric permittivity in these crystals are only valid above and below the maximum dielectric constant. It was shown earlier, that within $p=p_{atm}$ to p=0.27 MPa for y=0.1 and y=0.2 the ratio of Curie Weiss constants in paraelectric and ferroelectric phases is equal to 2 [109]. This ratio for y=0.1 is in good agreement with ours. However, the observed deviation from Curie-Weiss law in the intermediate region (Fig. 24(b-c)) does not allow to make a conclusion about a continous paraelectric-ferroelectric phase transition in $(Pb_ySn_{1-y})_2P_2S_6$ (y=0.2, 0.3) mixed crystals. Recently, a crossover has been reported in $(Pb_ySn_{1-y})_2P_2S_6$ from a non-mean field model at y = 0.1 to a mean-field one at y = 0.3 [110]. These findings coincide well with the presented in this study.It was also demonstrated by Moriya et al. [83] that the phase transition broadens slightly for x=0.27 and 0.53 because of compositional fluctuations and Curie-Weiss law is invalid for the solid solutions with concentration x>0.27

Pyroelectric Characterization. The temperature dependence of the pyroelectric coefficients is shown in Fig. 25. The variation of pyroelectric coefficient with temperature shows maxima in the phase transition region for all the investigated solid solutions. These maxima are related to the rapid disappearance of polarization at the phase transition of the crystal. The increase in lead content does not affect the maximum value of pyroelectric coefficient, and the maximum values of pyroelectric coefficients γ_{max} (in the vicinity of the phase transition temperature) are nearly equal to 250 nC cm^{-2} K^{-1} for all the compositions. Meanwhile, it was found earlier that in pure $Sn_2P_2S_6$ crystal the maximum value of pyroelectric coefficient possesses 650 nC cm^{-2} K^{-1} close to the phase transition point [64]. Moreover, after crossing the Curie temperature the pyroelectric coefficient of pure $Sn_2P_2S_6$ is rapidly dropping down to the zero [75], but in our investigated $Pb_{0.4}Sn_{1.6}P_2S_6$ and $Pb_{0.6}Sn_{1.4}P_2S_6$ compositions behaviour was slightly different: it only gradually diminishes. The lead-doped crystal has much more crystal lattice defects. At a substitution of tin by lead, local dipoles appear, which can be considered as random fields.

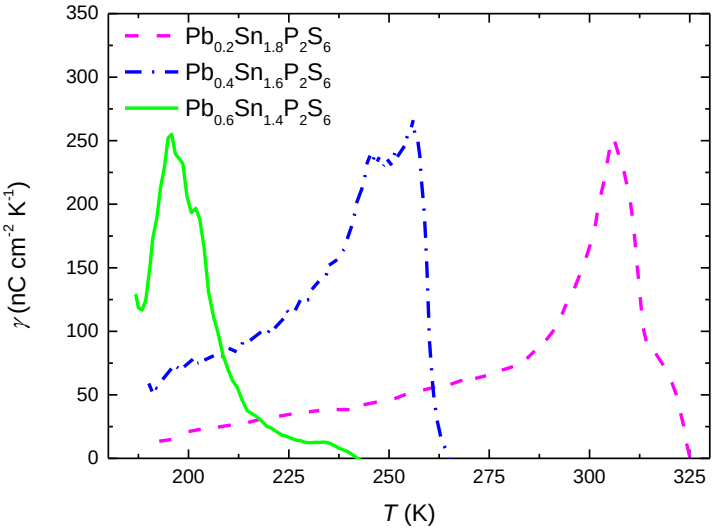

Fig. 25. Temperature dependences of the pyroelectric coefficients of $(Pb_ySn_{1-y})_2P_2S_6$ single crystals (y=0.1, 0.2 and 0.3).

Temperature dependences of the spontaneous polarization of $(Pb_ySn_{1-y})_2P_2S_6$ single crystals (y = 0.1, 0.2 and 0.3) is shown in Fig. 26. The Curie temperature T_C value obtained by these pyroelectric measurements for $Pb_{0.2}Sn_{1.8}P_2S_6$ is equal to 308.5±0.06 K. The phase transition temperature obtained from pyroelectric measurements differs from the dielectric measurements because the sample was multidomain when performing dielectric spectroscopy. The pyroelectric measurements were carried out on polarized samples and this gives the true value of the spontaneous polarization. Therefore, Curie temperatures obtained by pyroelectric measurements should be more reliable and in better agreement with Landau theory. This theory predicts that the order parameter varies as a function of $(T_C\text{-}T)^{1/2}$ in the ferroelectric phase ($T<T_C$) in accordance with the thermodynamic theory of second order phase transition.

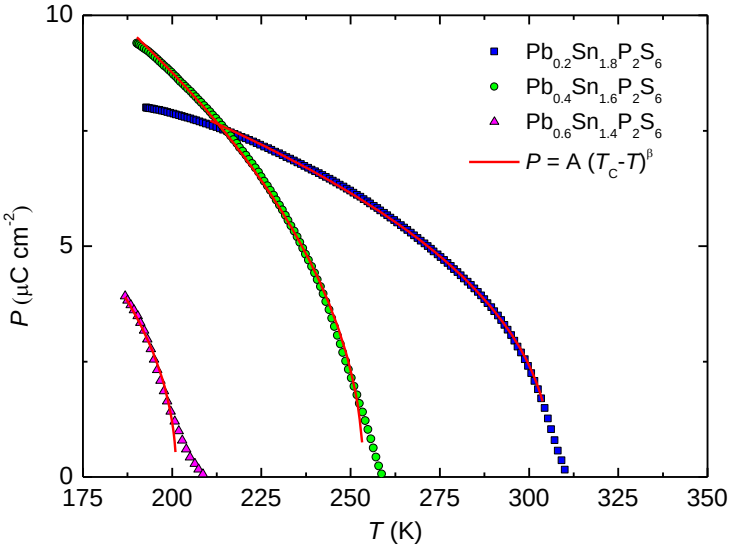

Fig. 26. Temperature dependence of spontaneous polarization of $(Pb_ySn_{1-y})_2P_2S_6$ single crystals (y=0.1, 0.2 and 0.3). Red solid lines represent fitting of the spontaneous polarization at $T<T_C$ by $P = A(T_C - T)^{\beta}$. The critical index β characterizes the order parameter behavior in the PT region.

For $(Pb_ySn_{1-y})_2P_2S_6$ solid solutions the order parameter is the spontaneous polarization P_S. We have expected that the spontaneous polarization can be well described by a power law formula with the critical exponent $\beta\approx1/2$ and our prediction based on Curie-Weiss constants ratio about the order of phase transition would be approved. A plot of polarization as a function of temperature (Fig. 26) gives the values of the polarization critical exponents of 0.47±0.002, 0.50±0.005 and 0.53±0.059 for y=0.1, 0.2 and 0.3, respectively. Shusta et al. have analysed how spontaneous polarization behaves in $(Pb_ySn_{1-y})_2P_2S_6$ solid solutions as well. From their spontaneous polarization measurements they found β=0.35±0.03 at atmospheric pressure for $(Pb_{0.2}Sn_{0.8})_2P_2S_6$. The reason for such a discrepancy is not known. Probably, it could be related to the pyroelectric measurement technique. The spontaneous polarization behaviour derived from the pyroelectric data depends on the degree of sample unipolarity. It shows that the results could be method dependent. The phase transition properties investigated by pyroelectric measurements are similar in $Pb_{0.4}Sn_{1.6}P_2S_6$ and $Pb_{0.6}Sn_{1.4}P_2S_6$ single crystals: the peaks of pyroelectric coefficients become broad and noisy, meanwhile in $Pb_{0.2}Sn_{1.8}P_2S_6$ sharp peak at 306.2 K is observed

indicating continuous phase transition from paraelectric to ferroelectric state. Such behaviour is in good agreement with dielectric measurements and confirms the possibility of the presence of the intermediate state in $Pb_{0.4}Sn_{1.6}P_2S_6$ and $Pb_{0.6}Sn_{1.4}P_2S_6$ single crystals. These results are compared with the corresponding ones found in literature. A number of papers reported a clear change in the behaviour of the phase transition of $Pb_{0.4}Sn_{1.6}P_2S_6$ and $Pb_{0.6}Sn_{1.4}P_2S_6$ single crystals [65], [84], [86], [111]. It was explained as follows: at higher lead content strong random field defects appear as well as coexistence of different phases which was well described by the BEG model [65], [84], [86]. The evolution of the ferroelectric transition with substitution of tin by lead in $(Pb_ySn_{1-y})_2P_2S_6$ mixed crystals is related to smaller stereoactivity of the Pb $6s^2$ electron lone pair. On the substitution of tin by lead, the sublattice of rather strongly stereoactive Sn^{2+} cations is diluted by weakly stereoactive Pb^{2+} cations, which also have a bigger ionic radius. In addition to the dilution effect, the ionicity of the Sn–S chemical bonds increases and the stereoactivity of the remaining Sn^{2+} cations decreases [65].

Ferroelectric characterization. Fig. 27 presents the temperature evolution of polarization hysteresis loops of the $(Pb_ySn_{1-y})_2P_2S_6$ single crystals with composition y = 0.1, 0.2 and 0.3. Ferroelectric hysteresis measurement is a good method to prove samples being ferroelectrics and quite sensitive to the presence of some defects. All investigated crystals exhibit usual well-saturated ferroelectric hysteresis loops. The shape of these hysteresis loops is not influenced by defects [86]. Probably, the explanation for such a behavior is that the defects are distributed uniformly in the crystal and they do not have a strong effect on the shape of *P-E* loop itself

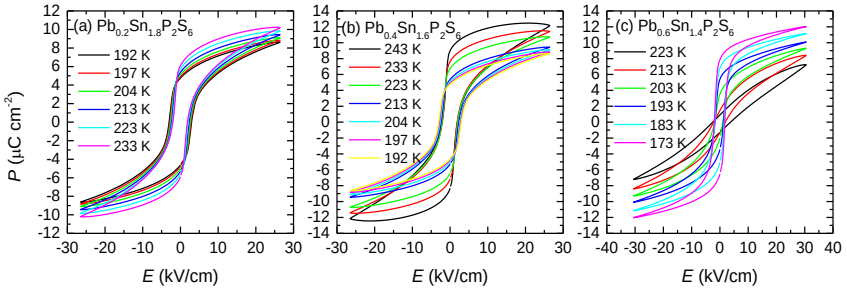

Fig. 27. Polarization hysteresis loops for $(Pb_ySn_{1-y})_2P_2S_6$ single crystals (y = 0.1, 0.2 and 0.3)

Spontaneous polarization obtained from ferroelectric hysteresis is equal to 11.9 μC cm^{-2} in $Pb_{0.4}Sn_{1.6}P_2S_6$ crystal, while the spontaneous polarization in a crystal with 30% lead impurities is reduced to 7.3 μC cm^{-2} near the phase transtion temperature. According to the literature, in a pure $Sn_2P_2S_6$ crystal spontanoeous polarization reaches 14 μC cm^{-2} at room temperature [105]. It is impossible to compare this value with the ones obtained by us because temperature range with respect to the phase transition point are quite different. Nevertheless, we could predict that spontaneous polarization in a pure $Sn_2P_2S_6$ is higher than in a mixed system. This can be attributed to the presence of crystal lattice defects in $(Pb_ySn_{1-y})_2P_2S_6$ system.

Summary. Structural phase transition characteristics in $(Pb_ySn_{1-y})_2P_2S_6$ single crystals (y = 0.1, 0.2 and 0.3) have been investigated by dielectric spectroscopy, pyroelectric properties and ferroelectric *P-E* loops analysis. The dielectric and pyroelectric measurements revealed anomalies in $Pb_{0.2}Sn_{1.8}P_2S_6$ crystal which are attributed to the ferroelectric phase transition, meanwhile with increasing lead content phase transition behaviour becomes much more complicated with some intermediate phase between ferroelectric and paraelectric states.

4.3.Influence of Ge doping in $(Pb_ySn_{1-y})_2P_2S(Se)_6$ single crystals

For $Sn_2P_2S_6$ (SPS) ferroelectrics the second order phase transition at T_0~337 K with mixed displacive – order/disorder character is occurred [64]. The spontaneous polarization is determined by three-well local potential for the order parameter fluctuations [72] [74]. Antiferroelectric-like double hysteresis presented earlier in this study is a direct experimental confirmation of three-well shape of the local potential in this proper uniaxial ferroelectrics. The experimental results of $(Pb_ySn_{1-y})_2P_2S_6$ showed that the phase diagram of $(Pb_ySn_{1-y})_2P_2S_6$ is not so simple and could be quite complicated with possible ferroelectric-paraectric states coexistence [84] [86]. This is in agreement with the thermodynamical description based on a Blume-Emery-Griffith (BEG) model with radom bond and random field defects, where the introduction of Pb is responsible for the randomness [65]. One more feature of phase diagram predicted by BEG model (presentend in Fig. 11) is the presence of tricritical point (TCP). According to the experimental data, for the $(Pb_ySn_{1-y})_2P_2S_6$ mixed crystals the paraelectric phase becomes stable above y>0.7 at a normal pressure [83], [87]. Also, in previous papers it was shown that for y>0.3 and below 220 K the hysteresis appears [86]. It is related to the paraelectric and ferroelectric phase

coexistence, and gives evidences about a discontinous character of the phase transition [65].

$SrTiO_3$ in chemically pure form was reported a typical quantum paraelectric featured by high dielectrc permittivity ε and low dielectric loss tanδ, absent of ferroelectric transitions down lo lowest temperatures [112], [113]. This effect is attributed to large quantum fluctuations in the limit of absolute zero temperature [113]. Besides $SrTiO_3$, $CaTiO_3$ and $KTaO_3$ are also classified as „quantum paraelectrics“, or so-called „incipient ferroelectrics“[114]. Very similar effects is also observed in the chemically or isotopic substituted $SrTiO_3$ ($SrTiO_3$:Ca or $SrTiO_3$:O^{18}) [115].

It was reported in pure $Pb_2P_2S_6$ single crystal „quantum paraelectric“ state [86], as it is classified according to work of Muller et al. [112] At 0 K, a material can be tuned to a quantum critical point (QCP) by applying pressure or changing chemical composition in mixed crystals $(Pb_ySn_{1-y})_2P_2S_6$ [116]. The quantum critical point (QCP) is a point at absolute zero temperature in a phase diagram, where the quantum flucatuations drive a phase transition. Thus, it may seem that a quantum phase transition is an abstract theoretical idea. However, the influence of the critical point extends over a wide range at $T>0$: this is the regime of quantum criticality.

In Fig. 28 the results of dielectric permittivity of $Pb_2P_2S_6$ single crystal is presented. It is shown that for $Pb_2P_2S_6$ single crystal, real part of dielectric permittivity increases monotonously with decreasing temperature in the measured temperature range. The saturation behavior of real part of dielectric permittivity is not observed. The clear dispersion of real part of dielectric permittivity is not detected. In the quantum critical regime the usual Curie-Weiss law of the inverse dielectric permittivty $1/\varepsilon(T)\sim T$ changes into $1/\varepsilon(T)\sim T^2$ [116]. That is the most prominent criterion of quantum critical behaviour. Other quantities such as the thermal expansion coefficient and soft-mode frequencies are expected to vary in an unconventional manner. As it is shown in the inset of Fig. 28, the inverse dielectric permittivity $1/\varepsilon(T)$ exhibits the expected non-classical T^2 temperature dependence over a finite temperature range above approximately 50 K and below 250 K. Typically, there is no ferroelectric phase transition in quantum paraelectrics, but critical behaviour, manifested by the non-classical T^2 dependece, is occured [117].

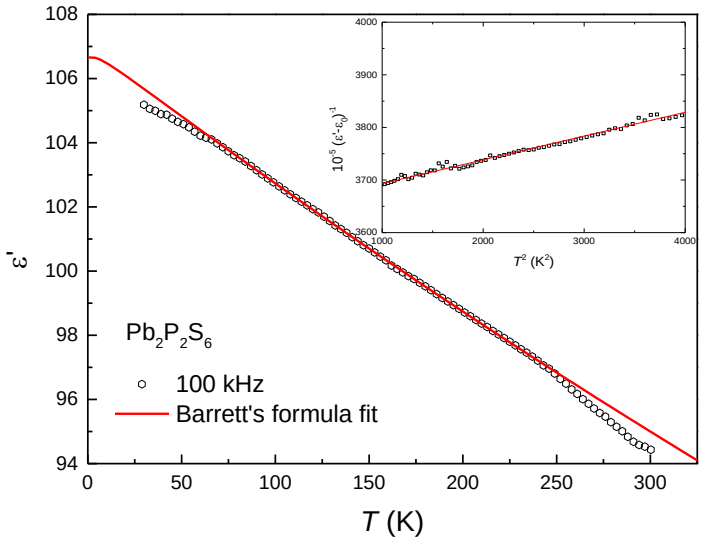

Fig. 28. The temperature dependences of real part of dielectric permittivity of $Pb_2P_2S_6$ single crystal. The inset shows the non-clasical $1/\varepsilon(T)\sim T^2$ behavior of $Pb_2P_2S_6$ quantum paraelectric.

In order to describe the temperature dependencies of the dielectric permittivity of quantum paraelectrics, Barrett extended Slater's mean-field theory by including the quantum effect, and an equation was derived as:

$$\varepsilon(T) = \frac{C}{\left(\frac{T_1}{2}\right)\coth\left(\frac{T_1}{2T}\right) - \theta_{CW}} + \varepsilon_0 \qquad (22)$$

where C is the Curie-Weiss constant, θ_{CW} can be recognized as the classical paraeletric Curie temperature, ε_0 is a temperature-independent constant, T is the sample temperature and T_1 is recognized as the temperature at which the instability begins. Roughly, it may be considered that T_1 is the dividing point between the low temperature where quantum effects are important so ε deviates from Curie-Weiss law, and the high temperature region where a classical approximation and Curie-Weiss law are valid [117].

In the low temperature region ($T<T_1$), the quantum effect takes place. In many cases, $\theta_{CW} \leq 0$ K, which refers to virtual transition temperature. Therefore, the material does not undergo a ferroelectric phase transition at any finite temperature. When, θ_{CW} is finite and $\theta_{CW} < T_1$, the quantum fluctuations that occur below T_1 break the long-range ferroelectric order and

stabilize the quantum paraelectric state in the sample and a probable ferroelectric transition occurs at θ_{CW} [118]. The dielectric data of $Pb_2P_2S_6$, $(Pb_{0.98}Ge_{0.02})_2P_2S_6$, $(Pb_{0.7}Sn_{0.3})_2P_2S_6$+5%Ge and $(Pb_{0.7}Sn_{0.3})_2P_2Se_6$+5%Ge single crystals were analysed on the basis of Barrett`s formula (22). The results are presnted in Figs. 28, 29, 32 and 34, respectively. The solid lines represent fitting with Barrett`s formula. The bestt-fit parameter values of all the measured samples are summarized in Table 1.

The deviation from Barrett`s equation for $Pb_2P_2S_6$ starts around 75 K. The obtained parameter values (T_1=99 K and θ_{CW}=-363 K) of pure single crystal $Pb_2P_2S_6$ demonstrate that material does not undergo ferroelectric phase transition at any finite temperature.

Lead substitutes tin and selenium takes place of sulfur in a whole concentration range of $(Pb_ySn_{1-y})_2P_2(Se_xS_{1-x})_6$ mixed crystals. In addition, these crystals can be doped with germanium Ge, antimony Sb or tellurium Te, but only in small percentages. Germanium is the most important dopant because it takes place of tin in the $Sn_2P_2S_6$-type crystals. It is known that the tin ions play an important role in the ferroelectricity of the material. Introducing Ge atoms into the cation sublattice of SPS crystal enhances the stereoactivity of the cation sublattice, increasing the critical temperature and sharpening the phase transition character. An increase of the transition temperature had already been observed in paper [111] measuring the temperature evolution of the piezoelectric and pyroelectric coefficients. It is worth noting that when Pb substitutes Sn the hybridization becomes weaker, reducing the phase transition temperature. On the other hand, Ge dopant in $Pb_2P_2S_6$-type crystals plays an opposite role: it enhances the total stereoactivity of the crystal.

It is known that small amount of impurities in quantum paraelectrics could induce ferroelectricity [119], [120]. The transition to a polar state appears above some impurity critical concentration x. A widely accepted viewpoint is that the ferroelectricity in doped-quantum paraelectrics is determined by an off-center position of impurity ions which produces electric dipoles interacting with a polarization. Thus, it is interesting to investigate how germanium impurities can affect quantum paraelectric state of $Pb_2P_2S_6$. Fig. 29 shows the temperature dependence of real part of dielectric permittivity of $(Pb_{0.98}Ge_{0.02})_2P_2S_6$. The inset of Fig. 29 confirms the non-clasical T^2 behaviour of the inverse dielectric permittivity. Needless to say, T^2 temperature dependence is not valid at low temperatures. For the doped-system $(Pb_{0.98}Ge_{0.02})_2P_2S_6$, both temperatures ($T_1$ and θ_{CW}) are finite (Table 1). Also, since $\theta_{CW} < T_1$ for $(Pb_{0.98}Ge_{0.02})_2P_2S_6$, it could be concluded that the long-range ferroelectric order in this Ge-doped sample is broken due

to quantum fluctuations below 207 K, and a probable ferroelectric transition occurs. These differences of $Pb_2P_2S_6$ and $(Pb_{0.98}Ge_{0.02})_2P_2S_6$ crystals could be related with different ionic radius of Pb^{2+} (r_{Pb}=1.33 Å) and Ge^{2+} (r_{Ge}=0.87 Å). The smaller germanium ionic radius results in different hybridziation with the sulfur ions. Thus, doping with germanium induces some disorder effects and decreases dielectric permittivity value below 75 K deviating from Barrett`s fit (Fig. 29). It suggests that possible phase transition might occur in this region.

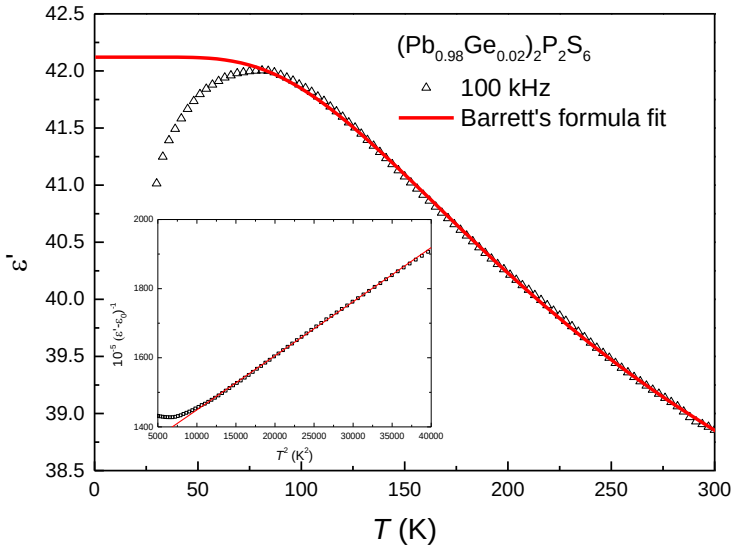

Fig. 29. Temperature dependence of dielectric permittivity of $(Pb_{0.98}Ge_{0.02})_2P_2S_6$. The inset shows the temperature dependence of the inverse dielectric function in $(Pb_{0.98}Ge_{0.02})_2P_2S_6$.

Temperature dependence of the dielectric permittivity of $(Pb_{0.98}Ge_{0.02})_2P_2S_6$ is presented in Fig. 30. Peak of dielectric permittivity is broad. The broadness of the phase transition is due to small compositional fluctuations. However, there is two peaks of the imaginary part of dielectric permittivity with a frequency dispersive behavior, and the temperatures of the loss peaks are around 50 K and 100 K at 100 kHz.

The relaxation rate derived from the maximum values of the imaginary part of the permittivity (Fig. 30) can be well fitted to the Arrhenius law:

$$\nu = \nu_0 \exp(\frac{E_A}{kT}) \quad (23)$$

where ν_0 is the relaxation rate at the infinite temperature, E_A is the activation energy for the relaxation, k is the Boltzmann constant and T is the temperature. The best-fitting value of the activation energy is equal to 0.41 eV.

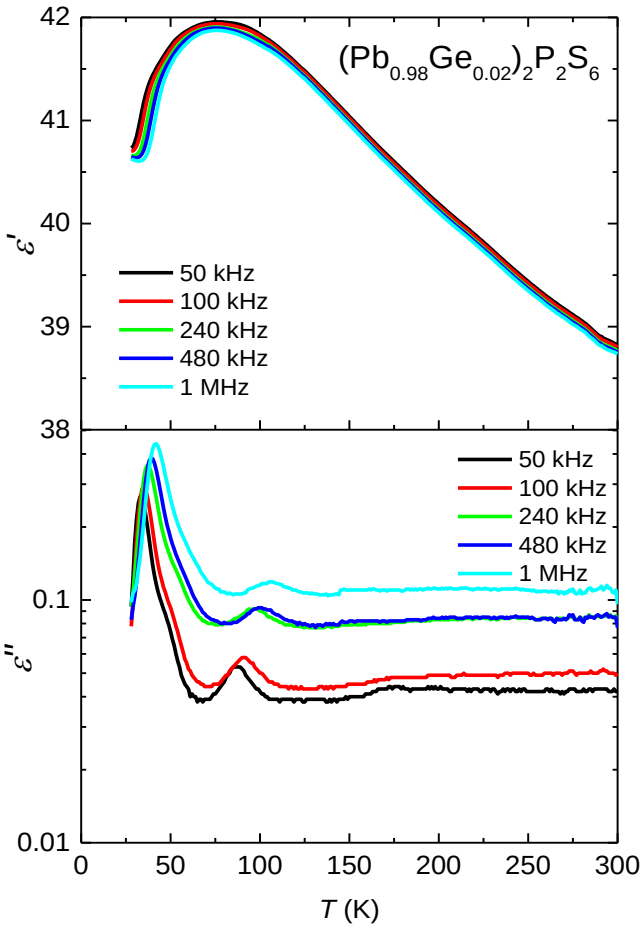

Fig. 30. Dielectric permittivity as a function of temperature at different frequencies for $(Pb_{0.98}Ge_{0.02})_2P_2S_6$ sample.

$Pb_2P_2S_6$ compounds have a stable paraelectric ground state till 0 K when lead concentration reaches y~0.7 [86]. In the previous papers it was shown that, $(Pb_ySn_{1-y})_2P_2S_6$ mixed crystals with compositions y~0.61 and y~0.65, which are close to the transition at zero temperature from polar phase (y<0.7)

to paraelectric one (y>0.7), the dielectric susceptibility demonstrates the quantum critical behavior in vicinity of the first order transitions with T_C~35K and 20 K, respectively [83]. To study the effect that the addition of Ge dopants has on the quantum paraelectric nature of $Pb_2P_2S_6$ compounds was precisely the aim of further investigations of $(Pb_{0.7}Sn_{0.3})_2P_2S_6$ + 5% Ge and $(Pb_{0.7}Sn_{0.3})_2P_2Se_6$ + 5% Ge samples. In these samples it was realized Sn^{2+} sites codoping with two different ionic radius impurities – lead and germanium. It is worth to remind that the substitution Sn has the strongest effect because the ferroelctric phase transition is induced by the stereoactivity of the Sn^{2+} cation $5s^2$ eectron one pair. However, it is known that lead and germanium have very different influences on the phase transitions.

Temperature dependence of the real and imaginary parts of dielectric permittivitty for $(Pb_{0.7}Sn_{0.3})_2P_2S_6$ + 5% Ge samples is shown in Fig. 31. From room temperature to 20 K, ε` increases continuously with decreasing temperature attaining a value 475 at 20 K. However, there is a loss tangent peak with a frequency -dispersive behavior, and the temperature (T_m) of the loss peak is around 50 K at 100 kHz.

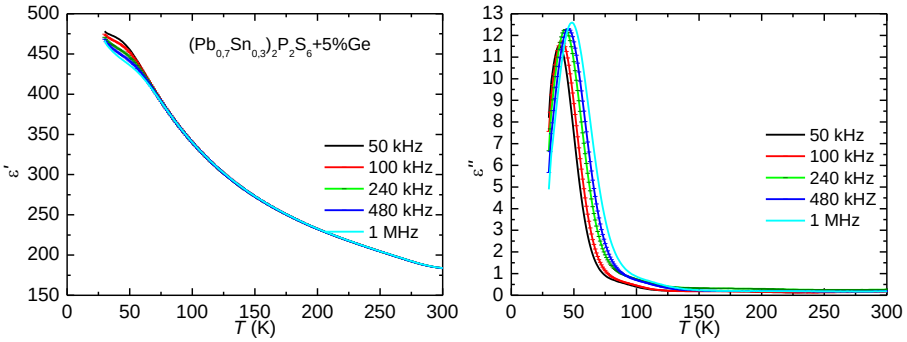

Fig. 31. Dielectric permittivity as a function of temperature at different frequencies for $(Pb_{0.7}Sn_{0.3})_2P_2S_6$+5% Ge sample.

For $(Pb_{0.7}Sn_{0.3})_2P_2S_6$+5%Ge, by fitting to Barrett`s equation (22), T_1=57.7 K,θ_{CW}=-17.5 K, and C=33 390 K were obtained. From the Fig. 32 it can be seen that the fitting data are good in agreement with the experimental data. The obtained values demonstrate that the sample does not undergo a ferroelectric phase transition at any finite temperature.

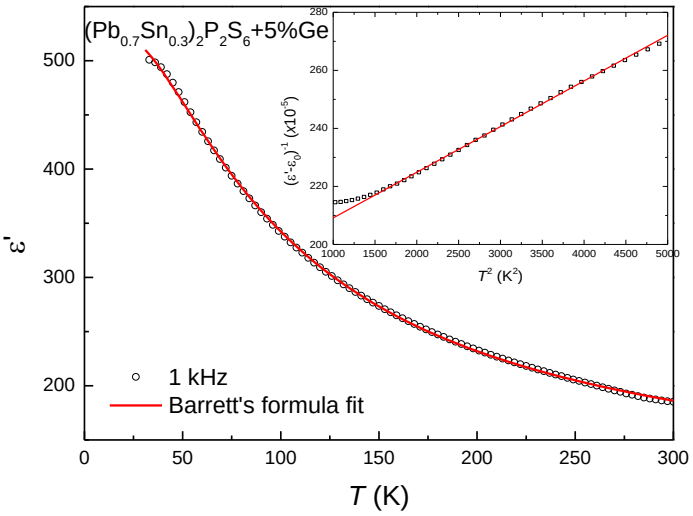

Fig. 32. Temperature dependence of the dielectric permittivity of $(Pb_{0.7}Sn_{0.3})_2P_2S_6$+5%Ge. Circles represent experimental data at 1 kHz, the solid curve – fitting according to the Barret`s equation (22). The inset shows the temperature dependence of the inverse dielectric function in $(Pb_{0.7}Sn_{0.3})_2P_2S_6$+5%Ge.

Temperature dependence of the dielectric permittivity as a function of frequency for $(Pb_{0.7}Sn_{0.3})_2P_2Se_6$ + 5% Ge is shown in Fig. 33. From 300 to 20 K, ε` increases continuously with decreasing temperature attaining the value 900 at 20 K.

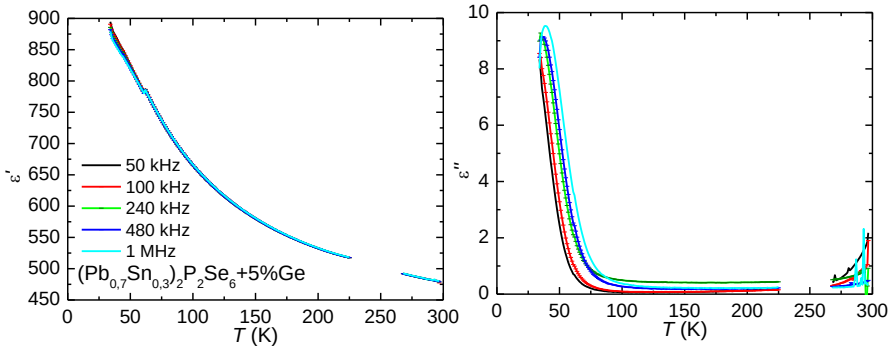

Fig. 33. Dielectric permittivity as a function of temperature at different frequencies for $(Pb_{0.7}Sn_{0.3})_2P_2Se_6$+5% Ge sample.

Table 1. Comparison of values obtained by fitting Barrett relation (22) for various compounds

Compound	C (K)	T_1 (K)	θ_{CW} (K)	ε_0
$(Pb_{0.7}Sn_{0.3})_2P_2Se_6$+5%Ge	34970	51.8	-8.8	370
$(Pb_{0.7}Sn_{0.3})_2P_2S_6$+5%Ge	33390	57.7	-17.5	82
$(Pb_{0.98}Ge_{0.02})_2P_2S_6$	1208	207	39.9	35
$Pb_2P_2S_6$	32890	99	-363	78

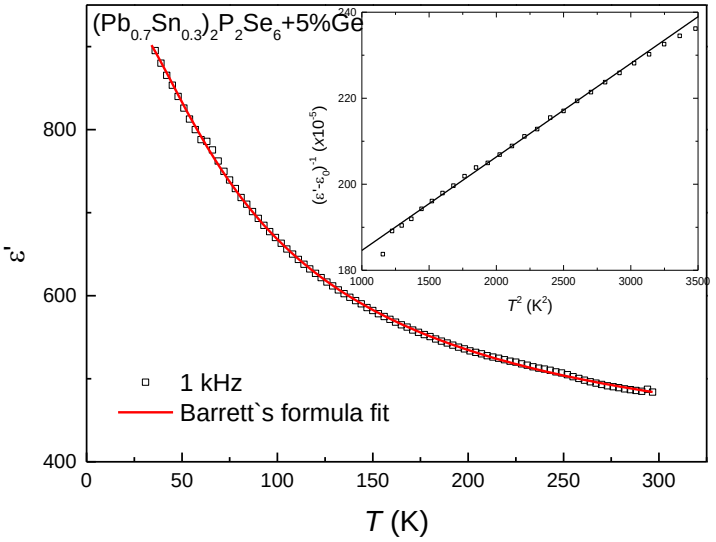

Fig. 34. Temperature dependence of the dielectric permittivity of the $(Pb_{0.7}Sn_{0.3})_2P_2Se_6$+5% Ge crystal. Circles represent experimental data at 1 kHz, the solid lines – fitting according to the Barret`s equation (22). The inset shows the temperature dependence of the inverse dielectric function in $(Pb_{0.7}Sn_{0.3})_2P_2Se_6$+5% Ge.

Summary. Ge doped $(Pb_ySn_{1-y})_2P_2S(Se)_6$ samples were used in these experiments. Dielectric measurements were carried out in the parallel plate capacitance geometry. Measurements were performed during heating at a rate of less than 0.5 K/min. The quantum paraelectric state was reported in these samples at low temperatures. In all of these materials on the border of ferroelectricity non-classical T^2 temperature dependencies of the inverse dielectric was observed.

4.4.Dielectric spectroscopy of $AgCrP_2S_6$ and $Cu_{0.2}Ag_{0.8}CrP_2S_6$ crystals

The results of low-frequency measurements of pure $AgCrP_2S_6$ and Cu-added $Cu_{0.2}Ag_{0.8}CrP_2S_6$ crystals are presented in Fig. 35. Differently from the $CuCrP_2S_6$ and $CuInP_2S_6$ no anomalies of complex dielectric permittivity indicating the polar phase transition has been observed down to the lowest temperature in presented crystals. The real part of dielectric permittivity of $Cu_{0.2}Ag_{0.8}CrP_2S_6$ crystal is almost a constant below 150 K and its value is 19.5, which is smaller than in pure $CuCrP_2S_6$ (the real part of dielectric permittivity at low temperature is 25). $AgCrP_2S_6$ show even smaller value (close to 10). The constant dielectric permittivity of $AgCrP_2S_6$ and $Cu_{0.2}Ag_{0.8}CrP_2S_6$ crystals at low temperatures is mainly caused by phonons. In $CuCrP_2S_6$ the antiferroelectric phase transition is driven by the soft phonon mode [121], [122]. Therefore, the decrease of the dielectric permittivity at low temperatures by substitution Ag→Cu in $Ag_xCu_{1-x}CrP_2S_6$ crystals can be caused by the disappearance of the low frequency phonon mode or by the increase of their frequency, according to the Lyddane-Sachs-Teller relation [123].

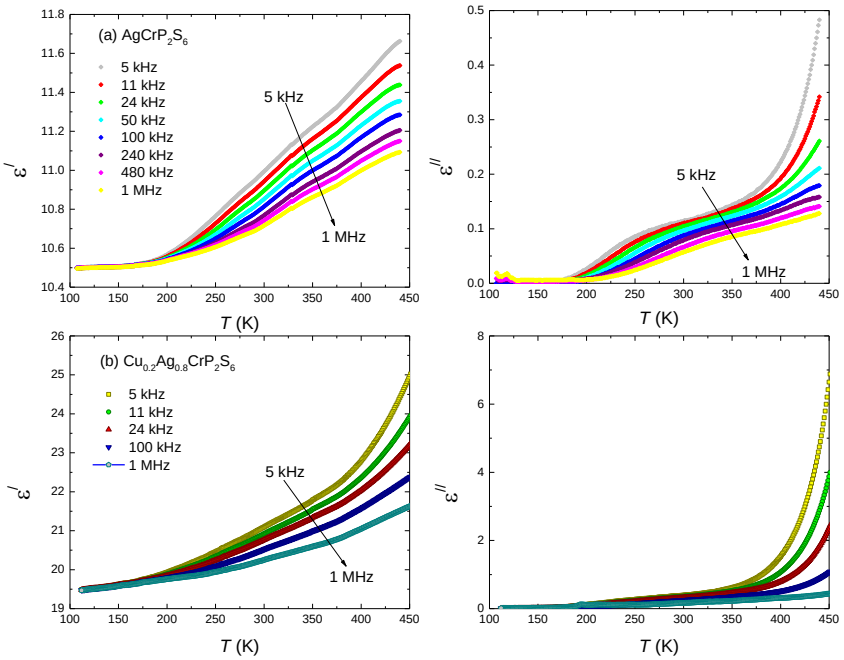

Fig. 35. Temperature dependence of the complex dielectric permittivity of $AgCrP_2S_6$ (a) and $Cu_{0.2}Ag_{0.8}CrP_2S_6$ (b) crystals at different frequencies.

At low temperatures, measurements show the dielectric behavior with comparatively low dielectric losses. Dielectric losses start increasing above 400 K and cause an increase of the real part of the dielectric permittivity in $Cu_{0.2}Ag_{0.8}CrP_2S_6$ crystal. Such a behavior indicates the electric conductivity, which is much smaller than in $CuCrP_2S_6$ [124]. Generally, conduction phenomena dominate in dielectric spectra of investigated crystals above 200 K temperature.

The real part of electrical conductivity σ' has been calculated according to the equation:

$$\sigma' = \omega\varepsilon_0\varepsilon'' \qquad (24)$$

The obtained frequency dependencies of conductivity for pure and Cu-added crystals are presented in Fig. 36. It was observed that the conductivity spectra indicate several different regions within the measured frequency range: plateau region corresponds to the frequency independent conductivity, known as DC conductivity, and the conductivity dispersion regions. The variation of σ with frequency at different temperatures was fitted according to the Almond-West type power law with a single exponent:

$$\sigma = \sigma_{DC} + A\omega^n \qquad (25)$$

where σ_{DC} is the DC conductivity, and $A\omega^n$ is the AC conductivity. From the fitting lines, it can be seen that conductivity spectra obey Almond-West power law quite well except for an additional low frequency dispersion region due to electrode effects. As has already been described, these effects are only important at lower frequencies and higher temperatures.

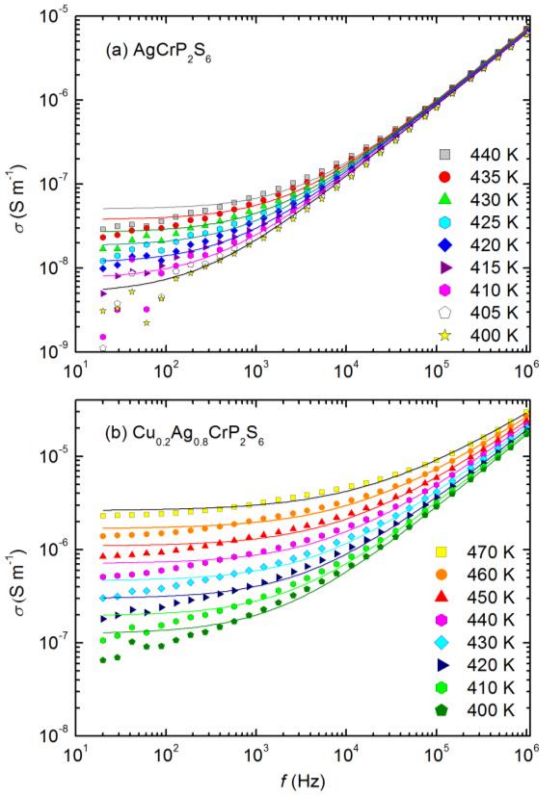

Fig. 36. Frequency dependence of conductivity σ for $AgCrP_2S_6$ (a) and $Cu_{0.2}Ag_{0.8}CrP_2S_6$ (b) crystals at several temperatures.

The reciprocal temperature (1000/T) dependence of $\ln(\sigma_{DC})$ is plotted in Fig. 37. From the slope of this dependence it is possible to calculate the activation energy E_A for the conduction process. Generally, the conductivity variation with temperature follows the Arrhenius law given by:

$$\sigma_{DC} = \sigma_0 e^{-\frac{E_A}{kT}} \qquad (26)$$

with the calculated parameters E_A= 1.26 eV and E_A= 0.75 eV for pure and Cu-added crystals, respectively. Activation energies of bulk conductivity calculated from complex impedance spectra are in good agreement with these DC conductivity activation energies.

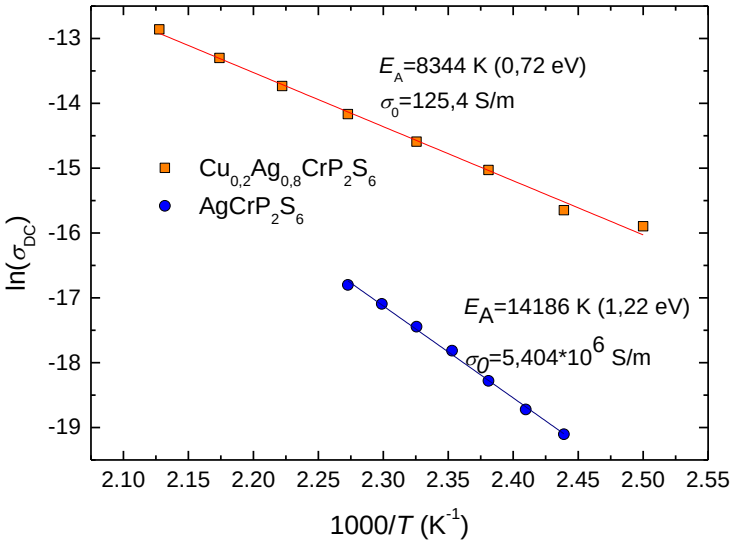

Fig. 37. Arrhenius plot of $\sigma_{DC}\cdot T$. Points represent experimental data, solid lines – the best fit according to Arrhenius relation.

By comparison conductivity parameters for $AgCrP_2S_6$ and $CuCrP_2S_6$ (Table 2) crystals, Ag→Cu substitution cause a decrease of the activation energy of electric conductivity. It was suggested that in $CuCrP_2S_6$ and $CuInP_2S_6$ crystals [125] Cu^1-Cu^2 hopping motion is the reason for the ionic conductivity. The DC conductivity is about 10 times higher in Cu-added crystals comparing with pure $AgCrP_2S_6$. Therefore, we can assume having different conduction mechanisms in both materials. However, it should be confirmed by more comprehensive investigations.

Table 2. Parameters of the Arrhenius law obtained from the conductivity measurements of various layered crystals.

Crystals	E_A (eV)	σ_0 (S m^{-1})	Reference
$AgCrP_2S_6$	1,22	$5{,}404\cdot10^6$	This study
$Cu_{0.2}Ag_{0.8}CrP_2S_6$	0,72	125	This study
$CuCrP_2S_6$	0,67	-	[125]
$AgInP_2S_6$	0,67	883	[126]
$Ag_{0.1}Cu_{0.9}InP_2S_6$	0,55	812	[14]

Summary. The dielectric properties of newly synthesized $AgCrP_2S_6$ and $Cu_{0.2}Ag_{0.8}CrP_2S_6$ phosphorous chalcogenide crystals are presented. The meaurements were performed in the frequency and temperature ranges 20 Hz to 1 MHz and 110 K to 470 K, respectively. No anomalies of complex dielectric permittivity indicating the polar phase transition can be detected in the measured temperature range. Dielectric spectra at high temperatures are mostly influenced by the electrical conductivity. From DC conductivity the activation energies have been calculated and compared with $CuCrP_2S_6$. The activation energies of the conductivity were found to be 1.26 eV and 0.75 eV for $AgCrP_2S_6$ and $Cu_{0.2}Ag_{0.8}CrP_2S_6$, respectively.

4.5.Low-frequency noise spectroscopy of lammelar $CuInP_2S_6$

Copper indium thiophosphate $CuInP_2S_6$, which belongs to the phosphorus chalcogenide family, was selected for the further noise studies. The structure of this layered material is defined by sulfur framework where the octahedral voids are filled with Cu and In cations, whereas P−P pairs form a triangular pattern within the interlinked sulfur cages [127]. The symmetry reduction from the paraelectric to the ferrielectric, at the first-order phase transition, occurs at T_C = 315 K, and is driven by the ordering in the copper sublattice and the displacement of cations from the centrosymmetric positions in the indium sublattice (C2/*c* to C*c* symmetry). According to the experimental results, the direction of the spontaneous polarization vector, at the onset of phase transition into the ferrielectric phase, is perpendicular to the layered planes [15], [128].

The voltage fluctuation spectral density of $CuInP_2S_6$ crystal as a function of the temperature at 128 Hz, is shown in Fig. 38(a). The noise intensity is constant and low below phase transition temperature T_C=315 K. In the vicinity of the phase transition (T>315 K) the noise level is increasing. Fig. 38(b) shows the noise of a white nature in the temperature ranges out of phase transition.

At temperatures higher than 315 K random telegraph signal (RTS) noise is observed, which indicates the jumps between the two states of the physical system. This type of noise is often observed in materials including the ferroic origin and called random telegraph signal (RTS) noise [88]. Superimposition of several RTS components gives 1/*f*-type noise spectra. From several repetitions of noise measurements, it is clear that noise spectroscopy is a sensitive tool for the qualitative phase transition detections in ferroelectric crystals.

Structural measurements were carried out, and such a noise behaviour repeats the structural results [3]. It will be shown by further spectral analysis.

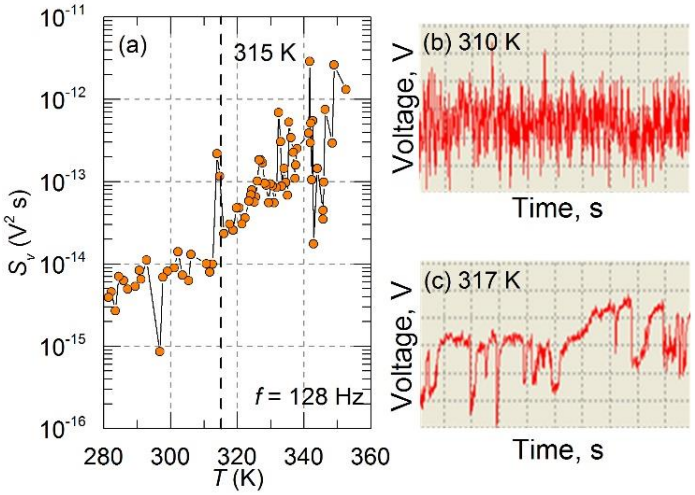

Fig. 38. Noise voltage spectral density dependence on temperature at 128 Hz frequency (for $CuInP_2S_6$). Figure (b) and (c) shows typical time dependences of voltage fluctuation at certain temperatures below and above the phase transition.

The voltage fluctuation spectral density as a function of frequency in the temperature region of 300–340 K is presented in Fig. 39(a). Low-frequency noise data revealed that only the "white" noise component is visible in the $CuInP_2S_6$ crystal at room temperature (300 K). At all measured temperatures above 315 K, noise behavior obviously changes, indicating phase transition: the voltage fluctuation spectra become 1/*f*-type (flicker noise) in nature. In the most condensed matter systems, 1/*f*–type noise arises because of fluctuation of the number of free charge carriers in the sample owing to their emission and capture by localized states in defects [91]. In the further analysis of the 1/*f* noise in the $CuInP_2S_6$ crystal, it will considered that flicker noise in the investigated crystal arises because of the superposition of the individual capture and emission noise sources with different relaxation times [93]. These noise sources can be resolved into distinct generation-recombination (GR) processes.

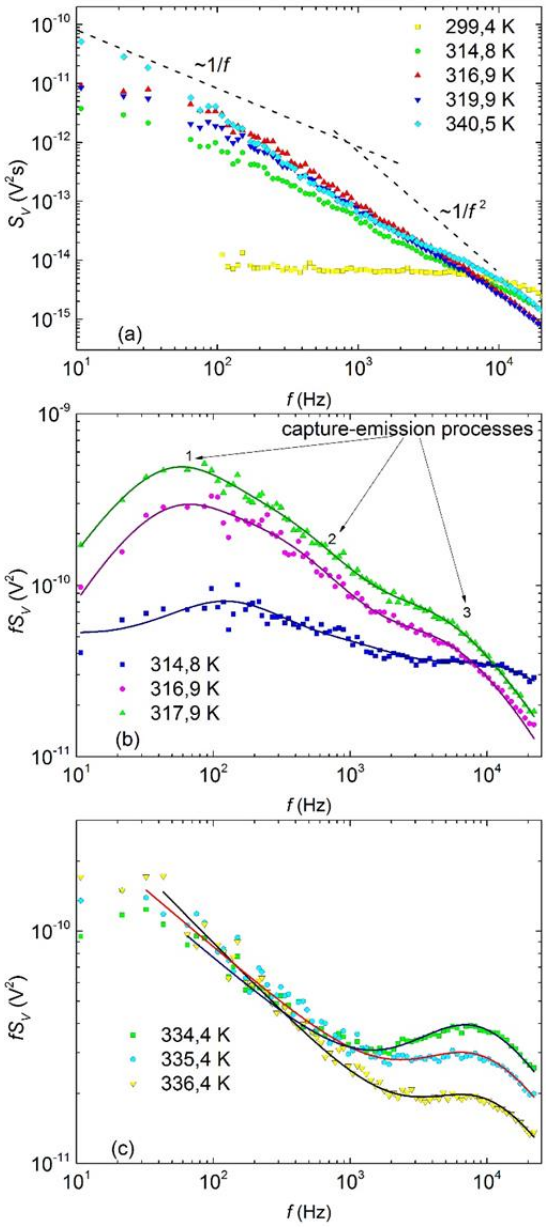

Fig. 39. Voltage fluctuations spectra of $CuInP_2S_6$ at several temperatures (a), noise voltage spectral density multiplied by frequency of $CuInP_2S_6$ taken at two different temperature ranges: 314-318 K (b) and 334-336 K (c). The solid lines represent fitting using (27) formula.

In general, the power spectral density of voltage fluctuations can be decomposed into independent components of $1/f^{\alpha}$, Lorentzian-type (with characteristic time constant τ) and white noise term S_{white}:

$$S(f) = \frac{A}{f^{\alpha}} + \sum_{i=1}^{n} \frac{2\tau_i A_{gr_i}}{1 + (2\pi f \tau_i)^2} + S_{white} \quad (27)$$

where, A is a frequency independent but temperature dependent constant that measures the strength of the $1/f$ type contribution and A_{gri} measures the strengths of the individual Lorentzians with characteristic corner frequency τ^{-1}. Since the discrete Lorentzians in most cases originate from generation-recombination mechanism, refered as GR type noise. There are several distinct generation-recombination processes, each with a distinct characteristic time τ_i. The white noise term S_{white} is included since it is almost always present experimentally and needs to be accounted.

Since $1/f$ noise is usually dominant over the other types of noise, small generation-recombination (GR) peaks are not visible in the spectra. In order to obtain a deeper insight into the mechanism of observed noise, the voltage spectral density (Fig. 39(a)) was normalized by multiplying the corresponding frequency. Thus, the resulting spectra clearly show relaxational peaks in the temperature ranges of 315 K–319 K (Fig. 37(b)) and 334 K–336 K (Fig. 39(c)) with the capture and emission processes.

To prove this statement, considerable fitting of measured noise spectra using equation (27) was performed. It was found that observed noise spectra could be characterized by a contribution of $1/f^{\alpha}$ -type noise and Lorentzian-type spectra. The voltage fluctuation spectral density follows the universal $1/f^{\alpha}$ law with $\alpha \approx 1.5$ in both temperature ranges. Every component of the equation (27), has a maximum at temperatures when $\omega\tau_i \approx 1$, as it is shown in Figs. 39(b-c). The fitting by equation (27) allows to extract characteristic time constants and hence activation energies, assuming that the relaxation times have a thermally activated character determined by the Arrhenius law:

$$\tau_i = \tau_0 \exp\left(\frac{\Delta E_A}{kT}\right) \quad (28)$$

where τ_0 is the characteristic time, ΔE_A is the activation energy of the recombination centers, T is the temperature of the samples and k is the Boltzmann constant.

In Fig. 39(b), it was presented spectra at 315–319 K (slightly above the phase transition temperature) fitted by three different capture and emission processes. All the peaks are related to thermally activated processes

described by Arrhenius law. The characteristic time constants extracted from observed maxima follow the Arrhenius law (28) with activation energies 0.57 eV, 0.74 eV, and 0.1 eV. Figure 37(c) displays the temperature range 334–336 K with contribution from $1/f^{1.5}$ noise and relaxational process that follows the Arrhenius law with activation energy equal to 0.68 eV. Application of noise spectroscopy is a relatively new area in the field of ferroelectric materials. It needs an explanation that correlates the processes observed in noise spectra with the features of certain materials. According to some studies of noise behavior in ferroelectrics [100], the polarization relaxa- tion in local polar-regions and conductivity are the main contribution to the origin of $1/f$ noise in the ferroelectric system. It should be noted that $1/f$ noise is observed in the non-polar paraelectric phase, and the latter interpretation of noise origin would be the most appropriate in our case. Obviously, process marked 1 (with the longest characteristic time constant) could be linked to some additional noise source in the ferroelectric regime that is related to the phase transition dynamics. An activation energy of process no. 2 (E_A=0.74eV) coincides well with ionic conductivity activation energy [125]. The generation-recombination type process at higher temperature with an activation energy of 0.68 eV is also attributed to the copper ion hopping. An activation energy decrease with the temperature can be explained with increasing copper jumps to the interlayer space [3].

There is a question about a clear identification of process no. 3 with 0.1 eV activation energy. It has been already established that noise has a defect origin; especially surface defects play a noticeable role. From previous studies it is known that the forbidden energy gap of $CuInP_2S_6$ is 3.1 eV [129]. Since our calculated activation energy falls into the forbidden energy gap, we determine effective energy barriers of process no. 3 by the pinning energy of defects. The ferroelectric hysteresis loop was measured in order to show the crystal being of ferroelectric origin and to prove the presence of some defects. According to the literature, a spontaneous polarization of 2.55 $\mu C\ cm^{-2}$ and a coercive field of 77 $kC\ cm^{-1}$ were observed in $CuInP_2S_6$ only at room temperature [3]. Here it was measured the thermal evolution of ferroelectric hysteresis loop for the $CuInP_2S_6$ crystal in the temperature region from 193K to 313K (Fig. 40).

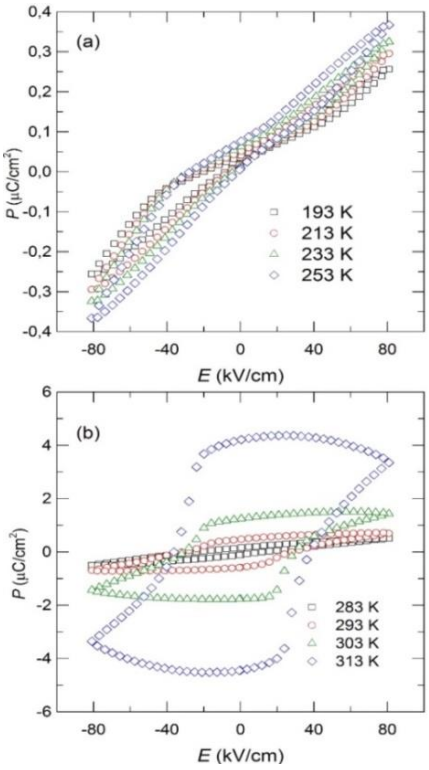

Fig. 40. *P-E* hysteresis loops of the $CuInP_2S_6$ crystal.

We observed some *P–E* loops off-set which can be attributed to the stabilized defects. Such an antisymmetric shape of the loops could be attributed to the pinning of domain walls [18], [19]. The pinched hysteresis loop behavior could be interpreted using the concept of memristive devices . The bending of the hysteresis loop at temperature close to T_C, could be related to quite high electric conductivity in this material.

Summary. The noise spectroscopy of the $CuInP_2S_6$ lamellar ferrielectric crystal at phase transition for temperatures from 300K to 340K over the frequency range 10Hz–20kHz was carried out. Lorentzian-type spectra, due to thermally activated carrier capture and emission processes, were observed in voltage fluctuations. An investigation of the temperature and frequency-dependent features of the noise spectra in $CuInP_2S_6$ enables to conclude that low-frequency noise can be explained by copper ion motion contribution and fluctuations of trap charges. The observed process is attributed to the generation-recombination at trap defect states. Ferroelectric hysteresis measurements approved pinning of the domain walls in the investigated crystal.

CONCLUSIONS

1. Peculiar polarization switching in the form of double hysteresis loops in bulk proper uniaxial ferroelectrics $Sn_2P_2S_6$ crystal was observed. Such a peculiarity is related to the three-well shape of the local potential for spontaneous polarization fluctuations, which determine the possibility of the existence of metastable nonpolar regions below the second-order phase-transition temperature. An enhanced quantum anharmonic model is proposed. This model can explain the coexistence of ferroelectric and antiferroelectric hysteresis loops in $Sn_2P_2S_6$ crystals.

2. The characteristics of structural phase transition in $(Pb_ySn_{1-y})_2P_2S_6$ single crystals (y=0.1, 0.2 and 0.3) have been investigated by dielectric spectroscopy, pyroelectric properties and ferroelectric *P-E* loops analysis. The dielectric and pyroelectric measurements revealed anomalies in $Pb_{0.2}Sn_{1.8}P_2S_6$ crystal which are attributed to the ferroelectric phase transition, meanwhile with increasing lead content the phase transition behaviour becomes much more complicated with coexistence of ferroelectric and paraelectric phases.

3. $Pb_2P_2S_6$-type crystals can exhibit a quantum paraelectric state that can be understood in terms of Barrett`s model over a wide temperature range. By introducing small amounts (2%) of germanium dopants, the ferroelectric phase appears.

4. The noise spectroscopy has been employed to analyze $CuInP_2S_6$ crystal at phase transition for temperatures from 300K to 340K over the frequency range 10Hz–20kHz. An investigation of the temperature and frequency-dependent features of the noise spectra in $CuInP_2S_6$ enables to conclude that low-frequency noise can be explained by copper ion motion contribution and fluctuations of trap charges.

REFERENCES

[1] C. D. Carpentier and R. Nitsche, “Vapour growth and crystal data of the thio(seleno)-hypodiphosphates $Sn_2P_2S_6$, $Sn_2P_2Se_6$, $Pb_2P_2Se_6$ and their mixed crystals,” *Mater. Res. Bull.*, vol. 9, no. 4, pp. 401–410, 1974.

[2] Y. Vysochanskii, “Ferroelectricity in complex chalcogenides $M'M''P_2X_6$ (M′, M″ - Sn, Pb, Cu, In, Cr; X - S, Se),” *Ferroelectrics*, vol. 218, no. 1, pp. 275–282, 1998.

[3] V. Maisonneuve, V. Cajipe, A. Simon, R. Von Der Muhll, and J. Ravez, “Ferrielectric ordering in lamellar $CuInP_2S_6$,” *Phys. Rev. B*, vol. 56, no. 17, pp. 10860–10868, 1997.

[4] X. Bourdon, V. Maisonneuve, V. . Cajipe, C. Payen, and J. . Fischer, “Copper sublattice ordering in layered $CuMP_2Se_6$ (M=In, Cr),” *J. Alloys Compd.*, vol. 283, pp. 122–127, 1999.

[5] M. Gave, D. Bilc, S. Mahanti, J. Breshears, and M. Kanatzidis, “On the lamellar compounds $CuBiP_2Se_6$, $AgBiP_2Se_6$ and $AgBiP_2S_6$. Antiferroelectric phase transitions due to cooperative Cu^+ and Bi^{3+} ion motion,” *Inorg. Chem.*, vol. 44, pp. 5293–303, 2005.

[6] A. Dziaugys *et al.*, “Phase Transitions in Layered Semiconductor - Ferroelectrics,” in *Ferroelectrics - Characterization and Modeling*, M. Lallart, Ed. InTech, 2011, pp. 153–180.

[7] V. Maisonneuve, M. Evain, C. Payen, V. B. Cajipe, and P. Molinié, “Room-temperature crystal structure of the layered phase $Cu^{I}In^{III}P_2S_6$,” *J. Alloys Compd.*, vol. 218, no. 2, pp. 157–164, 1995.

[8] Y. Li and D. J. Singh, “Properties of the ferroelectric visible light absorbing semiconductors: $Sn_2P_2S_6$ and $Sn_2P_2Se_6$,” *Phys. Rev. Mater.*, vol. 1, no. 7, pp. 0754021–0754024, 2017.

[9] M. Zhao, G. Gou, X. Ding, and J. Sun, “Enhancing Visible Light Absorption for Ferroelectric $Sn_2P_2S_6$ by Se Anion Substitution,” *J. Phys. Chem. C*, vol. 122, no. 44, pp. 25565–25572, 2018.

[10] M. Xu, T. Liang, M. Shi, and H. Chen, “Graphene-Like Two-Dimensional Materials,” *Chem. Rev.*, vol. 113, no. 5, pp. 3766–3798, 2013.

[11] P. Sutter, J. Lahiri, P. Zahl, B. Wang, and E. Sutter, “Scalable Synthesis of Uniform Few-Layer Hexagonal Boron Nitride Dielectric Films,” *Nano Lett.*, vol. 13, no. 1, pp. 276–281, 2013.

[12] D. Kong *et al.*, “Synthesis of MoS_2 and $MoSe_2$ Films with Vertically Aligned Layers,” *Nano Lett.*, vol. 13, no. 3, pp. 1341–1347, 2013.

[13] M. Chyasnavichyus *et al.*, “Size-effect in layered ferrielectric CuInP2S6,” *Appl. Phys. Lett.*, vol. 109, no. 17, p. 172901, 2016.

[14] A. Dziaugys, J. Banys, J. Macutkevic, R. Sobiestianskas, and Y. Vysochanskii, “Dipolar glass phase in ferrielectrics: $CuInP_2S_6$ and $Ag_{0.1}Cu_{0.9}InP_2S_6$ crystals,” *Phys. Status Solidi A*, vol. 207, no. 8, pp. 1960–1967, 2010.

[15] A. Belianinov *et al.*, “$CuInP_2S_6$ Room Temperature Layered Ferroelectric,” *Nano Lett.*, vol. 15, no. 6, pp. 3808–3814, 2015.

[16] J. Guyonnet, *Ferroelectric Domain Walls*. Springer, 2014.

[17] A. K. Tagantsev, L. E. Cross, and J. Fousek, *Domains in Ferroic Crystals and Thin Films*. New York, NY: Springer New York, 2010.

[18] D. Damjanovic, “Hysteresis in Piezoelectric and Ferroelectric Materials,” in *The Science of Hysteresis*, vol. 3, I. Mayergoyz and G. Bertotti, Eds. Elsevier, 2005, pp. 337–465.

[19] L. Jin, F. Li, and S. Zhang, “Decoding the Fingerprint of Ferroelectric Loops: Comprehension of the Material Properties and Structures,” *J. Am. Ceram. Soc.*, vol. 97, no. 1, pp. 1–27, 2014.

[20] L. Corbellini, J. Plathier, C. Lacroix, C. Harnagea, D. Ménard, and A. Pignolet, “Hysteresis loops revisited: An efficient method to analyze ferroic materials,” *J. Appl. Phys.*, vol. 120, no. 12, p. 124101, Sep. 2016.

[21] D. Damjanovic, “Ferroelectric, dielectric and piezoelectric properties of ferroelectric thin films and ceramics,” *Reports Prog. Phys.*, vol. 61, no. 9, pp. 1267–1324, 1998.

[22] J. Valasek, “Piezo-Electric and Allied Phenomena in Rochelle Salt,” *Phys. Rev.*, vol. 17, no. 4, pp. 475–481, Apr. 1921.

[23] A. von Hippel, R. G. Breckenridge, F. G. Chesley, and L. Tisza, “High dielectric constant ceramics,” *Ind. Eng. Chem.*, vol. 38, no. 11, pp. 1097–1109, 1946.

[24] M. Lines and A. Glass, *Principles and Applications of Ferroelectrics and Related Materials*. New York: Oxford University Press, 1977.

[25] R. W. Whatmore, “Piezoelectric and Pyroelectric Materials and Their Applications,” in *Electronic Materials*, Boston, MA: Springer US, 1991, pp. 283–290.

[26] P. Sharma *et al.*, “Nonvolatile ferroelectric domain wall memory,” *Sci. Adv.*, vol. 3, no. 6, p. e1700512, Jun. 2017.

[27] T. Eshita, T. Tamura, and Y. Arimoto, “Ferroelectric random access memory (FRAM) devices,” in *Advances in Non-Volatile Memory and Storage Technology*, Woodhead Publishing, 2014, pp. 434–454.

[28] J. F. Scott, “Ferroelectrics go bananas,” *J. Phys. Condens. Matter*, vol. 20, no. 2, p. 021001, Jan. 2008.

[29] M. Maglione and M. A. Subramanian, “Dielectric and polarization experiments in high loss dielectrics: A word of caution,” *Appl. Phys. Lett.*, vol. 93, no. 3, p. 032902, 2008.

[30] B. Kim, D. Seol, S. Lee, H. N. Lee, and Y. Kim, “Ferroelectric-like hysteresis loop originated from non-ferroelectric effects,” *Appl. Phys. Lett.*, vol. 109, no. 10, p. 102901, 2016.

[31] B. Xu, C. Paillard, B. Dkhil, and L. Bellaiche, “Pinched hysteresis loop in defect-free ferroelectric materials,” *Phys. Rev. B*, vol. 94, no. 14, p. 140101, 2016.

[32] K. M. Rabe, “Antiferroelectricity in Oxides: A Reexamination,” in *Functional Metal Oxides*, Weinheim, Germany: Wiley-VCH Verlag GmbH & Co. KGaA, 2013, pp. 221–244.

[33] P. Tolédano and M. Guennou, “Theory of antiferroelectric phase transitions,” *Phys. Rev. B*, vol. 94, no. 1, p. 014107, 2016.

[34] B. A. Strukov and A. P. Levanyuk, “Ferroelectric Phenomena in Crystals,” 1998.

[35] T. Rojac, S. Drnovsek, A. Bencan, B. Malic, and D. Damjanovic, “Role of charged defects on the electrical and electromechanical properties of rhombohedral Pb(Zr , Ti)O_3 with oxygen octahedra tilts,” *Phys. Rev. B*, vol. 93, no. 1, p. 014102, 2016.

[36] W. J. Merz, “Double Hysteresis Loop of $BaTiO_3$ at the Curie Point,” *Phys. Rev.*, vol. 91, no. 3, pp. 513–517, 1953.

[37] S. Yun, “Double Hysteresis Loop in $BaTiO_3$-Based Ferroelectric Ceramics,” in *Ferroelectrics - Characterization and Modeling*, Dr. Mikael Lallart, Ed. InTech, 2011, pp. 245–264.

[38] Y. A. Genenko, J. Glaum, and M. J. Hoffmann, “Mechanisms of aging and fatigue in ferroelectrics,” *Mater. Sci. Eng. B*, vol. 192, pp. 52–82, 2015.

[39] K. Carl and K. H. Hardtl, “Electrical after-effects in Pb(Ti, Zr)O_3 ceramics,” *Ferroelectrics*, vol. 17, no. 1, pp. 473–486, 1977.

[40] R. A. Cowley, S. N. Gvasaliya, S. G. Lushnikov, B. Roessli, and G. M. Rotaru, “Relaxing with relaxors: a review of relaxor ferroelectrics,” *Adv. Phys.*, vol. 60, no. 2, pp. 229–327, 2011.

[41] J. Y. Fu, “On the Landau theory of phase transitions: a hierarchical dynamic model,” *J. Phys. Condens. Matter*, vol. 25, no. 7, p. 075903, 2013.

[42] R. A. Cowley, “Structural phase transitions I. Landau theory,” *Adv. Phys.*, vol. 29, no. 1, pp. 1–110, 1980.

[43] P. C. Hohenberg and A. P. Krekhov, “An introduction to the Ginzburg-Landau theory of phase transitions and nonequilibrium patterns,” *Phys. Rep.*, vol. 572, pp. 1–42, 2015.

[44] A. Saxena, “Broken symmetry, ferroic phase transitions and multifunctional materials,” *Integr. Ferroelectr.*, vol. 131, no. 1, pp. 3–24, 2011.

[45] J. Honig and J. Spałek, “The Landau Theory of Phase Transitions: General Concept and Its Microscopic Relation to Mean Field Theory,” in *A Primer to the Theory of Critical Phenomena*, Elsevier Science, 2017, pp. 55–85.

[46] L. Landau, “On the theory of phase transitions (translated and reprinted),” *Ukr. J. Phys.*, vol. 53, no. Special Issue, pp. 25–35, 2008.

[47] H. Schmid, “Some symmetry aspects of ferroics and single phase multiferroics,” *J. Phys. Condens. Matter*, vol. 20, no. 43, p. 434201, 2008.

[48] V. Fridkin and S. Ducharme, *The ferroelectricity at the nanoscale. Basics and Applications*. Springer-Verlag Berlin heidelberg, 2014.

[49] H. E. Stanley, Introduction to Phase Transitions and Critical Phenomena. Oxford University Press, 1971.

[50] R. Folk, “Multicritical behavior in ferroelectrics,” *Phase Transitions*, vol. 67, no. 4, pp. 645–666, 1999.

[51] R. Nitsche and P. Wild, “Crystal growth of metal-phosphorous-sulfur compounds by vapor transport,” *Mater. Res. Bull.*, vol. 5, no. 5, pp. 419–424, 1970.

[52] G. Dittmar and H. Schaffer, “The Crystal Structure of $Sn_2P_2S_6$,” *Z. Naturforsch*, vol. 29b, pp. 312–317, 1974.

[53] B. Scott, M. Pressprich, R. D. Willet, and D. A. Cleary, “High temperature crystal structure and DSC of $Sn_2P_2S_6$,” *J. Solid State Chem.*, vol. 96, no. 2, pp. 294–300, 1992.

[54] K. Kuepper *et al.*, "Electronic structure of $Sn_2P_2S_6$," *Phys. Rev. B*, vol. 67, no. 11, p. 115101, 2003.

[55] S. W. H. Eijt, R. Currat, J. E. Lorenzo, P. Saint-Grégoire, B. Hennion, and Y. M. Vysochanskii, "Soft modes and phonon interactions in $Sn_2P_2S_6$ studied by neutron scattering," *Eur. Phys. J. B*, vol. 5, no. 2, pp. 169–178, 1998.

[56] K. Moriya, H. Kuniyoshi, K. Tashita, Y. Ozaki, S. Yano, and T. Matsuo, "Ferroelectric Phase Transitions in $Sn_2P_2S_6$ and $Sn_2P_2Se_6$ Crystals," *J. Phys. Soc. Japan*, vol. 67, no. 10, pp. 3505–3511, 1998.

[57] K. Glukhov *et al.*, "Electronic Structure and Phase Transition in Ferroelectic $Sn_2P_2S_6$ Crystal," *Int. J. Mol. Sci.*, vol. 13, no. 12, pp. 14356–14384, 2012.

[58] Y. Voroshilov, M. Potorii, L. Seikovskaya, A. Yatsenko, and I. Prits, "Crystal Structure of $Sn_2P_2Se_6$," *Kristallografiya*, vol. 33, no. 5, pp. 1282–1283, 1988.

[59] R. Israël *et al.*, "Crystal structures of di-tin-hexa(seleno)hypodiphosphate, $Sn_2P_2Se_6$, in the ferroelectric and paraelectric phase," *Zeitschrift für Krist. - Cryst. Mater.*, vol. 213, no. 1, pp. 34–41, 1998.

[60] R. Enjalbert, J. Galy, Y. M. Vysochanskii, A. Ouedraogo, and P. Saint-Gregoire, "Structural study of the ferroelectric instability in $Sn_2P_2Se_6$," *Eur. Phys. J. B*, vol. 5, pp. 169–177, 1999.

[61] T. K. Barsamian, S. S. Khasanov, V. S. Shekhtman, Y. M. Vysochanskii, and V. Y. Slivka, "Incommensurate phase in proper ferroelectric $Sn_2P_2Se_6$," *Ferroelectrics*, vol. 67, no. 1, pp. 47–54, 1986.

[62] R. Caracas and X. Gonze, "First-principles study of $Sn_2P_2Se_6$ ferroelectrics," *Phys. Rev. B*, vol. 66, no. 10, pp. 1041061–1041067, 2002.

[63] R. Becker and W. Brockner, "Crystal Structure and Vibrational Spectra of $Pb_2P_2S_6$," *Z. Naturforsch*, vol. 38, no. 8, pp. 874–879, 1983.

[64] Y. Vysochanskii *et al.*, *Phase Transitions in Ferroelectric Phosphorous Chalcogenide Crystals*. Vilnius: Vilnius University Publishing House, 2008.

[65] K. Z. Rushchanskii *et al.*, “Ferroelectricity in $(Pb_ySn_{1-y})_2P_2S_6$ mixed crystals and random field BEG model,” *Phys. Status Solidi B*, vol. 253, no. 2, pp. 384–391, 2016.

[66] C. Hadenfeldt and D. Hoedel, “Kristallstruktur und Eigenschaften von Calcium- und Strontiumhexathiodiphosphat(IV), $Ca_2P_2S_6$ und $Sr_2P_2S_6$, mit einem Beitrag zu Ca_5P_8 und $Pb_2P_2S_6$,” *Zeitschrift für Anorg. und Allg. Chemie*, vol. 622, no. 9, pp. 1495–1500, 1996.

[67] G. H. F. Van Raaij, A. N. Rubtsov, and T. Janssen, “On a lattice model for type II incommensurate crystals,” *Ferroelectrics*, vol. 240, no. 1, pp. 1429–1433, 2000.

[68] I. Martynyuk-Lototska, O. Mys, B. Zapeka, A. Grabar, and R. Vlokh, “Acoustic wave velocities and elastic properties of $Sn_2P_2(Se_{0.28}S_{0.72})_6$ solid solutions,” *Philos. Mag.*, vol. 90, no. 33, pp. 4349–4359, 2010.

[69] O. Mys, I. Martynyuk-Lototska, B. Zapeka, and R. Vlokh, “On the special points on the (P, T, x)-phase diagram for $Sn_2P_2(Se_xS_{1-x})_6$ crystals: acoustic studies of $Sn_2P2(Se_{0.28}S_{0.72})_6$,” *Philos. Mag.*, vol. 93, no. 6, pp. 648–660, 2013.

[70] Y. Shapira, “The evidence for a Lifshitz point in MnP (invited),” *J. Appl. Phys.*, vol. 53, no. 3, pp. 1914–1919, 1982.

[71] A. V. Gomonnai, A. A. Grabar, and Y. M. Vysochanskii, “The splitting of the phase transition in the ferroelectric solid solutions,” *Fiz. Tverd. Tela*, vol. 23, no. 12, pp. 3602–3606, 1981.

[72] K. Z. Rushchanskii, Y. M. Vysochanskii, and D. Strauch, “Ferroelectricity, Nonlinear Dynamics, and Relaxation Effects in Monoclinic $Sn_2P_2S_6$,” *Phys. Rev. Lett.*, vol. 99, no. 20, p. 207601, 2007.

[73] A. Oleaga, V. Liubachko, A. Salazar, and Y. Vysochanskii, “Inducing a tricritical point in $Sn_2P_2(Se_yS_{1-y})_6$ ferroelectrics by Pb addition,” *Thermochim. Acta*, vol. 675, pp. 38–43, 2019.

[74] R. Yevych, M. Medulych, and Y. Vysochanskii, “Nonlinear dynamics of ferroelectrics with three-well local potential,” *Condens. Matter Phys.*, vol. 21, no. 2, p. 23001, 2018.

[75] R. Yevych and Y. Vysochanskii, “Description of lattice anharmonicity observed in ferroelectrics with unusual three-well local potential,” *Condens. Matter Phys.*, vol. 21, no. 3, p. 33001, 2018.

[76] Y. M. Vysochanskii, A. A. Kohutych, A. V. Kityk, A. V. Zadorozhna, M. M. Khoma, and A. A. Grabar, “Tricritical Behavior of $Sn_2P_2S_6$ Ferroelectrics at Hydrostatic Pressure,” *Ferroelectrics*, vol. 399, no. 1, pp. 83–88, 2010.

[77] M. Maior, S. Molnar, V. Vrabel, M. Gurzan, S. Motrja, and Y. M. Vysochanskii, “Diffusion phase transitions in $(Pb_ySn_{1-y})_2P_2(Se_xS_{1-x})_6$ solid solutions,” *Condens. Matter Phys.*, vol. 6, pp. 301–306, 2003.

[78] Vysochanskii and Drobnich, “The phase transition character and microscopic models for $Sn_2P_2S(Se)_6$ ferroelectrics,” *Condens. Matter Phys.*, vol. 5, pp. 669–683, 2002.

[79] K. Z. Rushchanskii *et al.*, “Observation of nonequilibrium behavior near the Lifshitz point in ferroelectrics with incommensurate phase,” *Phys. Rev. B*, vol. 93, no. 1, p. 014101, 2016.

[80] T. W. B. Kibble and G. E. Volovik, “On phase ordering behind the propagating front of a second-order transition,” *J. Exp. Theor. Phys. Lett.*, vol. 65, no. 1, pp. 102–107, Jan. 1997.

[81] A. del Campo, T. W. B. Kibble, and W. H. Zurek, “Causality and non-equilibrium second-order phase transitions in inhomogeneous systems,” *J. Phys. Condens. Matter*, vol. 25, no. 40, p. 404210, 2013.

[82] Y. M. Vysochanskii *et al.*, “Concentration dependencies of temperatures and character of phase transitions in $(Pb_ySn_{1-y})_2P_2S_6$ and $(Pb_ySn_{1-y})_2P_2Se_6$,” *Fiz. Tverd. Tela*, vol. 27, pp. 858–864, 1984.

[83] Y. Moriya, K., Iwauchi, K., Ushida, M., Nakagawa, A., Watanabe, K., Yano, S., Motojima, S., Akagi, “Dielectric studies of $Pb_xSn_{2(1-x)}P_2S_6$ ” *J. Phys. Soc. Japan*, vol. 64, no. 5, pp. 1775–1784, 1995.

[84] V. Shvalya, A. Oleaga, A. Salazar, A. A. Kohutych, and Y. M. Vysochanskii, “Critical behaviour study of ferroelectric semiconductors $(Pb_xSn_{1-x})_2P_2S_6$ from thermal diffusivity measurements,” *Thermochim. Acta*, vol. 617, pp. 136–143, 2015.

[85] R. Bilanych, R. Yevych, A. Kohutych, S. Perechinskii, I. Stoika, and Y. Vysochanskii, “Elastic properties of $(Pb_ySn_{1-y})_2P_2S_6$ solid solutions,” *Open Phys.*, vol. 12, no. 9, pp. 611–614, 2014.

[86] R. Yevych *et al.*, “Valence fluctuations in $Sn(Pb)_2P_2S_6$ ferroelectrics,” *Low Temp. Phys.*, vol. 42, no. 12, pp. 1155–1162, 2016.

[87] P. Ondrejkovic, M. Guennou, M. Kempa, Y. Vysochanskii, G. Garbarino, and J. Hlinka, “An x-ray scattering study of $Sn_2P_2S_6$:

absence of incommensurate phase up to 1 GPa," *J. Phys. Condens. Matter*, vol. 25, no. 11, p. 115901, Mar. 2013.

[88] B. K. Jones, "Low-frequency noise spectroscopy," *IEEE Trans. Electron Devices*, vol. 41, no. 11, pp. 2188–2197, 1994.

[89] L. K. J. Vandamme, "Noise as a diagnostic tool for quality and reliability of electronic devices," *IEEE Trans. Electron Devices*, vol. 41, no. 11, pp. 2176–2187, 1994.

[90] A. van der Ziel and E. R. Chenette, "Noise in Solid State Devices," *Adv. Electron. Electron Phys.*, vol. 46, pp. 313–383, 1978.

[91] A. K. Raychaudhuri, "Measurement of 1/*f* noise and its application in materials science," *Curr. Opin. Solid State Mater. Sci.*, vol. 6, no. 1, pp. 67–85, 2002.

[92] H. Wong, "Low-frequency noise study in electron devices: review and update," *Microelectron. Reliab.*, vol. 43, no. 4, pp. 585–599, 2003.

[93] A. A. Balandin, "Low-frequency 1/*f* noise in graphene devices.," *Nat. Nanotechnol.*, vol. 8, no. 8, pp. 549–55, 2013.

[94] E. Burstein and A. L. McWhorter, *Semiconductor Surface Physics*. Philadelphia: University of Pennsylvania press, 1957.

[95] D. J. Bergman and D. Stroud, "Physical Properties of Macroscopically Inhomogeneous Media," *Solid State Phys.*, vol. 46, pp. 147–269, Jan. 1992.

[96] Y. M. Lin and P. Avouris, "Strong Suppression of Electrical Noise in Bilayer Graphene Nanodevices," *Nano Lett.*, vol. 8, no. 8, pp. 2119–2125, 2008.

[97] A. N. Pal and A. Ghosh, "Resistance Noise in Electrically Biased Bilayer Graphene," *Phys. Rev. Lett.*, vol. 102, no. 12, p. 126805, Mar. 2009.

[98] X. Xie *et al.*, "Low-Frequency Noise in Bilayer MoS_2 Transistor," *ACS Nano*, vol. 8, no. 6, pp. 5633–5640, 2014.

[99] J. Banys *et al.*, "Investigation of Dielectric and Noise Properties of the Multiferoic Composite $BaTiO_3$ with $CoFe_2O_4$," *Ferroelectrics*, vol. 417, no. 1, pp. 25–32, 2011.

[100] S. A. Gridnev, A. N. Tsotsorin, and A. V. Kalgin, "Low-frequency 1/*f* noise in relaxor ferroelectric PMN–PZT," *Phys. Status Solidi*, vol. 245, no. 1, pp. 224–226, 2008.

[101] S. Pralgauskaite *et al.*, "Low frequency noise characteristics of $BaTiO_3$-$NiFe_2O_4$ composites at phase transition," in *2015 International Conference on Noise and Fluctuations (ICNF)*, 2015, pp. 1–4.

[102] A. Lisauskas, "Electrical Noise in Colossal Magnetoresistors and Ferroelectrics," Royal Institute of Technology, 2001.

[103] I. Muševič, A. Kityk, M. Škarabot, and R. Blinc, "Polarization Noise in a Ferroelectric Liquid Crystal," *Phys. Rev. Lett.*, vol. 79, no. 6, pp. 1062–1065, 1997.

[104] G. Careri, G. Consolini, Z. Kutnjak, C. Filipič, and A. Levstik, "1 / *f* noise and dynamical heterogeneity in glasses," *Phys. Rev. E*, vol. 64, no. 5, p. 052901, 2001.

[105] C. Carpentier and R. Nitsche, "Ferroelectricity in $Sn_2P_2S_6$," *Mater. Res. Bull.*, vol. 9, no. 8, pp. 1097–1100, 1974.

[106] M. Fabrizio, A. O. Gogolin, and A. A. Nersesyan, "From Band Insulator to Mott Insulator in One Dimension," *Phys. Rev. Lett.*, vol. 83, no. 10, pp. 2014–2017, 1999.

[107] W. Selke, "The ANNNI model — Theoretical analysis and experimental application," *Phys. Rep.*, vol. 170, no. 4, pp. 213–264, 1988.

[108] V. Samulionis, J. Banys, J. Macutkevic, and Y. Vysochanskii, "Ultrasonic Behavior Near Phase Transitions in $(Pb_ySn_{1-y})_2P_2S_6$ Ferroelectric Materials," *Ferroelectrics*, vol. 462, no. 1, pp. 87–96, 2014.

[109] V. S. Shusta, E. I. Gerzanich, A. G. Slivka, P. P. Guranich, and V. A. Bobela, "Phase transitions and physical properties of $(Pb_ySn_{1-y})_2P_2S_6$ crystals at high hydrostatic pressures," *Ferroelectrics*, vol. 145, no. 1, pp. 61–71, 1993.

[110] A. Oleaga, A. Salazar, A. Kohutych, and Y. M. Vysochanskii, "Critical behavior near the Lifshitz point in $Sn_2P_2(S_{(1-x)}Se_x)_6$ ferroelectric semiconductors from thermal diffusivity measurements.," *J. Phys. Condens. Matter*, vol. 23, no. 2, p. 025902, 2011.

[111] M. Maior, M. Gurzan, S. Molnar, I. Prits, and Y. Vysochanskii, "Effect of germanium doping on pyroelectric and piezoelectric properties of $Sn_2P_2S_6$ single crystal," *IEEE Trans. Ultrason. Ferroelectr. Freq. Control*, vol. 47, no. 4, pp. 877–80, 2000.

[112] K. A. Müller and H. Burkard, "$SrTiO_3$: an intrinsic quantum paraelectric below 4 K," *Phys. Rev. B*, vol. 19, no. 7, pp. 3593–3602, 1979.

[113] T. Wei, C. Zhu, K. F. Wang, H. L. Cai, J. S. Zhu, and J. M. Liu, "Influence of A-site codoping on ferroelectricity of quantum paraelectric $SrTiO_3$," *J. Appl. Phys.*, vol. 103, no. 12, 2008.

[114] H. Fujishita, S. Kitazawa, M. Saito, R. Ishisaka, H. Okamoto, and T. Yamaguchi, "Quantum Paraelectric States in $SrTiO_3$ and $KTaO_3$: Barrett Model, Vendik Model, and Quantum Criticality," *J. Phys. Soc. Japan*, vol. 85, no. 7, p. 074703, 2016.

[115] C. W. Rischau *et al.*, "A ferroelectric quantum phase transition inside the superconducting dome of $Sr_{1-x}Ca_xTiO_{3-\delta}$," *Nat. Phys.*, vol. 13, no. 7, pp. 643–648, 2017.

[116] S. E. Rowley *et al.*, "Ferroelectric quantum criticality," *Nat. Phys.*, vol. 10, no. 5, pp. 367–372, 2014.

[117] C. L. Wang and M. L. Zhao, "Burns temperature and quantum temperature scale," *J. Adv. Dielectr.*, vol. 1, no. 2, pp. 163–167, 2011.

[118] N. Barman, P. Singh, C. Narayana, and K. B. R. Varma, "Incipient ferroelectric to a possible ferroelectric transition in Te 4+ doped calcium copper titanate ($CaCu_3Ti_4O_{12}$) ceramics at low temperature as evidenced by Raman and dielectric spectroscopy," *AIP Adv.*, vol. 7, no. 3, p. 035105, 2017.

[119] V. S. Vikhnin, P. A. Markovin, and W. Kleemann, "The origin of polar ordering in incipient ferroelectrics with weak off-center impurities," *Ferroelectrics*, vol. 218, no. 1, pp. 85–91, 1998.

[120] P. Barone, D. Di Sante, and S. Picozzi, "Improper origin of polar displacements at $CaTiO_3$ and $CaMnO_3$ twin walls," *Phys. Rev. B*, vol. 89, no. 14, p. 144104, 2014.

[121] K. Moriya, N. Kariya, A. Inaba, T. Matsuo, I. Pritz, and Y. Vysochanskii, "Low-temperature calorimetric study of phase transitions in $CuCrP_2S_6$," *Solid State Commun.*, vol. 136, no. 3, pp. 173–176, 2005.

[122] I. Studenyak, O. Mykajlo, Y. Vysochanskii, and V. Cajipe, "Optical absorption studies of phase transitions in $CuCrP_2S_6$ layered antiferroelectrics," *J. Phys. Condens. Matter*, vol. 15, no. 40, pp. 6773–6779, 2003.

[123] R. H. Lyddane, R. G. Sachs, and E. Teller, “On the Polar Vibrations of Alkali Halides,” *Phys. Rev.*, vol. 59, no. 8, pp. 673–676, Apr. 1941.

[124] A. Dziaugys, “Influence of impurities on dielectric properties of ferroelectric and superionic crystals,” Vilnius University, 2011.

[125] V. Maisonneuve, J. Reau, M. Dong, V. Cajipe, C. Payen, and J. Ravez, “Ionic conductivity in ferroic $CuInP_2S_6$ and $CuCrP_2S_6$,” *Ferroelectrics*, vol. 196, no. 1, pp. 257–260, 1997.

[126] A. Dziaugys, J. Banys, J. Macutkevic, and Y. Vysochanskii, “Conductivity Spectroscopy of New $AgInP_2S_6$ Cystals,” *Integr. Ferroelectr.*, 2010.

[127] V. Maisonneuve, M. Evain, C. Payen, V. B. Cajipe, and P. Molinié, “Room-temperature crystal structure of the layered phase $Cu^{II}n^{III}P_2S_6$,” *J. Alloys Compd.*, vol. 218, no. 2, pp. 157–164, 1995.

[128] M. A. Susner, M. Chyasnavichyus, M. A. McGuire, P. Ganesh, and P. Maksymovych, “Metal Thio- and Selenophosphates as Multifunctional van der Waals Layered Materials,” *Adv. Mater.*, vol. 29, no. 38, p. 1602852, 2017.

[129] I. Studenyak *et al.*, “Disordering effect on optical absorption processes in $CuInP_2S_6$ layered ferrielectrics,” *Phys. Status Solidi B*, vol. 236, no. 3, pp. 678–686, 2003.

SANTRAUKA LIETUVIŲ KALBA

ĮVADAS

Pastaraisiais dešimtmečiais daugiausiai tyrinėtos feroelektrinės medžiagos bario titanatas ($BaTiO_3$), švino titanatas ($PbTiO_3$) ir švino cirkonio titanatas (PZT) jau yra sėkmingai komercializuotos ir dominuoja rinkoje. Palyginti su jomis, feroelektriniai fosforo chalkogenidų kristalai atrodo gana egzotiškomis medžiagomis. Šioje disertacijoje tirta fosforo chalkogenidų kristalų šeima gali būti suskirstyta į dvi medžiagų grupes. Pirmoji aprašoma chemine formule $M_2P_2X_6$ (kur M – pereinamųjų žemių metalai, X – chalkogenidų atomai). Šie junginiai taip pat klasifikuojami kaip chalkogenohipodifosfatai. Sėkmingai sintezuoti ir charakterizuoti tiofosfatai $Sn_2P_2S(Se)_6$ ir $Pb_2P_2S(Se)_6$ yra izostruktūriniai analogai galintys sudaryti kietuosius tirpalus įvairiomis koncentracijomis. $(Pb_ySn_{1-y})_2P_2(Se_xS_{1-x})_6$ sistemos kristalams būdinga sudėtinga žemos simetrijos trimatė kristalinį gardelė. Antroji kristalų grupė aprašoma chemine formule $M^IM^{III}P_2X_6$ (M^I, M^{III} – pereinamųjų metalų elementai, X – chalkogenidai) pasižymi sluoksnine struktūra su van der Waals tarpais tarp sluoksnių. Nemažai sluoksniuotų feroelektrinių fosforo chalkogenid kristalų buto tyrinėta iki šiol, tačiau paskutiniu laiku jie susilaukė naujo vis didėjančio tyrėjų susidomėjimo.

Be abejo, pastaruoju metu augantis susidomėjimas minėtais kristalais susijęs ne tik su struktūriniais aspektais, tačiau ir dėl fundamentinių ir taikomųjų fizinių bei cheminių savybių įvairovės. $Sn_2P_2S_6$ kristalai yra žinomiausias feroelektrinio trinario fosforo chalkogenido pavyzdys. Optiniais metodais nustatyta, kad $Sn_2P_2S_6$ pasižymi ir puslaidininkinėmis bei perspektyviomis fotorefraktinėmis, fotovoltainėmis bei elektrooptinėmis savybėmis. Šiame darbe tirtos nominaliai gryno $Sn_2P_2S_6$kristalo feroelektrinės savybės. Taip pat tiriama įvarių priemaišų ir dėl jų atsirandančių kristalinės gardelės defektų įtaka kristalų dielektrinėms, elektrinėms ir feroelektrinėms savybėms.

Panaudojus lipnią juostą atskirti anglies atomo storio sluoksnelius nuo grafito gabalo buvo sukurta pirmoji dvimatė (2D) vieno atomo storio medžiaga - grafenas. Vieno atomo sluoksnio plėvelės pasižymi naujomis savybėmis, kurios nėra būdingos tūriniam kristalui, todėl dvimatė (2D) sluoksninių medžiagų įvairovė didėja iki šiol ir sulaukia vis didesnio susidomėjimo. Pastaruoju metu, plačiausiai tiriamos sluoksninės 2D medžiagos yra heksagoninis boro nitridas ir pereinamųjų metalų dichalkogenidai, kurių geriausiai žinomas atstovas yra molibdeno disulfidas. Keturnariai fosforo chalkogenidų kristalai pasižymi sluoksnine struktūra su

silpnomis jungtimis tarp sluoksnių, todėl struktūriškai jie labai panašūs į anksčiau minėtas dvimates medžiagas, kurias galima izoliuoti iki atomo storio sluoksnelių. Atsižvelgiant į tai, kad keturnariai fosforo chalkogenidai yra puslaidininkiai ir feroikai, jie yra potencialūs kandidatai naujos kartos elektronikai. Ferielektrikas vario indžio tiofosfatas ($CuInP_2S_6$) yra plačiausiai žinomas šių medžiagų pavyzdys. Iki šiol šis tūrinis kristalas buvo puikiai charakterizuotas. Šioje disertacijoje triukšminės spektroskopijos metodas $CuInP_2S_6$ leido praplėsti žinias apie šią medžiagą ir suteikė papildomos informacijos apie procesus vykstančius ferielektrinio fazinio virsmo metu.

Disertacijos tikslas ir uždaviniai

Disertacijos tikslas – ištirti dielektrines, feroelektrines, piroelektrines ir triukšmines savybes susijusias su trinarių ir keturnarių fosforo chalkogenidų kristalų faziniais virsmais.

Tikslui įgyvendinti iškelti pagrindiniai darbo uždaviniai:

1. Ištirti $Sn_2P_2S_6$ kristaluose stebėtus feroelektrinius ir antiferoelektrinius nestabilumus ir palyginti jų dielektrines bei feroelektrines savybes;
2. Ištirti švino priemaišų įtaką $Sn_2P_2S_6$ kristalo dielektrinėms, piroelektrinėms ir feroelektrinėms savybėms, ištiriant švino priemaišų įtaką fazinei diagramai.
3. Ištirti nedidelio kiekio Ge priemaišų įtaką $(Pb_ySn_{1-y})_2P_2S_6$ kristalų dielektrinėms savybėms.
4. Nustatyti feroelektrinių kristalų makroskopinių savybių ir fliuktuacijų, vykstančių fazinio virsmo metu, ryšį triukšminės spektroskopijos metodu.

Mokslinis naujumas

• Dviguba antiferoelektrinio tipo histerezes kilpa stebima pirmą kartą Bridgman metodu užaugintama tūriniame feroelektriniame $Sn_2P_2S_6$ kristale. Dviguba histerezės kilpa feroelektriniame kristale yra neįprastas ir retas reiškinys. Išsamiai ištirtos ir analizuotos normalios feroelektrinės ir dvigubos antiferoelektrinio tipo histerezės kilpos realizavimo sąlygos $Sn_2P_2S_6$ kristale.

• Atlikta išsami $(Pb_ySn_{1-y})_2P_2S_6$ kietųjų tirpalų dielektrinių, piroelektrinių ir feroelektrinių savybių analizė ir susieta su fazinio virsmo metu stebėtomis savybėmis.

• Pirmą kartą išmatuota $Pb_2P_2S_6$, $(Pb_{0.98}Ge_{0.02})_2P_2S_6$, $(Pb_{0.7}Sn_{0.3})_2P_2S_6$+5%Ge and $(Pb_{0.7}Sn_{0.3})_2P_2Se_6$+5%Ge junginių dielektrinės skvarbos temperatūrinės priklausomybės (20-300 K).

• Pirmą kartą ištirtos ferielektrinio sluoksninio $CuInP_2S_6$ kristalo triukšminės savybės fazinio virsmo artumoje. Atliktas detalus ferielektrinio kristalo triukšmų charakteristikų modeliavimas. Gauti rezultatai rodo, kad triukšminė spektroskopija yra patikimas, jautrus ir nedestruktyvus metodas papildomam feroelektrinių medžiagų charakterizavimui.

Ginamieji teiginai

1. Neįprastas poliarizacijos persijungimo mechanizamas tūriniame tikrajame feroelektrike $Sn_2P_2S_6$ yra paaiškinamas anharmoninio kvantinio osciliatoriaus modeliu.
2. Dielektriniai, piroelektriniai ir feroelektriniai $(Pb_ySn_{1-y})_2P_2S_6$ mišrių kristalų matavimai įrodo dviejų fazių koegzistavimą, kai švino koncentracija viršija y>0,2.
3. Germanio priemaišos turi lemiamą įtaką $Pb_2P_2S_6$ kristalo kvantinei paraelektrinei būsenai.
4. Ferrielektriniuose kristaluose pastebimi staigūs žemadažnio triukšmo charakteristikų pokyčiai, rodantys struktūrinį fazinį virsmą.

Disertacijos sandara

Disertaciją sudaro penki skyriai ir cituojamos literatūros sąrašas. Cituojamos literatūros sąraše yra 129 nuorodos.

Pirmasis skyrius – įvadas, kuriame pristatoma disertacijos tema bei aktualumas, iškeliami darbo tikslai ir suformuluojami uždaviniai jiems įgyvendinti, taip pat pateikiami ginamieji teiginiai, publikacijų ir pranešimų konferencijose sąrašas.

Antrajame skyriuje yra apžvelgta literatūra disertacijos tema.

Trečiajame skyriuje pateikiama tyrimų metodika bei bandinių aprašymas.

Ketvirtajame skyriuje apžvelgiami tyrimų metu gauti rezultatai.

Penktajame skyriuje pateikiamos išvados.

TYRIMŲ METODIKA

Tirtos medžiagos

Disertacijoje tiriami fosforo chalkogenidų kristalai buvo užauginti garų transporto (disertacijoje ir santraukoje trumpinama – VT, angl. *vapor transport*) arba Bridgman (disertacijoje ir santraukoje trumpinama – Br) metodais.

Disertacijoje tirti žemiau nurodyti kristalai:

- o $Sn_2P_2S_6$ VT ir $Sn_2P_2S_6$ Br;
- o $Pb_2P_2S_6$ VT;
- o $(Pb_ySn_{1-y})_2P_2S_6$ (y = 0,1, 0,2 ir 0,3) VT;
- o $(Pb_{0,98}Ge_{0,02})_2P_2S_6$ VT;
- o $(Pb_{0,7}Sn_{0,3})_2P_2S(Se)_6$ VT;
- o $CuInP_2S_6$ VT;
- o $AgCrP_2S_6$ and $Cu_{0,2}Ag_{0,8}P_2S_6$ VT.

Matavimų metodai

Dielektrinė spektroskopija

Tiriamųjų kristalų kompleksinės dielektrinės skvarbos matavimai atlikti plačiame temperatūros (nuo 20 K iki 500 K) intervale. Žemuose dažniuose, nuo 20 Hz iki 1 MHz, buvo matuojama kondensatoriaus talpa ir nuostolių kampo tangentas, naudojant LCR matuoklį (Hewlett Packard 4284). Iš matavimo duomenų buvo apskaičiuotos menamoji ir realioji dielektrinės svarbos dedamosios.

Korektiškam matavimui atlikti reikalingas tam tikrų matmenų bandinys. Bandinio kontaktinės plokštumos nušlifuojamos ir padengiamos sidabro pasta, geresniam kontakto užtikrinimui.

Feroelektrinių ir piroelektrinių charakteristikų matavimas

Feroelektrinių ir piroelektrinių charakteristikų matavimams buvo naudojamas TF Analyzer 2000E (aixACCT Systems) analizatorius su TREK 609E-6 4 kV įtampos stiprintuvu. Visi bandiniai buvo patalpinti į alyvą, kad būtų galima išvengti elektrinės iškrovos. Bipolinis trikampio pavidalo įtampos signalas buvo naudojamas feroelektrinių kilpų ir piroelektrinio atsako indukcijai.

Triukšminė spektroskopija

Triukšmų tyrimas atliekamas gerai ekranuotoje patalpoje. Tiriamieji kristalai dar papildomai patalpinami į metalinę dėžę. Taip siekiama visą matavimo sistemą maksimaliai apsaugoti nuo išorinio elektromagnetinio lauko fono.

Elektriniai žemadažniai triukšmai buvo matuojami panaudojant National Instrument PCI 6115 analogas – kodas keitiklį. Triukšmai matuoti dažnių diapazone nuo 10 Hz iki 20 kHz.

Dielektrinės ir feroelektrinės $Sn_2P_2S_6$ kristalo savybės

Šiame poskyryje pateikti tyrimų rezultatai ir jų aptarimas, kurie atskleidžia dvigubos histerezės kilpos reiškinį $Sn_2P_2S_6$ (SPS) feroelektriniame kristale. Egzistuoja dvi skirtingos $Sn_2P_2S_6$ kristalų auginimo metodikos: Bridgman metodas (toliau vadinamas – $Sn_2P_2S_6$ Br) ir garų transporto metodas (toliau vadinamas – $Sn_2P_2S_6$ VT). Dielektriniams ir feroelektriniams tyrimams buvo naudoti $Sn_2P_2S_6$ kristalai išauginti abiem metodais. Rezultatų patikimumui ir atsikartojamumui užtikrinti buvo panaudota po du skirtingos auginimo serijos bandinius iš kiekvienos grupės.

$Sn_2P_2S_6$ yra feroelektrinis puslaidininkinis kristalas, priklausantis trinarių fosforo chalkogenidų $M_2P_2X_6$ (M – pereinamųjų metalų atomai, X – chalkogenas) kristalų šeimai. Kambario temperatūroje $Sn_2P_2S_6$ yra feroelektrinėje fazėje, aprašomas monoklinine erdvine grupe Pc. SPS kristale įvyksta antros rūšies fazinis 337 K temperatūroje į paraelektrinę fazę, aprašomą monoklinine erdvine grupe $P2_1/c$ [1].

1 pav. pateiktos $Sn_2P_2S_6$ Br kristalo poliarizacijos histerezės kilpos 243-347 K temperatūrų intervale. Kaip minėta anksčiau, SPS kristale struktūrinis fazinis virsmas įvyksta 337 K temperatūroje, tai patvirtina ir histerezės. Pateiktos SPS kristalo histerezės yra antiferoelektrinio tipo, nors literatūroje pateikti duomenys apie šio kristalo feroelektrinę prigimtį [2].

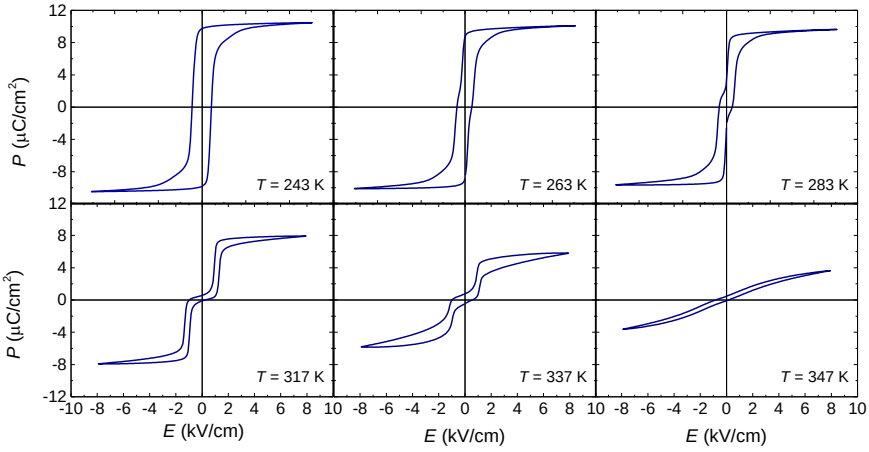

1 pav. Bridgman metodu užaugintų $Sn_2P_2S_6$ kristalų poliarizacijos histerezės kilpos skirtingose temperatūrose.

2 paveiksle pavaizduota realiosios ir menamosios dielektrinės skvarbos dalių priklausomybė nuo temperatūros $Sn_2P_2S_6$ Br kristaluose esant skirtingiems dažniams. Šių medžiagų dielektrinės skvarbos priklausomybės

nuo dažnio ir temperatūros buvo išmatuotas 20 Hz – 1 MHz dažnių ruože ir 100 K – 400 K temperatūrų intervale. Stebimos ryškios dielektrinės skvarbos anomalijos 337 K temperatūroje susijusios su struktūriniu faziniu virsmu. Dielektriniai nuostoliai kristale nėra dideli. Be to, dielektrinės skvarbos matavimai neparodė neįprastų anomalijų, leidžiančių indikuoti prastą kristalo kokybę.

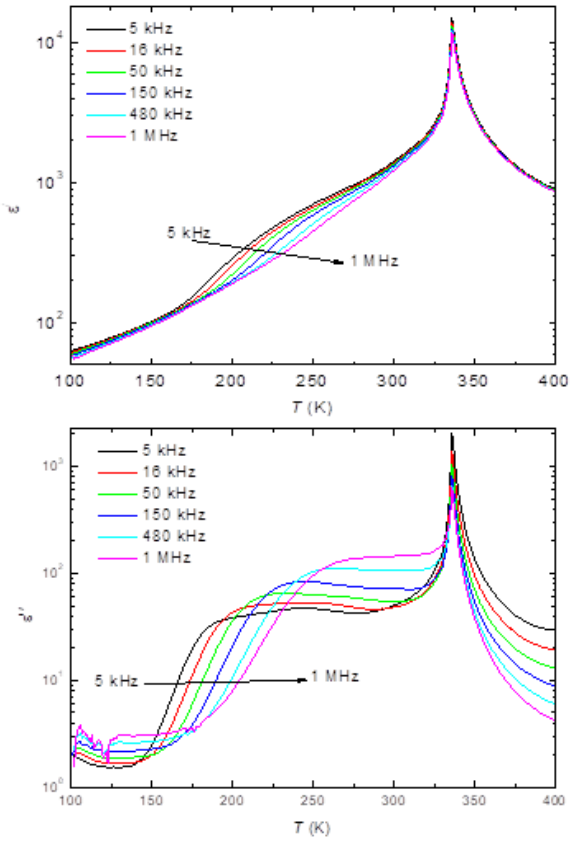

2 pav. $Sn_2P_2S_6$ Br kristalų dielektrinės skvarbos priklausomybė nuo temperatūros.

$Sn_2P_2S_6$ Br kristalą pakaitinus iki temperatūros aukštesnės nei kristalo Kiuri temperatūra (T_C=337 K) ir palaikius dvi valandas 373 K temperatūroje, antiferoelektrinio tipo histerezės pranyko. Visgi, kristalą palaikius kelias savaites kambario temperatūroje ir pakartojus feroelektrinius matavimus, gaunamos dvigubos antiferoelektrinio tipo kilpos. Šie dėsningumai kartojosi tarp skirtingų Bridgman metodu gamintų bandinių.

Ankstesnių tyrimų duomenimis, SPS kristalas būdinga feroelektrinė histerezės kilpa, ir nustatyta savaiminės poliarizacijos vertė lygi 14 μC/cm^2, o koercinis laukas lygus 0,75 kV/cm. Žinoma, kad SPS kristale savaiminė poliarizacija yra (010) plokštumoje, nukrypusi maždaug (14±2)º nuo $+x$ ašies. Minėtieji autoriai tyrė SPS kristalą, užauginta garų transporto metodu, tuo tarpu 1 ir 2 paveiksluose pateikti $Sn_2P_2S_6$ Br kristalo tyrimų rezultatai. Todėl papildomiems tyrimams buvo pasirinkti garų transporto metodu užauginti $Sn_2P_2S_6$ (toliau - $Sn_2P_2S_6$ VT) bandiniai. Pamatavus garų transporto metodu užauginto $Sn_2P_2S_6$ kristalo feroelektrines savybes, buvo stebėtos feroelektrinės histerezės kilpos (3 pav.)

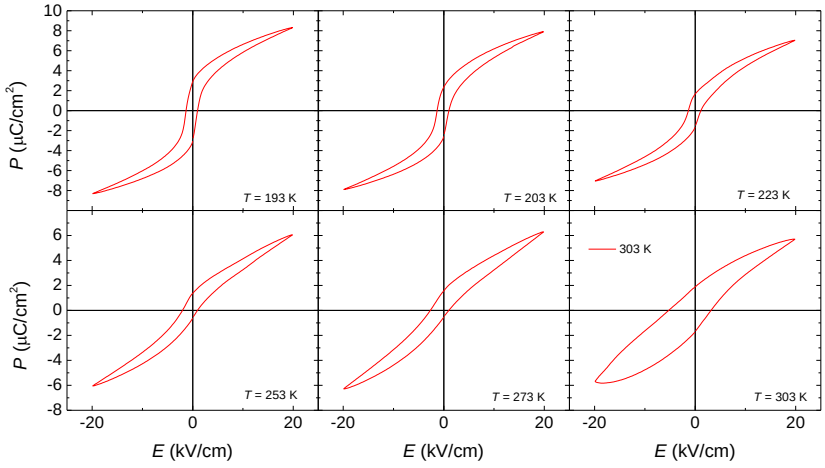

3 pav. Garų transporto metodu užaugintų $Sn_2P_2S_6$ kristalų poliarizacijos histerezės kilpos skirtingose temperatūrose.

Iš gautų histerezių matyti, $Sn_2P_2S_6$ VT kristalo poliarizacijos vertė apytiksliai lygi 10 μC/cm^2, ir tikrai nesiekia literatūroje nurodytos 14 μC/cm^2 vertės. Toks elgesys gali būti siejamas su pasireiškiančiu laidumo indėliu šiuose kristaluose. Pamatavus dielektrines savybes ir kristalo laidumą, patvirtinta iškelta hipotezė apie didesnį laidumo sandą $Sn_2P_2S_6$ VT nei $Sn_2P_2S_6$ Br kristaluose. Kadangi SPS kristalai yra puslaidininkiai, laidumo padidėjimas aiškintinas didesne defektų koncentracija. Dvigubos histerezės nestebimos ir kitose šios šeimos kristaluose $(Pb_ySn_{1-y})_2P_2S_6$ ir $Sn_2P_2(Se_xS_{1-x})_6$, kuriuose dėl atominių priemaišų kristalų defektų koncentracija taip pat padidėjusi. Spėjama, kad būtent defektai visuose šiuose kristaluose panaikina dvigubos histerezės kilpos realizacijos galimybę.

$Sn_2P_2S_6$ Br kristale stebėtas dvigubos kilpos gali būti paaiškintos remiantis anharmoninio kvantinio osciliatoriaus modeliu [3]. Osciliatoriaus modelis dažnai naudojamas fizikoje įvairių reiškinių paaiškinimui. Kvantinio

osciliatoriaus įvaizdis – tai mechaninės švytuoklės kvantinis analogas, kuris dažnai taikomas spektroskopijoje. Paprasčiausias modelis yra harmoninis kvantinis osciliatorius, kuriuo naudojantis galima aprašyti atomų virpesius diatomėje molekulėje. Tokio kvantmechaninio uždavinio sprendinius galima rasti daugelyje kvantinės fizikos vadovėlių. Anharmoninis kvantinis osciliatorius - tai bendresnis uždavinys, kurio sprendiniai priklauso nuo to, kokio pavidalo pasirinksime potencinės energijos priklausomybės nuo koordinatės funkciją.

$Sn_2P_2S_6$ kristalo fizikinių savybių aprašymui iki šiol buvo naudotas anharmoninio kvantinio osciliatoriaus modelis, kuriame kristalinė gardelė aprašoma vienmate vienodų sąveikaujančių anharmoninių osciliatorių grandinėle. Tokios sistemos Hamiltonianas aprašomas taip:

$$H = \sum_i (T(x_i) + V(x_i)) + \sum_{ij} J_{ij} x_i x_j \qquad (1)$$

čia $T(x_i)$ ir $V(x_i)$ atitinkamai yra kinetinės ir potencinės energijos operatoriai, x_i yra i-tojo osciliatoriaus koordinatė, J_{ij} yra i-tojo ir j-tojo osciliatorių sąveikos konstanta. Naudojantis vidutinio lauko artiniu ir įvedus vidutinį osciliatoriaus poslinkį, paskutinį (1) formulės narį galima pakeisti taip:

$$\sum_{ij} J_{ij} x_i x_j \approx \sum_i J_i \langle x \rangle x_i \qquad (2)$$

Įvedus šiuos pakeitimus, visos sistemos Hamiltoniaas gali būti užrašytas kaip nepriklausomų dalelių Hamiltonianų suma:

$$H = \sum_i H_i^{eff}, H_i^{eff} = T(x_i) + V(x_i) + J\langle x \rangle x_i \qquad (3)$$

Išsprendus Šriodingerio lygtį tokiai sistemai gaunami sprendiniai atitinkantys vidutinį osciliatoriaus poslinkį, kuris nagrinėjamu atveju yra proporcingas sistemos tvarkos parametrui.

$Sn_2P_2S_6$ kristalinė gardelė yra trimatė ir sudaryta iš dviejų formulinių vienetų, tačiau ji puikiai gali būti aprašyta dvejomis ekvivalenčiomis grandinėlėmis, kurios aprašomos (3) Hamiltonianu. Papildomai įvestas sąveikos operatorius J_2 aprašo sąveiką tarp šių dviejų grandinėlių (4 pav.) Ankstesniuose darbuose buvo parodyta, kad $Sn_2P_2S_6$ kristalinės gardelės potencinės energijos operatorius įgauna pavidalą, pavaizduotą 4 paveiksle. Trijų duobių pavidalo potencialas yra fenomenologiškai aprašytas ankstesniuose darbuose. Toks pavidalas aiškinamas netiesine $A_gB_u^2$ sąveika tarp žemadažnių optinių B_u simetrijos modų ir simetriškų A_g modų [3].

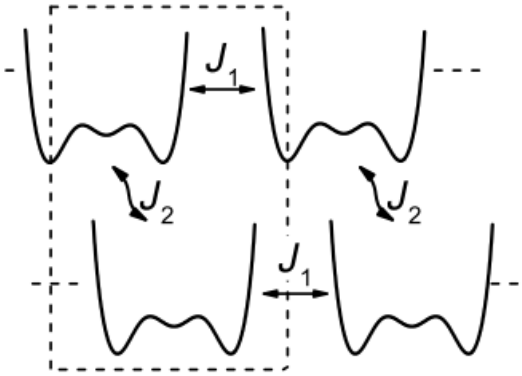

4 pav. Trijų duobių pavidalo potencialas naudojamas kvantinio anharmoninio osciliatoriaus modelyje $Sn_2P_2S_6$ kristalo aprašymui. Kvantinio anharmoninio osciliatoriaus modelis, kuriame dvi anharmoninių osciliatorių grandinėlės atitinka dvi subgardeles, sudarančias $Sn_2P_2S_6$ kristalo gardelę. Sąveiką subgardelėse aprašoma sąveikos operatoriumi J_1, o sąveika tarp subgardelių – sąveikos operatoriumi J_2.

Atkreiptinas dėmesys, kad kvantinio anharmoninio osciliatoriaus modelis puikiai paaiškinio eksperimentinius $Sn_2P_2S_6$ kristalo rezultatus, susijusius su *T-p* ir *T-y* fazine diagrama $(Pb_ySn_{1-y})_2P_2S_6$ mišrių kristalų šeimai [4]. Dvigubos kilpos atsiradimui $Sn_2P_2S_6$ tikrajame feroelektrike paaiškinti, gauti sprendiniai, kurie pavaizduoti 5 paveiksle.

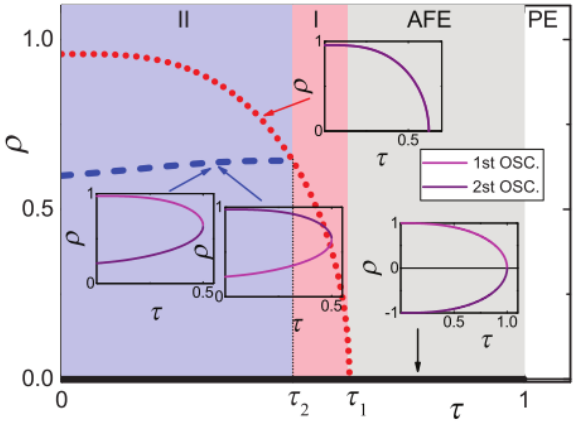

5 pav. $Sn_2P_2S_6$ kristalo redukuoto tvarkos parametro priklausomybė nuo redukuotos temperatūros.

Pateiktame 5 paveiksle galime išskirti keturias sritis, atitinkančius stabilius sprendinius aprašančius stabilias feroelektrinė (FE) ir

antiferoelektrines (AFE) fazes bei dvi sritis I ir II aprašančias metastabilius sprendinius, kuriuose matome kelių fazių koegistavimą. Šiame kristalo aprašyme įvedama redukuota temperatūra τ (čia $\tau = T/T_C$) ir redukuotas tvarkos parametras ρ (čia $\rho = P/P_0$, P_0 – vienos iš subgardelių poliarizacija nulinėj temperatūroj atitinkanti stabilų srendinį). Gauti sprendiniai patvirtina, kad $Sn_2P_2S_6$ kristale stebėta dviguba histerezės kilpa atsiranda dėl trigubo potencialo pavidalo, kuris nulemia FE ir AFE tvarkos koegzistavimą metastabiliose srityse.

Dielektrinės, piroelektrinės ir feroelektrinės $(Pb_ySn_{1-y})_2P_2S_6$ kietųjų tirpalų savybės

6 paveiksle pavaizduota realiosios ir menamosios atvirkštinės dielektrinės skvarbos dalių priklausomybės nuo temperatūros $(Pb_ySn_{1-y})_2P_2S_6$ kristaluose esant skirtingiems dažniams. Šių medžiagų dielektrinės skvarbos priklausomybės nuo dažnio ir temperatūros buvo išmatuotas 20 Hz – 1 MHz dažnių ruože ir 20 K – 350 K temperatūrų intervale. Įvedant švino priemaišų į SPS kristalą fazinio virsmo temperatūra slenka žemesnių temperatūrų link.

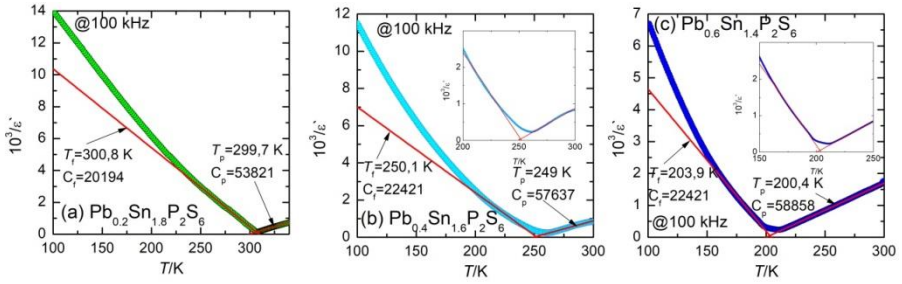

6 pav. $(Pb_ySn_{1-y})_2P_2S_6$ (y=0,1; 0,2; 0,3) kristalų atvirkštinės dielektrinės skvarbos realiosios ir menamosios dalių temperatūrinės priklausomybės

Aproksimuojant gautus rezultatus buvo apskaičiuotos Kiuri-Veiso konstantos ($C_{P,F}$) ir rastos Kiuri temperatūros T_C. $(Pb_{0,1}Sn_{0,9})_2P_2S_6$ kristalui gauti tokie parametrai: $C_F = 0{,}21\cdot10^5$ K; $C_P = 0{,}54\cdot10^5$ K; T_C = 299,4 K. Kiuri-Veiso konstantų santykis C_P/C_F=2,2. Pagal Landau teoriją, esant antros rūšies faziniam virsmui, Kiuri – Veiso konstantų santykis turi būti lygus 2. Kadangi apskaičiuotas santykis paklaidų ribose sutampa su teorine verte galima teigti, kad $(Pb_{0,1}Sn_{0,9})_2P_2S_6$ kristale stebimas antros rūšies feroelektrinis fazinis virsmas. Kaip matyti iš 6 pav. didėjant švino priemaišų koncentracijai tirtuosiuose kristaluose galima išskirti trečią vidurinę fazę. Iki šiol manyta, kad $(Pb_ySn_{1-y})_2P_2S_6$ (y<0,6) kristaluose vyksta paraelektrinis-feroelektrinis fazinis virsmas. Atsižvelgiant į tai, kad tirtuose kristaluose alavas keičiamas žymiai sunkesniais švino jonais, galima daryti prielaidą,

kad kristalinėje gardelėje atsiranda papildomi įtempimai. Todėl tikėtina, kad padidinus švino priemaišų koncentraciją arba išorinį slėgį galima tikėtis trikritinio taško fazinėje diagramoje.

Temperatūrų vertės gautos iš piroelektrinių matavimų gerai sutampa su Kiuri temperatūrų vertėmis gautomis iš dielektrinių matavimų. Tuo tarpu $(Pb_{0,2}Sn_{0,8})_2P_2S_6$ ir $(Pb_{0,3}Sn_{0,7})_2P_2S_6$ kristalų pirokoeficiento maksimumai nėra tokie „aštrūs“. Tokie rezultatai neblogai koreliuoja su duomenimis, gautais iš dielektrinių matavimų (6 pav.), kurie buvo aiškinami kelių fazių koegzitavimu SPS kristaluose su 20% ir 30% švino priemaišų. Gautos piroelektrinio koeficiento aproksimavimo parametrų vertės gerai sutampa su vertėmis, gautomis iš dielektrinių matavimų. Laipsnio rodiklis β visuose tirtuose kristaluose atitinkamai didinant švino koncentraciją yra: 0,47±0,002, 0,50±0,005 ir 0,53±0,059.

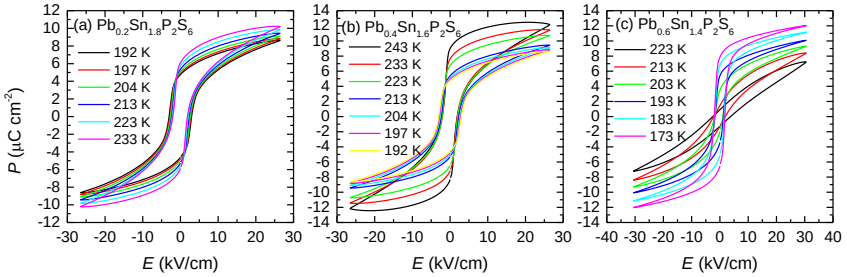

7 pav. $(Pb_ySn_{1-y})_2P_2S_6$ (y=0.1; 0.2 ir 0.3) poliarizacijos histerezės kilpos.

$CuInP_2S_6$ kristalo triukšminė spektroskopija

Triukšmų tyrimams buvo pasirinktas $CuInP_2S_6$ kristalas, kuris taip pat priskiriamas fosforo chalkogenidų šeimai. Šis kristalas sudarytas dviejų feroiškai aktyvių subgardelių, kurių dinamika 315 K temperatūroje sukelia pirmos rūšies fazinį virsmą. Simetrijos pažemėjimas ($C_2/c \rightarrow Cc$) atsiranda dėl vario jonų susitvarkymo ir indžio jonų poslinkio atitinkmose subgardelėse. Šis feroelektrinis kristalas taip pat turi puslaidininkių savybių [5].

Pagrindinės $CuInP_2S_6$ kristalo įtampos fliuktuacijų spektrinio tankio priklausomybė nuo temperatūros prie 128 Hz dažnio pateiktos 8 (a) pav. Kaip matyti iš 8 pav. nuo 310 K temperatūros stebimo triukšmo lygis padidėja, tačiau laikiniame signale (8 (b) pav.) stebima ta pati šiluminio triukšmo komponentė turinti „baltą“ spektrą. Fazinio virsmo temperatūros aplinkoje triukšmų lygis dar labiau išauga, o laikiniame signale matyti fizikinės sistemos šuoliai tarp dviejų būsenų (8 (c) pav.).

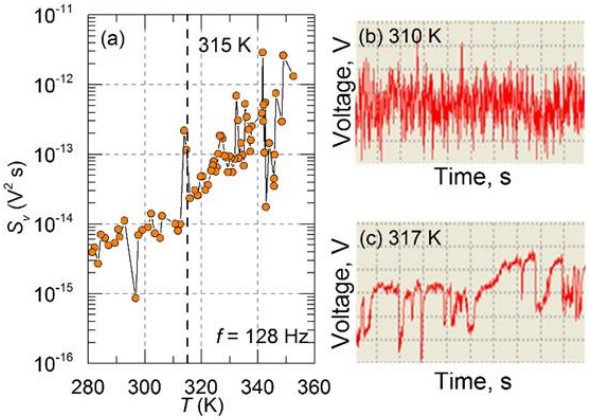

8 pav. $CuInP_2S_6$ kristalo įtampos fliuktuacijų spektrinio tankio priklausomybė nuo temperatūros (a), triukšminio signalo laikinis vaizdas 310 K (b) ir 317 K (c) temperatūroje.

9(a) pav. pateiktos įtampos fliuktuacijų spektrinio tankio dažninės priklausomybės fazinio virsmo temperatūros aplinkoje. Matyti, kad kambario temperatūroje $CuInP_2S_6$ matoma tik nuo dažnio nepriklausanti šiluminio triukšmo komponentė. Pašildžius iki 315 K temperatūros, kurioje vyksta fazinis virsmas, triukšmas įgyja $1/f^{\alpha}$ tipo pavidalą.

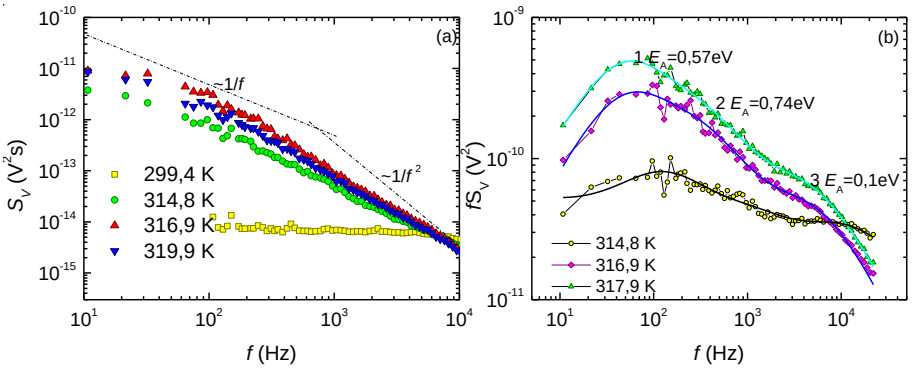

9 pav. $CuInP_2S_6$ kristalo įtampos fliuktuacijų spektrinis tankis (a) ir normuotas įtampos fliuktuacijų spektrinis tankis (b).

Fizikinė žemadažnio triukšmo atsiradimo prigimtis nėra aiški. Siekiant aiškumo įtampos fliuktuacijų spektrinis tankis buvo normuojamas dauginant iš atitinkamo dažnio (9 (b) pav.). Gautame spektre aiškiai matyti Lorenco tipo procesai. Kadangi tirtasis kristalas yra puslaidininkis, todėl tolesnei

triukšminei analizei pasienkamas relaksacinis $1/f$ triukšmo atsiradimo modelis, kuris paremtas generacinių-rekombinacinių procesų superpozicija:

$$S(f) = \frac{A}{f^{\alpha}} + \sum_{i=1}^{n} \frac{2\tau_i A_{gr_i}}{1 + (2\pi f \tau_i)^2} + S_{white} \qquad (4)$$

Fazinio virsmo aplinkoje įtampos fliuktuacijų spektriniame tankyje aiškiai matomi keli relaksaciniai procesai, kurie gali būti aprašomi (4) formule. Pasirinkta aproksimuoti trimis skirtingais procesais, kurių aktyvacijos energijos yra 0,57 eV, 0,7 eV ir 0,1 eV. Gautos aktyvacijos energijos susietos su dinaminiais procesais vykstančiais medžiagoje ir defektų įtaka.

Remiantis literatūros duomenimis, $CuInP_2S_6$ kambario temperatūroje išmatuota 55 μC cm^{-2} savaiminė poliarizacija ir 77 kC cm^{-1} koercinis laukas [6]. Disertacijoje pateiktos histerezės kilpos išmatuotos temperatūrų intervale 193-313 K. 10 pav. pateiktos histerezės, susijusios su triukšmų tyrimais.

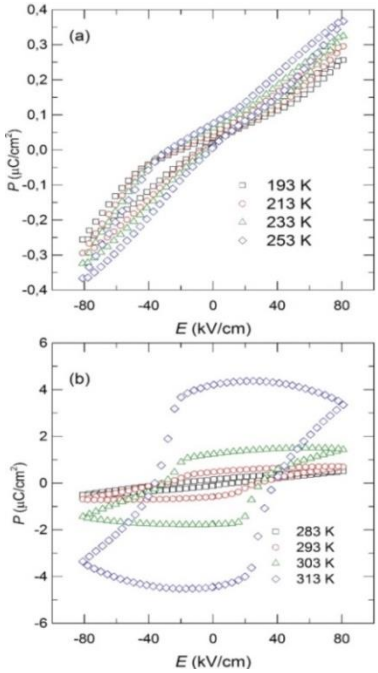

10 pav. $CuInP_2S_6$ kristalo histerezės matuotos skirtingose temperatūrose.

Iš pateiktų histerezių matyti stipri elektrinio laidumo ir defektų įtaka kristalo feroelektrinėms savybėms. Savaiminės poliarizacijos ir koercinio lauko vertės gerai sutampa su pateiktomis literatūroje.

IŠVADOS

1. Stebėtas neįprastas poliarizacijos persijungimas pasireiškiantis dvigubos histerezės kilpos forma vienašiuose tūriniuose feroelektrikuose $Sn_2P_2S_6$. Šis ypatumas susijęs su trijų duobių potencialo pavidalu, lemiančiu metastabilios būsenos atsiradimą žemiau antros rūšies fazinio virsmo temperatūros. Kvantinio anharmoninio osciliatoriaus modelis paaiškina feroelektrinės ir antiferoelektrinės fazių koegzistavimą Sn2P2S6 kristale.
2. Ištyrus $(Pb_ySn_{1-y})_2P_2S_6$ kristalų (y=0,1; 0,2 ir 0,3) dielektrines, piroelektrines ir feroelektrines savybes nustayta kad didinant švino priemaišų koncentraciją fazinio virsmo charakteristikos tampa sudėtingesnės su feroelektrinės ir paraelektrinės fazių koegzistavimu.
3. $Pb_2P_2S_6$ tipo kristaluose pasireiškia kvantinė paraelektrinė būsena, aprašoma Bareto modeliu plačiame temperatūrų intervale. Šis reiškinys fosforo chalkogenido kristaluose atsiranda didinant švino priemaišų koncentraciją (y>0.7). Įvedus nedidelį kiekį germanio priemaišų (2%) $(Pb_{0,98}Ge_{0,02})_2P_2S_6$ kristale atsiranda feroelektrinė fazė.
4. Triukšminė spektroskopija panaudota pirmą kartą ištirti $CuInP_2S_6$ kristalui fazinio virsmo artumoje temperatūrų intervale nuo 300K iki 340K ir dažnių ruože 10Hz-20kHz. $CuInP_2S_6$ triukšmo spektrų temperatūrinės ir dažninės priklausomybės tyrimas leidžia daryti išvadą, kad žemadažnį triukšmą lemia dinaminiai procesai susiję su faziniu virsmu, vario jonų judėjimas ir gardelės defektų svyravimai.

Literatūros šaltiniai

[1] Y. Vysochanskii et al., *Phase Transitions in Ferroelectric Phosphorous Chalcogenide Crystals*. Vilnius: Vilnius University Publishing House, 2008.

[2] C. Carpentier and R. Nitsche, "Ferroelectricity in $Sn_2P_2S_6$," *Mater. Res. Bull.*, vol. 9, no. 8, pp. 1097–1100, 1974.

[3] R. Yevych and Y. Vysochanskii, "Description of lattice anharmonicity observed in ferroelectrics with unusual three-well local potential," *Condens. Matter Phys.*, vol. 21, no. 3, p. 33001, 2018.

[4] R. Yevych et al., "Valence fluctuations in $Sn(Pb)_2P_2S_6$ ferroelectrics," *Low Temp. Phys.*, vol. 42, no. 12, pp. 1155–1162, 2016.

[5] A. Dziaugys et al., "*Phase Transitions in Layered Semiconductor - Ferroelectrics*," in Ferroelectrics - Characterization and Modeling, M. Lallart, Ed. InTech, 2011, pp. 153–180.

[6] X. Bourdon, V. Maisonneuve, V. . Cajipe, C. Payen, and J. . Fischer, "Copper sublattice ordering in layered $CuMP_2Se_6$ (M=In, Cr)," *J. Alloys Compd.*, vol. 283, pp. 122–127, 1999.

INFORMACIJA APIE AUTORĘ

Vardas Pavardė	Ilona Zamaraitė
El. paštas	ilona.zamaraite@ff.vu.lt

Išsilavinimas

2009-2013 m. Vilniaus universiteto Fizikos fakultetas (Bakalauro studijos);
2013-2015 m. Vilniaus universiteto Fizikos fakultetas (Magistrantūros studijos);
2015-2018 m. Vilniaus universiteto Fizikos fakultetas (Doktorantūros studijos).

Dalyvavimas mokslo projektuose

2015-2019 m. Horizon2020, Marie-Curie RISE veiklos projectas TUMOCS nr. 645660. Projekto dalyvė
2016-2017 m. Lietuvos-Ukrainos programa, projekto nr. TAP-LU-15-005. Projekto dalyvė

Mokslinės stažuotės

2017.01.08-2017.02.09 Stažuotė Aveiro universitete, Portugalijoje.
2018.03.23-2018.04.24 Stažuotė į Minsko mokslinį-praktinį medžiagotyros centrą, priklausantį Baltarusijos mokslų akademijai.

Vilniaus universiteto leidykla
Saulėtekio al. 9, LT-10222 Vilnius
El. p. info@leidykla.vu.lt,
www.leidykla.vu.lt
Tiražas 15 egz.